**Naval Surface Warfare Center**
**Carderock Division**
West Bethesda, MD 20817-5700

**NSWCCD-61-TR-2019/03** **May 2019**

Platform Integrity Department

Technical Report

# Temperature-Dependent Material Property Databases for Marine Steels – Part 1: DH36

by

Daniel H. Bechetti

Jennifer K. Semple

Wei Zhang

Charles R. Fisher

**Naval Surface Warfare Center**
**Carderock Division**
West Bethesda, MD 20817-5700

**NSWCCD-61-TR-2019/03** **May 2019**

Platform Integrity Department
Technical Report

# Temperature-Dependent Material Property Databases for Marine Steels – Part 1: DH36

by
Daniel H. Bechetti
Jennifer K. Semple
Wei Zhang
Charles R. Fisher

# REPORT DOCUMENTATION PAGE

*Form Approved*
*OMB No. 0704-0188*



**1. REPORT DATE** *(DD-MM-YYYY)*
29-05-2019

**2. REPORT TYPE**
Technical Report

**3. DATES COVERED** *(From - To)*
AUG 2016 – JAN 2017

**4. TITLE AND SUBTITLE**

Temperature-Dependent Material Property Databases for Marine Steels – Part 1: DH36

**5a. CONTRACT NUMBER**
N/A

**5b. GRANT NUMBER**
N/A

**5c. PROGRAM ELEMENT NUMBER**
N/A

**6. AUTHOR(S)**

Daniel H. Bechetti
Jennifer K. Semple
Wei Zhang
Charles R. Fisher

**5d. PROJECT NUMBER**
N/A

**5e. TASK NUMBER**
N/A

**5f. WORK UNIT NUMBER**
N/A

**7. PERFORMING ORGANIZATION NAME(S) AND ADDRESS(ES) AND ADDRESS(ES)**

Naval Surface Warfare Center,
Carderock Division, Code 611
9500 MacArthur Boulevard
West Bethesda, MD 20817-5700

Ohio State University, Department of Materials Science & Engineering
Welding Engineering Program
1248 Arthur Adams Dr
Columbus, OH 43221

**8. PERFORMING ORGANIZATION REPORT NUMBER**

NSWCCD-61-TR-2019/03

**9. SPONSORING / MONITORING AGENCY NAME(S) AND ADDRESS(ES)**

William Mullins
Program Manager, 332
Office of Naval Research
Arlington, VA 22217

Lightweight Innovations for Tomorrow (LIFT)
Detroit, MI 48216

**10. SPONSOR/MONITOR'S ACRONYM(S)**

**11. SPONSOR/MONITOR'S REPORT NUMBER(S)**
N/A

**12. DISTRIBUTION / AVAILABILITY STATEMENT**
DISTRIBUTION A. Approved for public release: distribution unlimited.

**13. SUPPLEMENTARY NOTES**

**14. ABSTRACT:**
The Lightweight Innovations for Tomorrow (LIFT) project entitled, *Robust Distortion Control Methods and Implementation for Construction of Lightweight Metallic Structures*, sought to address distortion issues with thin-plate steel fabrication of U.S. Navy ships. Integrated computational materials engineering (ICME)-based tools and techniques were identified as the best path forward for distortion mitigation through computational simulation of the welding process. ICME tools require temperature-dependent material properties to achieve accurate computational results for distortion and residual stress. Properties of note include specific heat, thermal conductivity, coefficient of thermal expansion, elastic modulus, yield strength, and flow stress of alloys, from room temperature up to near melting point. In addition, the temperatures associated with on-heating and on-cooling phase transformations and their variation with heating rate, cooling rate, and peak temperature are also important for the prediction of stress and distortion evolution.

The integrated project team (IPT) made generating pedigreed, temperature-dependent material property databases of Navy-relevant steels a key task within the LIFT project. The testing plan included some of the most common marine steels used in the construction of U.S. Naval vessels; namely, DH36, HSLA-65, HSLA-80, HSLA-100, HY-80, and HY-100. Material testing for each of the six steel grades was performed jointly by the Welding Engineering Program within the Department of Materials Science and Engineering at the Ohio State University (OSU) and the Welding, Processing, and Nondestructive Evaluation Branch at the Naval Surface Warfare Center, Carderock Division (NSWCCD). The temperature-dependent material property data was then sent to ESI for adaptation for use in their welding-based, finite-element analysis (FEA) software colloquially known as SYSWELD.

This report is part of a seven-part series detailing the pedigreed steel data. The first six reports will report and discuss the material properties for each of the individual steel grades, whereas the final report will compare and contrast the measured steel properties across all six steels, while also comparing them to the available literature data. This report will focus specifically on the data associated with DH36 steel.

**15. SUBJECT TERMS**
ICME, CWM, SYSWELD, Computational Simulation, Steel, Welding, Material Database, DH36

| **16. SECURITY CLASSIFICATION OF: UNCLASSIFIED** | | | **17. LIMITATION OF ABSTRACT** | **18. NUMBER OF PAGES** | **19a. RESPONSIBLE PERSON** |
|---|---|---|---|---|---|
| **a. REPORT** | **b. ABSTRACT** | **c. THIS PAGE** | | | Charles Fisher |
| UNCLASSIFIED | UNCLASSIFIED | UNCLASSIFIED | | 92 | **19b. TELEPHONE NUMBER** (301) 227-4969 |

## CONTENTS

*Page*

## FIGURES

*Page*

## TABLES

*Page*

## ADMINISTRATIVE INFORMATION

The work described in this report was performed by the Welding, Processing, and Nondestructive Evaluation Branch (Code 611) of the Platform Integrity Department at the Naval Surface Warfare Center, Carderock Division (NSWCCD) and by the Department of Materials Science and Engineering at the Ohio State University. The work was funded in FY16 by the Office of Naval Research (ONR) and the Office of the Secretary of Defense (OSD), in support of the Lightweight Innovations for Tomorrow (LIFT) Institute's program entitled, *Robust Distortion Control Methods and Implementation for Construction of Lightweight Metallic Structures*.

## ACKNOWLEDGEMENTS

The authors would like to thank the other members of the LIFT Joining-R1-3 integrated project team, including other engineers at the Naval Surface Warfare Center, Carderock Division (Matthew Sinfield, David Kihl, Maria Posada, and Johnnie Deloach), Huntington Ingalls Industries – Ingalls Shipbuilding (T.D. Huang, Harry Rucker, Randy Johnson, Yu-Ping Yang, Steve Scholler, Charlotte Merritt, Michael Harbison, Shannon Dolese, Anthony Copeland, Melvin Washington, Stacey Merritt, Win Delancey, Dianna Genton, Lee Kvidahl, and John Walks), the University of Michigan (Pingsha Dong, Jack Hu, Matt Collette, Haseung Chung, Mark Groden, Mark Para-Shostrand, and Trey Neveux), the Massachusetts Institute of Technology (Richard Roth, Michele Bustamante, Randy Kirchain, and Joel Clark), EWI (Randy Dull and Wael Alfakir), ESI (Yogendra [San] Gooroochan and Mark Doroudian), the American Bureau of Shipping (Alex Gonzalez and Kin-Ling Sham), Comau, LLC (Martin Kinsella) and LIFT (Melvin Hawke, Alan Taub, and Hadrian Rori), for their technical assistance in the completion of this work.

*This page intentionally left blank*

## EXECUTIVE SUMMARY

*The Lightweight Innovations for Tomorrow (LIFT) project entitled, Robust Distortion Control Methods and Implementation for Construction of Lightweight Metallic Structures, sought to address distortion issues with thin-plate steel fabrication of U.S. Navy ships. Integrated computational materials engineering (ICME)-based tools and techniques were identified as the best path forward for distortion mitigation through computational simulation of the welding process. ICME tools require temperature-dependent material properties to achieve accurate computational results for distortion and residual stress. Properties of note include specific heat, thermal conductivity, coefficient of thermal expansion, elastic modulus, yield strength, and flow stress of alloys, from room temperature up to near melting point. In addition, the temperatures associated with on-heating and on-cooling phase transformations and their variation with heating rate, cooling rate, and peak temperature are also important for the prediction of stress and distortion evolution.*

*The integrated project team (IPT) made generating pedigreed, temperature-dependent material property databases of Navy-relevant steels a key task within the LIFT project. The testing plan included some of the most common marine steels used in the construction of U.S. Naval vessels; namely, DH36, HSLA-65, HSLA-80, HSLA-100, HY-80, and HY-100. Material testing for each of the six steel grades was performed jointly by the Welding Engineering Program within the Department of Materials Science and Engineering at the Ohio State University (OSU) and the Welding, Processing, and Nondestructive Evaluation Branch at the Naval Surface Warfare Center, Carderock Division (NSWCCD). The temperature-dependent material property data was then sent to ESI for adaptation for use in their welding-based, finite-element analysis (FEA) software colloquially known as SYSWELD.*

*This report is part of a seven-part series detailing the pedigreed steel data. The first six reports will report and discuss the material properties for each of the individual steel grades, whereas the final report will compare and contrast the measured steel properties across all six steels, while also comparing them to the available literature data. This report will focus specifically on the data associated with DH36 steel.*

## BACKGROUND

The Lightweight Innovations for Tomorrow (LIFT) project entitled, *Robust Distortion Control Methods and Implementation for Construction of Lightweight Metallic Structures*, is a collaborative research project to address the complex fabrication problems that arise from the use of thin, high-strength steel panels for ship construction. The importance of lightweighting in the commercial and military shipbuilding sectors has gained attention in recent decades as a way to increase the performance capabilities of products while also reducing total ownership costs. Over the past decade, the production ratio of thin plate (10 mm [3/8-in.] or less) to thicker plate structures for steel construction at Huntington Ingalls Industries – Ingalls Shipbuilding has risen to over 80% in the Coast Guard's National Security Cutter (NSC) program. Modern naval vessel designs also make greater use of complex panels with inserts and cutouts, further increasing the fabrication complexity to achieve weight savings while meeting structural requirements.

European shipbuilding research suggests that 30% of hull fabrication costs can be attributed to re-work and fit-up issues due to distortion [1]. Integrated computational materials engineering (ICME)-based prediction tools can be used to quantify distortions associated with the fabrication process of complex

stiffened panels or other lightweight structures. These tools, once validated on selected product forms, could be used to establish recommended fitting, fixturing, welding, and assembly sequencing for optimized distortion control in thin-plate steel construction.

These ICME tools require detailed, reliable databases of temperature-dependent material properties in order to increase the accuracy of calculated distortion and residual stresses in welded metallic structures. Of highest importance to the fidelity of such models are the thermo-physical and thermo-mechanical properties of the material(s) being joined. The properties of note include specific heat, thermal conductivity, coefficient of thermal expansion, elastic modulus, yield strength, and flow stress, from room temperature up to nearly the alloy's melting point. The temperatures associated with on-heating and on-cooling phase transformations and their variation with heating rate, cooling rate, and peak temperature are also important for the prediction of stress and distortion evolution.

While some of these data exist for the most common Navy steels, these are generally not suitable for use in high-fidelity welding-focused computational models for several reasons. First, the methods of data generation are inconsistent because the testing was completed over many decades by separate researchers and programs. Also, significant gaps exist in the data, especially at temperatures above approximately 400 °C (~750 °F). Additionally, some available data are restricted against public distribution. Finally, the data are, in general, subject to reliability issues because of changes in material fabrication and testing practices that have occurred in the decades since the data were generated. To combat this lack of comprehensive and consistent data, the integrated project team (IPT) made generating pedigreed, temperature-dependent material property databases of Navy-relevant steels a key task within the LIFT project. A major portion of the tasking involved analysis of heat-affected zone (HAZ) microstructures, as this region of rapidly changing microstructure results in significant changes in resultant mechanical properties. These varied HAZ region microstructures of Navy-relevant also do not have well-established mechanical property data, especially as a function of temperature and heating or cooling rate.

The testing plan included some of the most common marine steels used in the construction of U.S. Naval vessels; namely DH36, HSLA-65, HSLA-80, HSLA-100, HY-80, and HY-100. HSLA is short for "high-strength low-alloy," whereas HY stands for "high yield." The number designation behind HSLA and HY is the minimum yield strength of the plate material in units of ksi. Current (as of this writing) specifications for these alloys can be found in references [2] [3] [4]. Material testing for each of the six steel grades was performed jointly by the Welding Engineering Program within the Department of Materials Science and Engineering at the Ohio State University (OSU) and the Welding, Processing, and Nondestructive Evaluation Branch at the Naval Surface Warfare Center, Carderock Division (NSWCCD). The temperature-dependent material property data was then sent to ESI for adaptation for use in their welding-based, finite-element analysis (FEA) software colloquially known as *SYSWELD*.

This report is part of a seven-part series based on the pedigreed steel data. The first six reports will focus on establishing the material properties for each of the individual steel grades, whereas the final report will compare and contrast the measured steel properties across all six steels, while also comparing them to the available literature data. Follow-on reports detailing use of these temperature-dependent material databases within the LIFT-funded program are also expected.

## APPROACH

### Material Testing Program

The material property assessment program was developed through inputs from welding engineers at NSWCCD, researchers at OSU, and modeling experts at ESI. The program focused on generating the

types of data required to develop Navy-relevant material databases for use by ESI's commercial software, *SYSWELD*. The raw data could also be adapted for use by other FEA tools, such as MSC's *Simufact Welding* or the welding module for *Abaqus*. Specific data included thermo-physical and mechanical properties of the alloys of interest, from room temperature up to near-melting. Density, heat capacity, thermal conductivity, and coefficient of thermal expansion (CTE) were identified as the most important thermo-physical properties. Mechanical properties of interest included the elastic modulus, yield strength, and flow stress.

Material from a single DH36 steel plate procured to MIL-S-22698C [2] was analyzed for this project. The plate was acquired by Huntington Ingalls Industries – Ingalls Shipbuilding (HII – Ingalls) and was nominally 4.76 mm (3/16-in.) thick. Military grade DH36 is roughly equivalent to commercial products specified in ASTM A541 (Class 1C) [5], ASTM A131 (Grade DH36) [6], and American Bureau of Shipping (ABS) grade DH36 [7]. The room temperature yield strength, ultimate tensile strength, and elongation requirements for the alloy are 352 MPa (51 ksi), 490 to 621 MPa (71 to 90 ksi), and 19% in 200 mm (8-in.) or 22% in 50 mm (2-in.), respectively [2]. The plate conformance certification sheet for the material investigated in this study is given in **Appendix A**. A portion of this plate was cut into 610 mm by 305 mm (24-in. by 12-in.) pieces and shipped to both NSWCCD and OSU for determination of temperature-dependent material properties.

### *Chemical Composition*

The chemical composition of the base material was measured at the Edison Welding Institute (EWI) using glow discharge atomic emission spectrometry in accordance with ASTM E415 [8].

### *Solidus and Liquidus Analysis*

The solidus and liquidus temperatures were evaluated using a single-sensor differential thermal analysis (SS-DTA) apparatus, where a 6 g (0.2 oz) button of material underwent induction levitation melting and was dropped into a copper crucible while temperature data were collected with a Type C thermocouple. This technique measures the temperature of a liquid metal sample as it rapidly cools via conduction through a water-cooled copper crucible. Phase transformations are reflected in there temperature data by non-linearity associated with the latent heat of fusion.

### *Heat Affected Zone Phase Transformation Analysis*

Phase transformations of DH36 as a function of austenitization temperature and cooling rate were assessed via dilatometry. Continuous cooling transformation (CCT) diagrams were developed for four regions of the heat affected zone (HAZ) that are subject to microstructural transformation during welding: the intercritical region (ICHAZ); the low-temperature, fine-grained region (FGHAZ1); the high-temperature, fine-grained region (FGHAZ2); and the coarse-grained region (CGHAZ).

Heating and cooling rates for these regions were defined by combining typical heat inputs used in the fabrication of DH36 weldments, from 0.4 to 2.6 kJ/mm (10 to 65 kJ/in) as suggested by Ingalls engineers, with numerical simulation of the heat flow using the *SmartWeld* program from Sandia National Laboratories [9]. From these calculations, it was determined that peak temperatures ($T_{peak}$) between 875 and 1350 °C (1607 and 2462 °F), in combination with cooling rates between 1 and 200 °C/s (1.8 and 360 °F/s), would provide information covering a sufficiently broad range of phase transformation behavior relevant to both slowly-cooled welds (e.g., high heat input welds on thin plate) and rapidly-cooled welds (e.g., low heat input welds on thick plate). These CCT diagrams informed the temperature-dependent mechanical property testing program as well, specifically for heating and cooling rates, peak temperatures, and various testing temperatures.

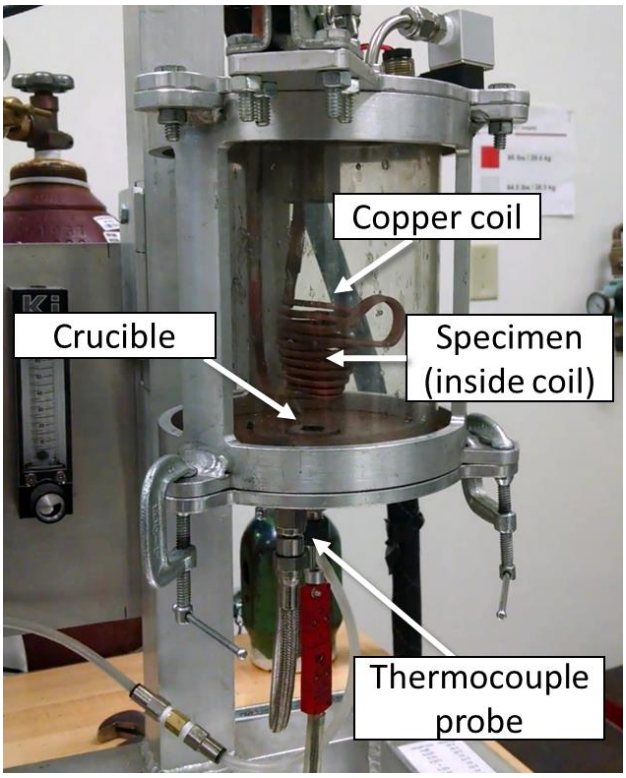


**Figure 1.** Induction levitation setup used in the measurement of DH36 liquidus and solidus temperatures.

In addition to the on-cooling CCT diagram development, this portion of the testing program also involved a detailed assessment of the on-heating austenite transformation as a function of heating rate. Just as on-cooling transformation temperatures vary with cooling rate, so does on-heating austenitization temperature ($A_{c1}$ and $A_{c3}$). Heating rates between 100 and 2000 °C/s (180 and 3600 °F/s) were used to study these variations. **Table 1** shows the full test matrix utilized for HAZ CCT diagram development.

**Table 1.** Test matrix for HAZ CCT diagram development

| Test Type | Region | Peak Temperature, °C (°F) | Heating Rate, °C/s (°F/s) | Soak Time, s | Cooling Rate, °C/s (°F/s) |
|---|---|---|---|---|---|
| $A_{c1}/A_{c3}$ Determination | N/A | 1200 (2192) | 100 (180)<br>200 (360)<br>500 (900)<br>1000 (1800)<br>2000 (3600) | N/A | N/A |
| CCT Diagram Development | ICHAZ | 875 (1607) | 200 (360) | 2 | 1 (1.8)<br>5 (9)<br>10 (18)<br>25 (45)<br>100 (180)<br>200 (360) |
| | FGHAZ1 | 1000 (1832) | | | |
| | FGHAZ2 | 1150 (2102) | | | |
| | CGHAZ | 1350 (2462) | | | |

Execution of this test matrix was performed in tandem at NSWCCD and OSU, with both facilities employing a Gleeble thermo-mechanical simulation apparatus to apply the prescribed heating and cooling rates. The Gleeble operates on the principles of resistive heating, conductive cooling through water-

cooled fixturing, and rapid (50 kHz) control system feedback to apply precise thermal cycles, even at rapid heating and cooling rates that cannot be easily achieved by other apparatus. At NSWCCD, a Gleeble 3500 was used in combination with the apparatus's standard 'Pocket Jaw' setup, full contact copper grips, and 70 mm (2.76-in.) long specimens with 3 mm (0.118-in.) diameters. A linear variable differential transformer (LVDT)-type contact extensometer was used to measure diametric dilation of the specimens during heating and cooling. A Gleeble 3800 system was used at OSU, in combination with the apparatus's 'Low Force Jaw' setup, full contact copper grips, and 70 mm (2.76-in.) long specimens with 5 mm (0.20-in.) by 11 mm (0.43-in.) rectangular cross-sections. A LVDT-type extensometer similar to that used at NSWCCD was used for dilation measurement. All dilatometry specimens were extracted perpendicular to the rolling direction of the plate, and all dilatometry tests were performed in an argon atmosphere. The typical experimental setup for the dilatometry testing is shown in **Figure 1.**

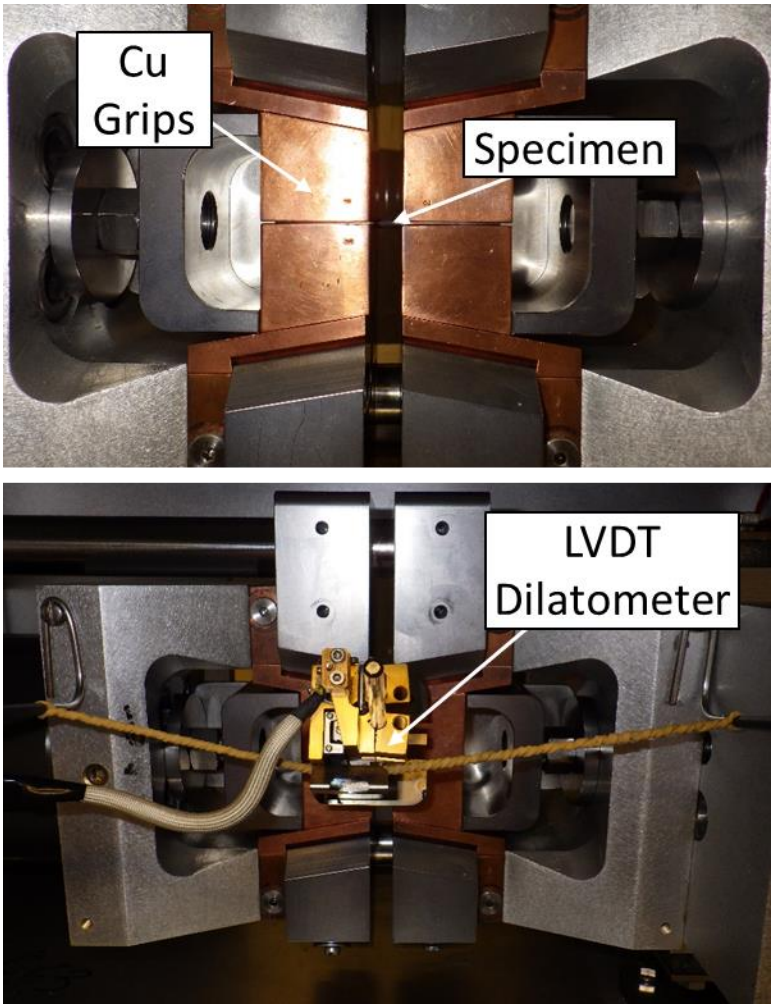


**Figure 2.** Photographs of the Gleeble-based dilatometry experimental set-up

***Thermo-Physical Property Analysis***

Specimens were sent to the Thermophysical Properties Research Laboratory, Inc. (TPRL) in West Lafayette, IN for analysis of thermal diffusivity ($\alpha$) and specific heat ($C_p$). Thermal diffusivity was measured using the laser flash method according to ASTM E1461 [10]. Specific heat was measured using differential scanning calorimetry (DSC) methods according to ASTM E1269 [11]. Coefficient of thermal expansion (CTE) was measured from the on-heating Gleeble dilatometry data in two regimes: 50 to 650

°C (122 to 1202 °F) for the base material microstructure, and 950 to 1200 °C (1742 to 2192 °F) for austenite. No attempt was made to determine CTE during the on-heating transformation. CTE calculations were either performed by linear fitting or by discrete analysis using the dilation data endpoints from each temperature range in conjunction with **Equation 1**. The material was assumed to be isotropic.

$$\alpha_T = \left(\frac{\Delta d}{d_0}\right)\left(\frac{1}{\Delta T}\right) \quad \textbf{(1)}$$

where $\alpha_T \equiv$ Linear coefficient of thermal expansion [°C$^{-1}$]
$\Delta d \equiv$ Change in specimen diameter over the chosen temperature range [cm]
$d_0 \equiv$ Initial specimen diameter [cm]
$\Delta T \equiv$ Temperature range [°C]

The temperature-dependent density ($\rho$) was calculated using a theoretical cubic volume element under the assumption of isotropic thermal expansion:

$$\rho(T) = \frac{\rho_0 V_0}{V(T)} \quad \textbf{(2)}$$

where $\rho(T) \equiv$ Density at temperature $T$ [g/cm$^{-3}$]
$\rho_0 \equiv$ Room temperature density provided by TPRL [g/cm$^3$]
$V_0 \equiv$ Room temperature volume of the theoretical cubic element [cm$^3$]
$V(T) \equiv$ Volume of the theoretical cubic element at temperature $T$ [cm$^3$]

$V_0$ was calculated assuming a side length equal to the room temperature width of OSU's dilatometry specimens. This value was chosen because, as shown in **Figure 2**, it corresponds to the starting gauge length for the dilatometer used to measure thermal expansion. A theoretical cubic volume element was chosen instead of the actual specimen dimensions to subvert potential complications with measuring dimensions that were not directly measured by the dilatometer (e.g. the effect of thermal gradients on measurement of the specimen's longitudinal expansion). $V_T$ was simply calculated by:

$$V(T) = [w(T)]^3 \quad \textbf{(3)}$$

where $w(T) \equiv$ Dilatometer-measured specimen width at temperature $T$ [cm]

This method allowed calculation of the density through the austenite transformation. Finally, thermal conductivity ($\lambda$) as a function of temperature was then calculated by using **Equation 4**:

$$\lambda = \rho \cdot c_p \cdot \alpha \quad \textbf{(4)}$$

where $\lambda \equiv$ Thermal conductivity [W/cm-°C]
$c_p \equiv$ Specific heat capacity [J/g-°C]
$\rho_0 \equiv$ Room temperature density [g/cm$^3$]
$\alpha \equiv$ Thermal diffusivity [cm$^2$/s]

### *Thermo-Mechanical Property Analysis*

Tensile specimens were machined from the DH36 plates according to the dimensions shown in **Figure 3a**. All specimens were extracted with their length perpendicular to the rolling direction of the

plate. Elastic modulus, yield strength, and flow stress were identified as the required mechanical properties from room temperature up to near-melting. On-heating tension testing of the DH36 base material at temperatures between 22 and 1100 °C (72 and 2012 °F) was subcontracted to IMR Test Labs in Portland, OR. Room temperature testing was performed in accordance with ASTM A370 [12], and elevated temperature testing was performed in accordance with ASTM E21 [13]. Specimens were of rectangular cross-sections with gauge widths of either 6 or 3 mm (0.50 or 0.25 in.). Testing was performed in strain control mode at target rates of 0.005 $min^{-1}$ prior to yield and 0.05 $min^{-1}$ after yield.

On-cooling mechanical properties were measured using the Gleeble 3500 at NSWCCD. Prior to mechanical testing, the specimens were thermally cycled to generate different initial microstructures based on the results of the CCT diagram development described above. For DH36, microstructural analysis indicated that substantially different microstructures formed when the material was cooled at 1, 10, and 100 °C/s (1.8, 18, and 180 °F/s). Because of programmatic time constraints, only a peak temperature of 1350 °C (2462 °F) was applied to the tensile specimens. All specimens were heated in an argon atmosphere, and forced air was used to meet cooling rates of 10 °C/s (18 °F/s) and above. All specimens were cooled to room temperature, and thereafter a contact longitudinal extensometer was affixed. The specimens were then reheated to the test temperature at a rate of 10 °C/s (18 °F/s) and soaked for 10 sec. before being pulled to failure in crosshead control mode at strain rates targeting those prescribed in ASTM E21 [13]. The crosshead displacement rates used were 0.30 mm/min (0.012 in/min) through yield and 0.40 mm/min (0.016 in/min) after yield. It is acknowledged that this is not the most representative method of testing for welding-related applications because the stresses that develop during welding do so rapidly and while the material is cooling and undergoing phase transformations. However, given the programmatic intent of establishing the mechanical behavior of specific microstructures and the need to avoid exposing the strain measurement device to exceedingly high temperatures, the method of cooling to room temperature and tension testing after reheating was determined to be an acceptable compromise. In cases where the induced microstructure was stronger than the base material, a second reduced gauge section was machined in the specimen prior to testing to ensure specimen fracture in the region of interest. This revised specimen geometry is shown in **Figure 3b**.

Thermal cycling and subsequent tensile testing were performed using the apparatus's 'Pocket Jaw' setup with minimal contact stainless steel grips used to fixture the specimen. These grips were selected to minimize the longitudinal thermal gradient in the gauge length of the specimens during testing. Graphite foil was inserted between the specimen and the grips to further minimize the thermal gradient. Strain in the specimens was measured using a contact longitudinal extensometer, and the initial gauge length for the tests varied between 8 and 10 mm (0.31 and 0.39 in.). Elevated temperature tension tests were performed in an argon atmosphere. Preliminary testing indicated that for this setup, the temperature variation across the initial gauge length was 10 to 30 °C (18 to 54 °F). The typical experimental setup for the dilatometry testing is shown in **Figure 4**.

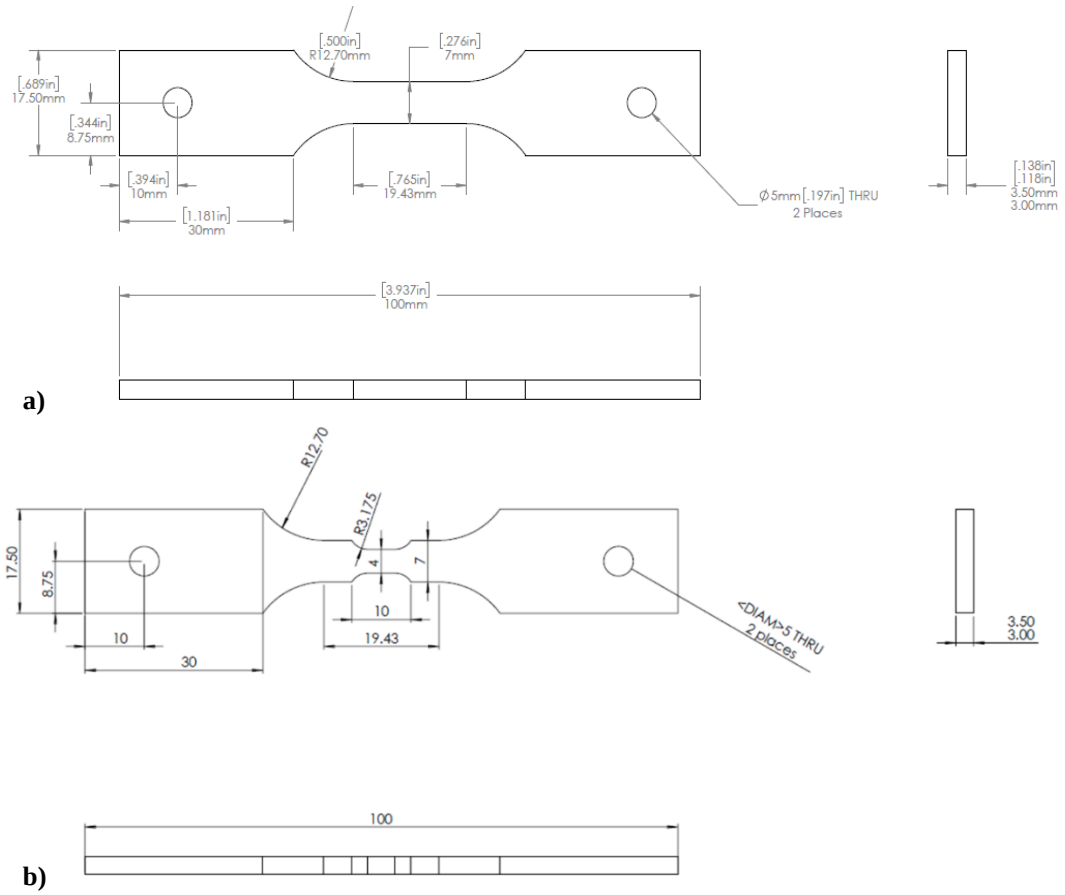


**Figure 3.** Specimen dimensions for Gleeble-based mechanical testing of DH36 steel: **a)** single-reduced gauge section, **b)** double-reduced gauge section (dimensions in mm).

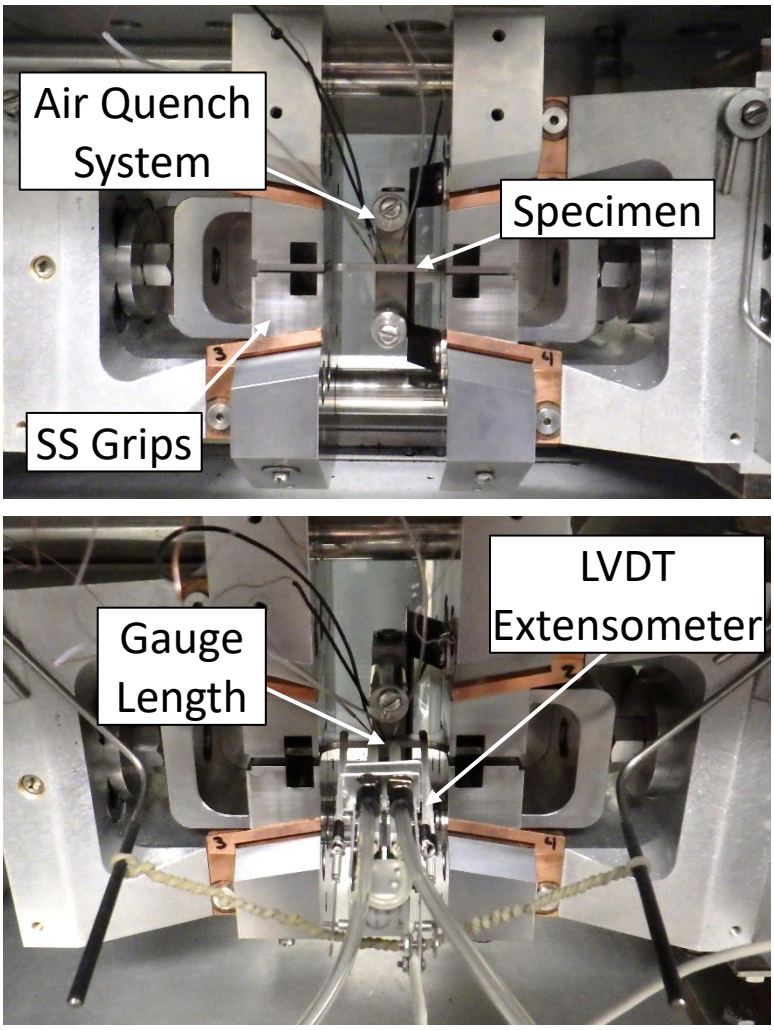


**Figure 4.** Photographs of the Gleeble-based mechanical testing experimental set-up.

### *Fabrication of Welded Specimens*

Additionally, two sets of plates were welded together at Ingalls and sent to OSU to investigate the plate, weld, and heat-affected zone (HAZ) microstructures. The first set of plates were welded using submerged arc welding (SAW) in a two-sided butt joint configuration, as shown in **Figure 5a**. Welding parameters used are given in **Table 2**. The second set of plates were welded using flux cored arc welding (FCAW) in a two-sided tee-joint configuration, as shown in **Figure 5b**. Welding parameters are given in **Table 2**. These weldments enabled correlation of the microstructures generated through thermal simulations for the CCT curves with those produced from arc welding. Each weldment is representative of two primary types of joints used at Ingalls for structural welds: seaming butt joints and fillet joint stiffener welds. These joint types were also the focus of larger fabrication efforts described in other tasks within the greater LIFT project as described in [14].

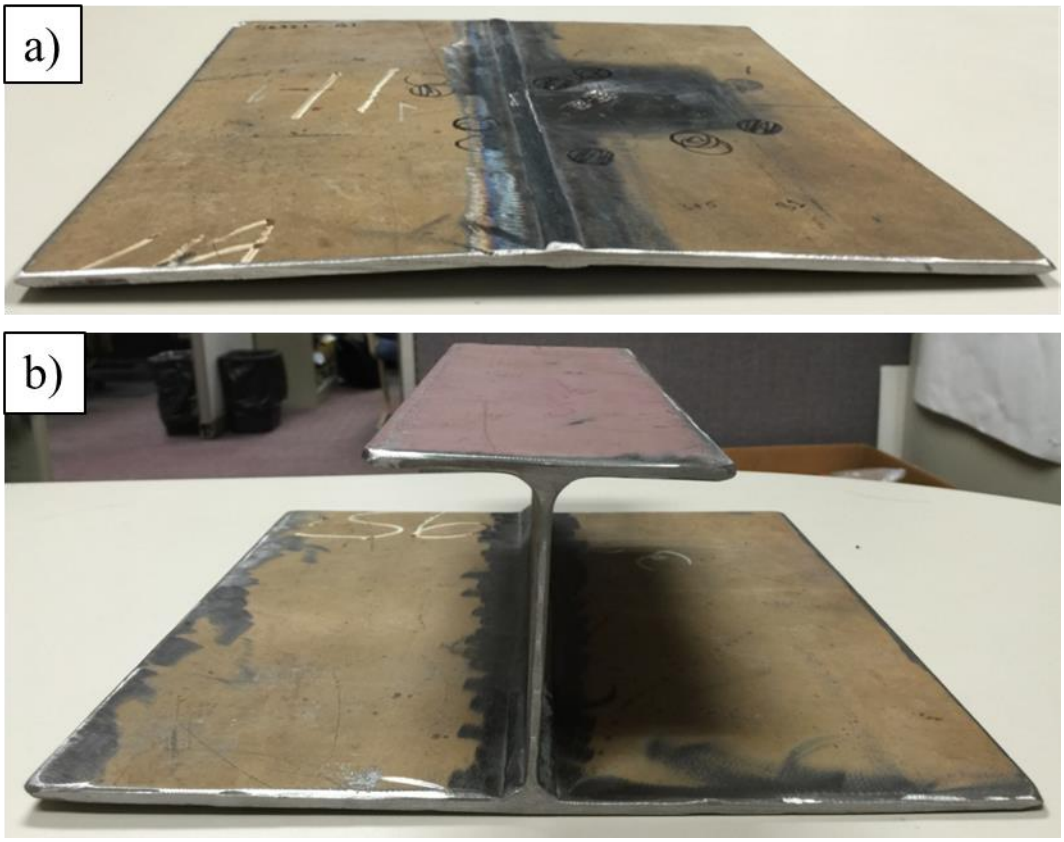


**Figure 5.** DH36 **a)** butt and **b)** tee joint weldments investigated for plate, weld, and HAZ microstructures.

**Table 2.** Nominal welding parameters used to fabricate DH36 butt and tee joints

| | **Butt Joint** | **Tee Joint** |
|---|---|---|
| **Welding Process** | Submerged arc (SAW) | Flux cored arc (FCAW) |
| **Current (A)** | 375 | 355 |
| **Voltage (V)** | 30 | 28 |
| **Travel Speed (mm/s [in/min])** | 12.7 (30) | 10.2 (24) |
| **Heat Input (kJ/mm [kJ/in])** | 0.89 (22.5) | 0.98 (24.8) |
| **Consumable Designation(s)** | AWS A5.17 F7A6-EM14K | AWS A5.20 E71T-1 |
| **Filler Wire Diameter (mm [in])** | 3.2 (1/8) | 1.6 (1/16) |
| **Interpass Temperature, Max. (°C [°F])** | 93 (200) | 107 (225) |

***Microstructural Analysis***

To quantify and characterize the microstructures observed in DH36, both in the welded and non-welded state, a cross-section of each of the weldments shown in **Figure 5** was analyzed. Each specimen was metallographically prepared to a final polish of 0.05 μm using standard techniques and etched with 2% Nital solution for light optical microscopy (LOM) and scanning electron microscopy (SEM) analysis.

Vickers microhardness values at 200 g (7.05 oz) load were taken from the fusion zone through the HAZ to the base material for both weldments.

Additionally, thermally-cycled specimens from the HAZ CCT diagram development were metallographically prepared to a final polish of 0.05 μm using standard techniques and etched with 4% Picral solution followed by 2% Nital solution. Identification and phase fraction measurement of the microstructural constituents in each specimen were evaluated using image analysis through LOM and SEM. Vickers microhardness testing was also used to determine the hardness of the constituent(s) in each CCT specimen. This analysis facilitated proper CCT analysis, provided phase fraction input for the DH36 material property database, and helped determine which thermal cycles were the most appropriate for application in the mechanical testing portion of the program described above.

## RESULTS AND DISCUSSION

### Chemical Composition

**Table 3** shows the averaged results of three base material chemistry measurements for the DH36 plate, plus manufacturer's plate certification values (shown in **Appendix A**) and the MIL-S-22698C specifications for DH36 steel [2]. As expected, the measured chemical composition values generally agreed with the manufacturer's plate certification and were well within military specifications. The carbon equivalency number (CEN) was calculated according to [15].

**Table 3.** Chemical composition of DH36 plate material (wt%)

| Type | C | Mn | P | S | Si | Cu | Ni | Cr | Mo |
|---|---|---|---|---|---|---|---|---|---|
| **Measured Avg.** | 0.057 | 1.39 | 0.013 | 0.007 | 0.25 | 0.025 | 0.012 | 0.042 | 0.005 |
| **Plate Certificate** | 0.07 | 1.31 | 0.011 | 0.004 | 0.241 | 0.028 | 0.02 | 0.04 | 0.006 |
| **MIL-S-22698 DH36** | < 0.18 | 0.90-1.60 | < 0.04 | < 0.04 | 0.10-0.50 | < 0.35 | < 0.40 | <0.25 | < 0.08 |

| Type | V | Ti | Al | B | Nb | N | Sn | Fe | **CEN** [15] |
|---|---|---|---|---|---|---|---|---|---|
| **Measured Avg.** | 0.043 | 0.017 | 0.034 | 0.0008 | 0.050 | --- | --- | Bal. | 0.200 |
| **Plate Certificate** | 0.044 | 0.014 | 0.033 | 0.0002 | 0.028 | 0.009 | 0.007 | Bal. | 0.210 |
| **MIL-S-22698 DH36** | < 0.10 | --- | --- | --- | <0.05 | --- | --- | Bal. | --- |

### Solidus and Liquidus Analysis

As shown by the SS-DTA data in **Figure 6**, the solidus and liquidus temperatures for DH36 were experimentally measured to be 1453 and 1483 °C (2647 and 2701 °F), respectively. To assess the ability of current CALPHAD (CALculation of PHAse Diagrams) methods to predict these temperatures and supplant some of the need for physical testing, thermodynamic equilibrium simulations using the Thermo-Calc software package [16] in combination with the TCFE9 database were performed on the measured plate composition given in **Table 3**. All reported elements were included in the simulations, and only the liquid, ferrite, austenite, cementite, and MC-type carbide phases were allowed to form. The simulations predicted slightly higher solidus and liquidus temperatures than the experimental measurements, at 1471 and 1522 °C (2680 and 2772 °F), respectively. The discrepancy is attributed to the rapid, non-equilibrium solidification induced by the SS-DTA, while the Thermo-Calc simulation reflects equilibrium values. Predictions from non-equilibrium solidification simulations using the Scheil Gulliver

model within Thermo-Calc predicted a solidus temperature closer to the experimental values (1430 to 1460 °C [2606 to 2660 °F], depending on the fraction of solid at which solidification was considered complete). The closer correspondence between the Scheil prediction and experimental measurement occurs because the Scheil simulations take into account the physical phenomenon of solute segregation, which suppresses the termination of solidification. However, it does not account for undercooling, so the liquidus temperature predicted by the Scheil simulation was still significantly higher than measured experimentally.

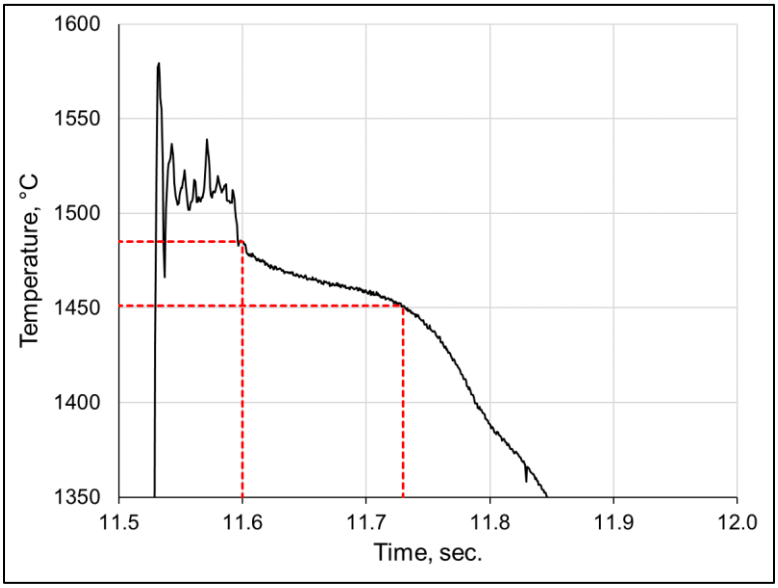


**Figure 6.** SS-DTA data for the solidus and liquidus measurement of DH36 steel

## Base Metal Microstructure

The microstructure of the DH36 base metal is shown in the light optical and SEM micrographs of **Figures 7a** and **b**, respectively. The white-etched structure is equiaxed ferrite (84%), and the dark-etched constituent is pearlite (16%). The amount of each constituent was quantified by standard image threshold techniques applied to five fields in *ImageJ* software [17], as shown in **Figure 7c**. The average Vickers microhardness of the base metal was 187 $HV_{200}$.

Observing the DH36 base metal in both the longitudinal and transverse planes revealed slight elongation of the grains along the rolling direction. The grain size was measured using the "intercept method" detailed in ASTM E1382 [18]. Using this technique, a circle is drawn at random locations within a micrograph (e.g., the purple circle shown in **Figure 7a**), and the number of times a grain boundary intercepts that circle is used to calculate the average grain size. Using a circle instead of a line ensured that rolling texture was accounted for. Measurements were taken twice on a sample longitudinal to the rolling direction and three times on a sample transverse to the rolling direction. The average ASTM grain size was calculated to be G = 12.

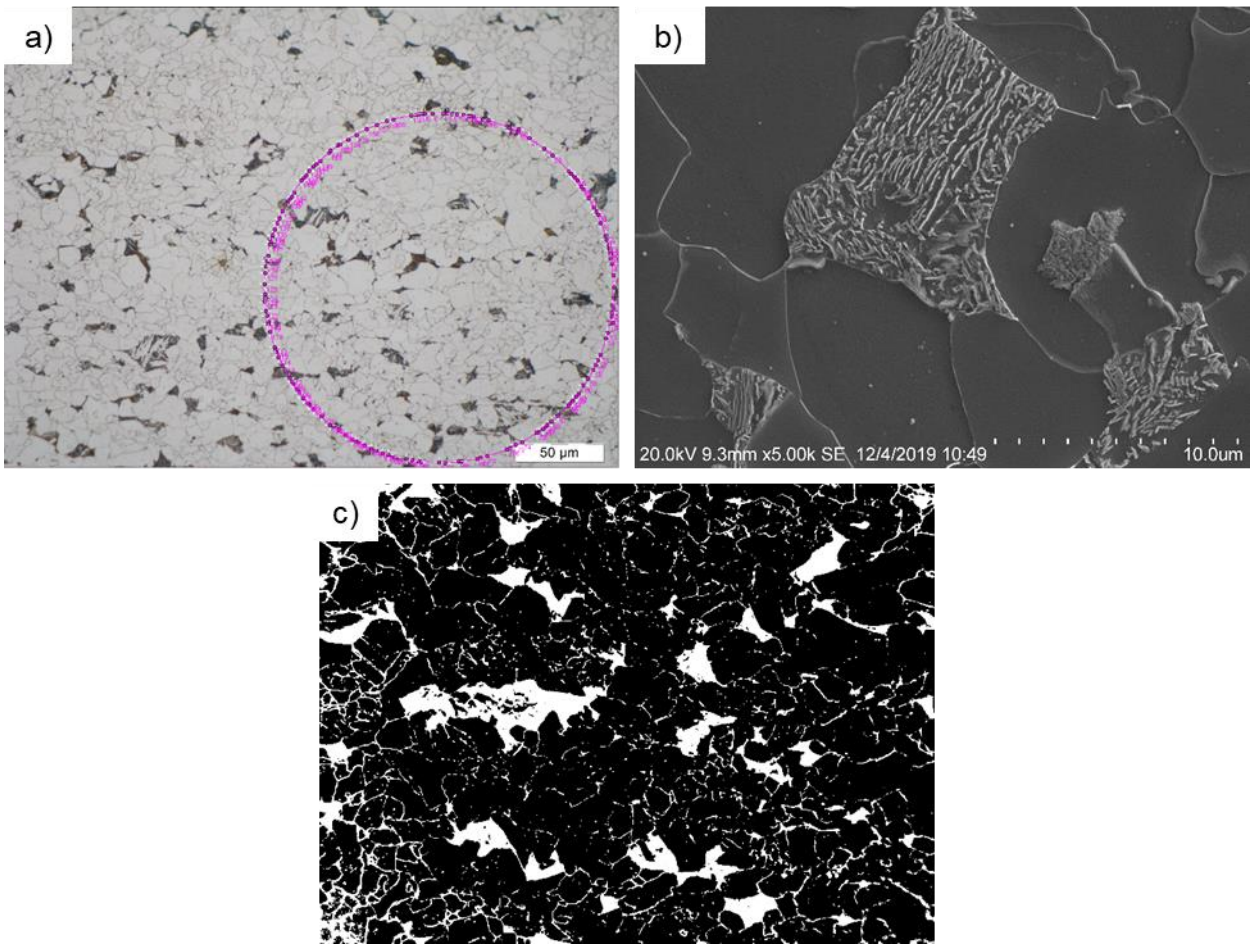


**Figure 7.** Representative micrographs of DH36 steel plate, showing **a)** base metal microstructure and **b)** an *ImageJ* representation of the microstructure used to calculate phase fraction. The purple circle in **a)** was used to calculate average grain size.

## Heat Affected Zone Phase Transformation Analysis

### *Dilation Curve Analysis Method*

**Figure 8** shows a representative on-heating portion of a Gleeble-produced dilatometry curve generated by NSWCCD. The black curve (left axis) represents the change in sample diameter with temperature, and non-linearity in the curve is indicative of a phase transformation's occurrence. Non-linearity is shown in the derivative curve, as shown by the red curve (right axis). Linear extrapolations of the black curve are shown by the blue lines. In this case, the transformation of interest is that of the DH36 base metal microstructure to austenite.

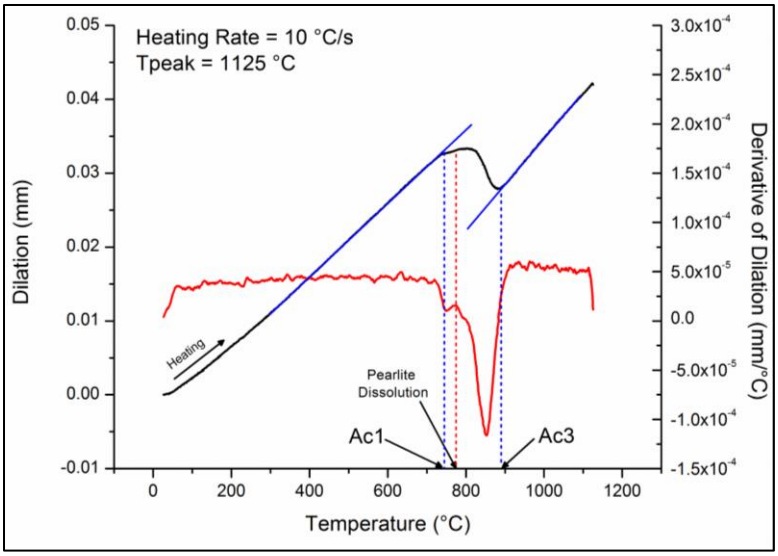


**Figure 8.** Representative on-heating dilatometry curve for DH36 steel, showing the linear extrapolation and derivative curve methods for evaluating the ferrite + pearlite to austenite reaction. Black curve, left axis: dilation data. Red curve, right axis: derivative of dilation data. Blue lines: extrapolation lines for determining transformation start ($A_{c1}$) and finish ($A_{c3}$) temperatures.

Two methods for extracting start and finish temperatures for phase transformations from Gleeble dilatometry data are commonly used. The first method involves superimposing a straight line of matching slope along the low temperature portion of the dilation curve and extrapolating it past the transformation. The point at which the experimental data begins to deviate from the straight line is then taken as the transformation start temperature. The same technique is then used to find the transformation finish temperature, with the straight line being extrapolated from the high-temperature portion of the curve after the transformation. The second method involves calculating and plotting the derivative of the dilation curve. Then the points at which the derivative begins to deviate from a constant value are taken as the transformation start and finish temperatures. Both methods for determining phase transformation temperatures are inherently somewhat subjective, and both also have advantages and disadvantages. The linear extrapolation method is faster and easier to interpret but is difficult to use when multiple transformations occur. The derivative method is more quantitative and can more easily distinguish multiple transformations but can be difficult to interpret when the dilation data is noisy. For this work, the linear extrapolation method was chosen as the primary method of data analysis, and the derivative method was used as a complementary technique for distinguishing concurrent phase transformations. Both methods are shown in **Figure 8**, where the derivative curve is displayed in red and the linear extrapolations are displayed in blue.

***Austenite Transformation Temperature Measurement***

On-cooling solid-state, phase transformation temperatures and products in steels can vary substantially with peak temperature due to differences in austenite grain size at different peak temperatures [19] [20] [21] [22]. Thus, it is expected that each of the investigated HAZ regions would produce slightly different CCT diagrams. The residual stress (and subsequent distortion) that develops during weld cooling is greatly influenced by: 1) the microstructure that forms on cooling and 2) the temperature difference between the end of the on-cooling transformations and the final temperature of the component. It was therefore important to capture as much HAZ phase transformation behavior as possible in order to provide the most complete and accurate material database for welding simulations.

**Figure 9** presents the variation in austenite transformation behavior as a function of heating rate for DH36 base material. As shown, the austenite transformation start ($A_{c1}$) temperature varies significantly over the range of experimental heating rates. This is a consequence of thermal diffusion during heating outpacing the mass diffusion required for the transformation to take place. The austenite transformation finish ($A_{c3}$) temperature remains relatively stable across the experimental heat rate range. The reason for the difference in heating rate response of the $A_{c1}$ and $A_{c3}$ temperatures in this material is not readily determined without further investigation. Researchers who have investigated similar behavior in other ferrous materials have associated heating rate dependencies of the austenite transformation with those of the controlling diffusion mechanism (i.e., volume carbon diffusion or grain boundary substitutional element diffusion), the ferrite recrystallization process, and/or austenite nucleation and growth rates [23] [24] [25]. These data are important for the refinement of welding simulation results because different regions of a weldment and its HAZ are subject to significantly different heating rates during the welding process. Thus, the on-heating transformation behavior must be incorporated in order to accurately predict which areas around the weld will transform to austenite, and will therefore be subject to re-transformation (and associated changes in mechanical properties and residual stresses) during cooling. The raw data points for **Figure 9** can be found in **Table 8** within **Appendix B.**

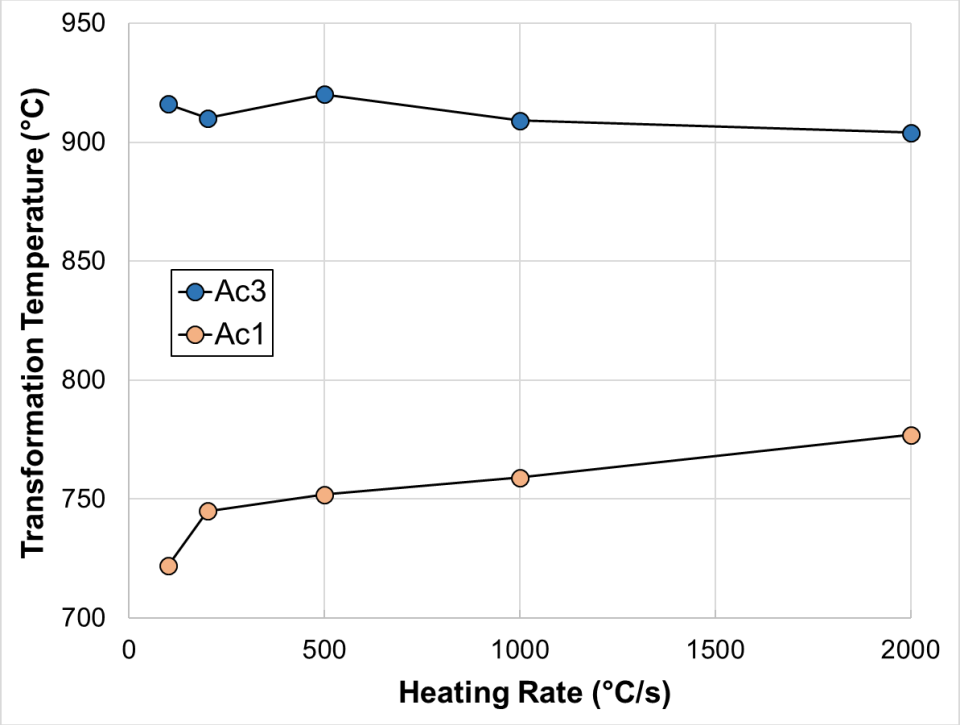


**Figure 9.** Variation in austenite transformation start and finish temperatures with heating rate for DH36 material.

***Continuous Cooling Transformation Diagrams***

CCT diagrams, assembled from dilatometry of DH36 thermally cycled to peak temperatures representative of the four selected HAZ regions, are given in **Figures 10-13**. The $A_{c1}$ and $A_{c3}$ temperatures labeled on the CCT diagrams are averages calculated from the individual $A_{c1}$ and $A_{c3}$ values for all of the specimens. The black curves are the actual specimen cooling curves. The target cooling rates for all specimens except those cooled at 200 °C/s (360 °F/s) were maintained through the on-cooling phase transformations. The latent heat released during transformation slightly affected the cooling rate during the 200 °C/s (360 °F/s) tests, such that the target cooling rate was maintained until the start of the

transformation, but was slowed by about 15% as the transformation occurred. The raw data for these figures are given in **Tables9-12** of **Appendix B**, and the individual dilation curves are given in **Figures 37-61** of **Appendix B**. Due to time and scope limitations, all reported data are the result of single tests. The only exception to this is a duplicate specimen heated to a peak temperature of 1000 °C (1832 °F) and cooled at 1 °C/s (1.8 °F/s). The error bars shown for this data point in the following figures represent one standard deviation from the average of the two tests.

The colored symbols in **Figures 10-13** correspond to the start and finish temperatures for the various on-cooling phase transformations. Each simulated HAZ region was subject to three regimes of on-cooling transformation start temperatures across the cooling rate range assessed in this work. The first occurred at high temperatures (650 to 750 °C [1202 to 1382 °F]) and is denoted in **Figures 10-13** by blue square symbols. The start of this transformation generally occurred near $A_{c1}$, though it decreased slightly with increasing peak temperature and increasing cooling rate. For all four peak temperatures, this transformation starts above $A_{c1}$ at the slowest cooling rate (i.e., the closest to equilibrium cooling). The second type of transformation identified is indicated by red circle symbols. This transformation generally started about 100 to 150 °C (180 to 270 °F) below the start of the higher temperature transformation and about 20 to 40 °C (36 to 72 °F) prior to the completion of austenite decomposition. It appeared to follow the same trends as the high temperature transformation with respect to peak temperature and cooling rate, but was not observed for cooling rates above 10 °C/s (18 °F/s) in any specimen. The third transformation regime identified in the CCT diagrams, indicated as green triangle symbols, generally started at temperatures of 500 to 600 °C (932 to 1112 °F) and was only observed at cooling rates of 100 °C/s (180 °F/s) and higher. The start and finish temperatures vary minimally for a given peak temperature, but they both appear to decrease with increasing peak temperature. Identification of these transformations is discussed in more detail below, but for interpretation of the diagrams presented in **Figures 10-13**, the blue, red, and green symbols reflect ferrite, pearlite, and bainite transformations, respectively.

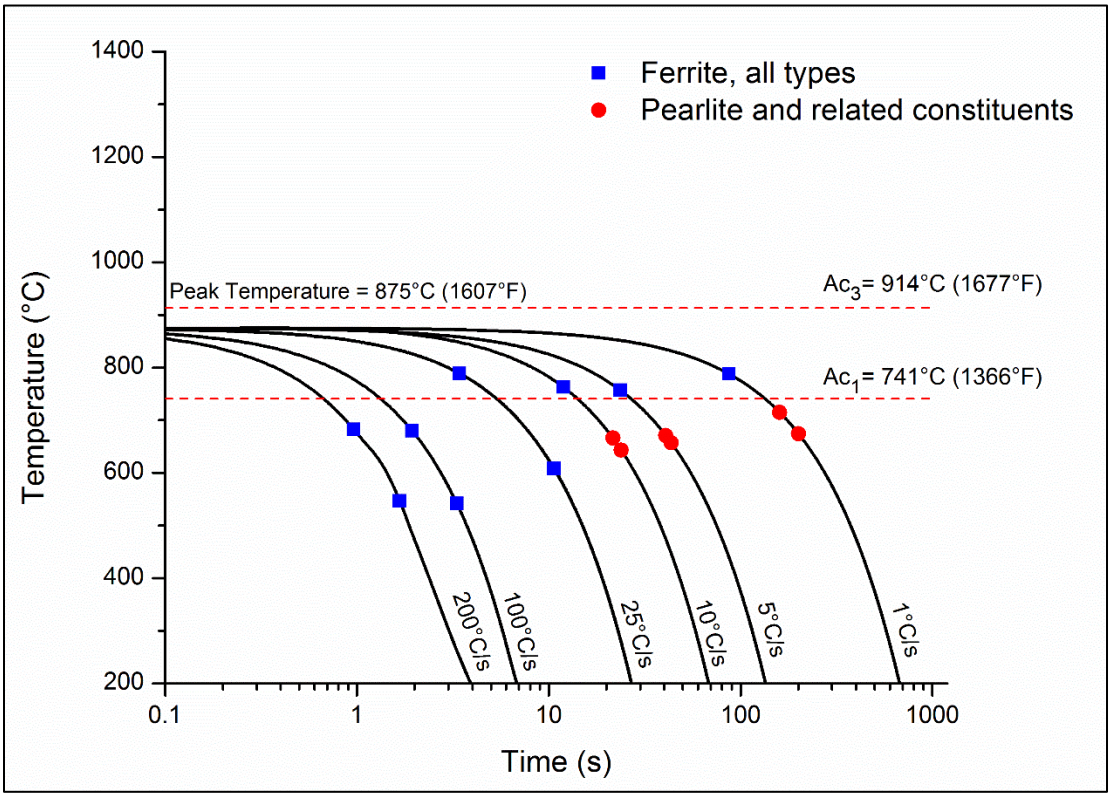


**Figure 10**. CCT diagram for DH36 heated to peak temperature of 875 °C (1607 °F).

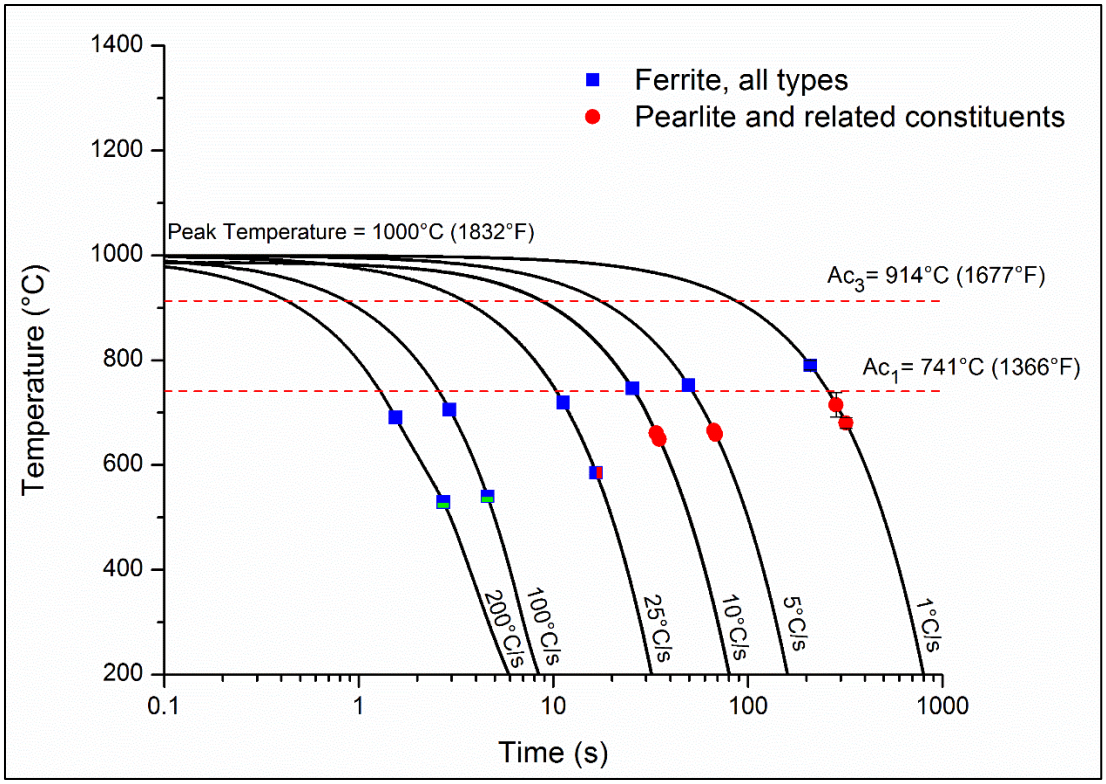


**Figure 11.** CCT diagram for DH36 heated to peak temperature of 1000 °C (1832 °F).

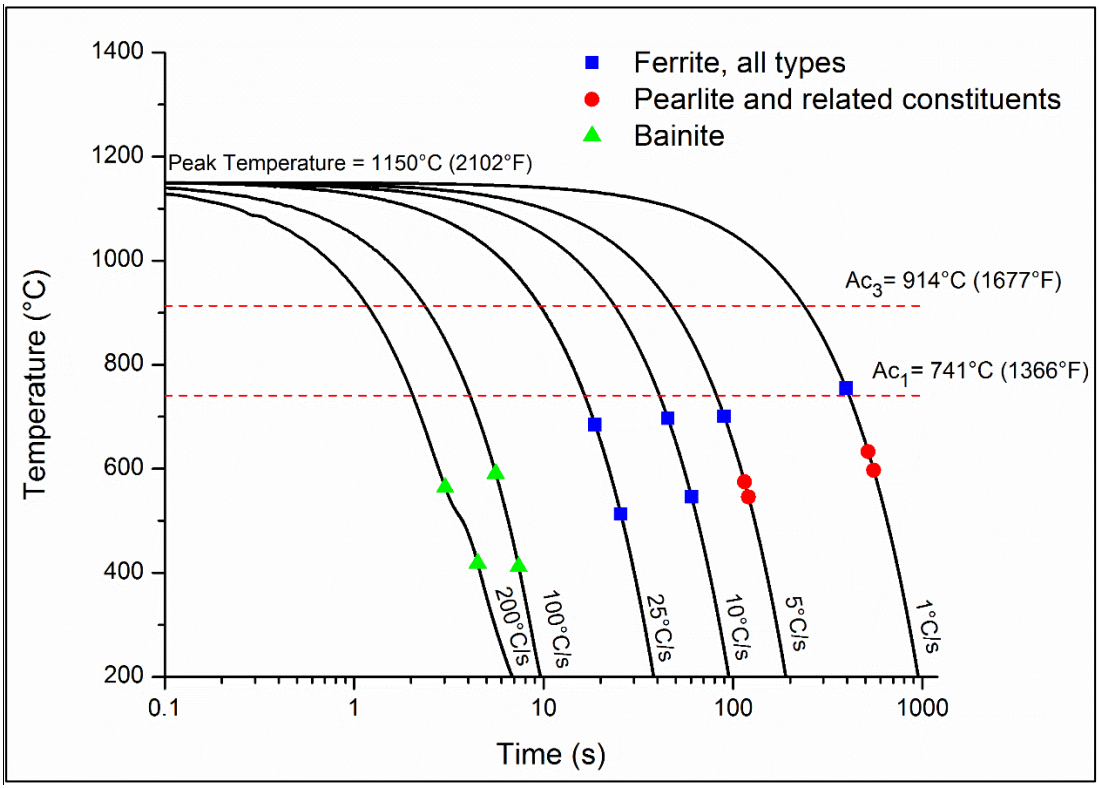


**Figure 12.** CCT diagram for DH36 heated to peak temperature of 1150 °C (2102 °F).

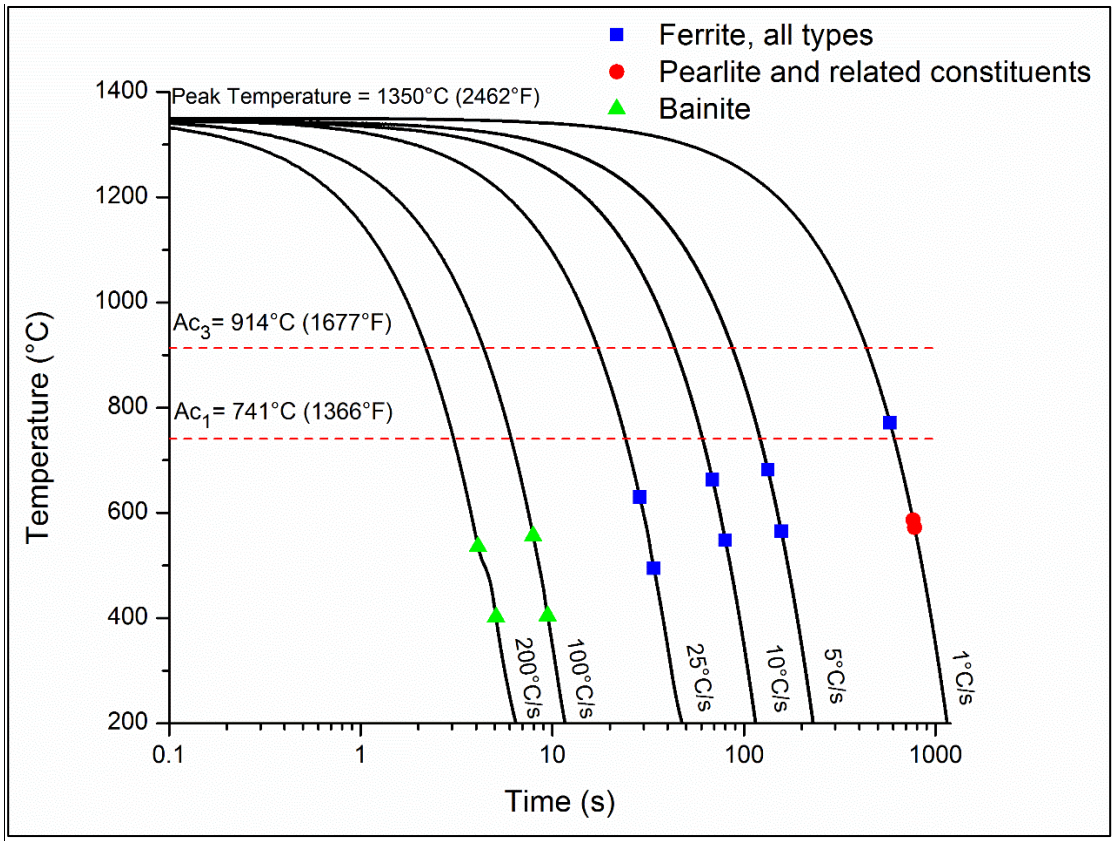


**Figure 13.** CCT diagram for DH36 heated to peak temperature of 1350 °C (2462 °F).

The effects described above are summarized in an alternate way in **Figures 14-17**. **Figure 14** gives the variation in transformation start temperature for the ferrite transformation as a function of peak temperature and cooling rate. As shown, for a given cooling rate, increasing the peak temperature generally suppresses the onset of the transformation, resulting in lower start temperatures. This most likely occurs because prior austenite grain (PAG) size increases with increasing peak temperature, resulting in less grain boundary area and therefore fewer nucleation sites for transformation. The onset of transformation is additionally suppressed by undercooling as cooling rate is increased. As a result, the difference in transformation start temperature between samples cooled at 5 to 25 °C/s (9 to 45 °F/s) increases from 65 to 141 °C (117 to 254 °F) when the peak temperature is increased from 875 to 1350 °C (1607 to 2462°F).

Another notable behavior shown in **Figure 14** is the relative lack of variation in transformation start temperature for the specimens cooled at 1 °C/s (1.8 °F/s). The average transformation start temperature for the 1 °C/s specimens is 775 °C (1427 °F). This is substantially lower than the Thermo-Calc predicted equilibrium value of 856 °C (1573 °F), which indicates that 1 °C/s (1.8 °F/s) cooling is still far from slow enough to use equilibrium calculations to predict the phase transformations. However, it does appear to be slow enough to reduce the sensitivity of this transformation to peak temperature (i.e., PAG size). In addition, the measured transformation start temperature is shown to be relatively insensitive to cooling rate for specimens heated to 875 °C (1607 °F). As given in **Table 9**, the variation between specimens cooled at 1 to 25 °C/s (1.8 to 45 °F/s) is 31 °C (56 °F).

**Figure 15** shows that the pearlite transformation behaved in a similar manner to that of ferrite, and decreases in the transformation start temperature were measured for both increasing cooling rates and increasing peak temperatures. However, in this case, the specimens cooled at 1 °C/s (1.8 °F/s) displayed a

much more apparent dependence on peak temperature than was observed in **Figure 14**. Finally, **Figure 17** shows how the measured transformation behavior for bainite varied. The start temperature increased slightly from the simulated low temperature FGHAZ to the high temperature FGHAZ before dropping slightly in the CGHAZ specimens. Overall, however, the start temperature for this transformation was significantly less variable than those of ferrite and pearlite.

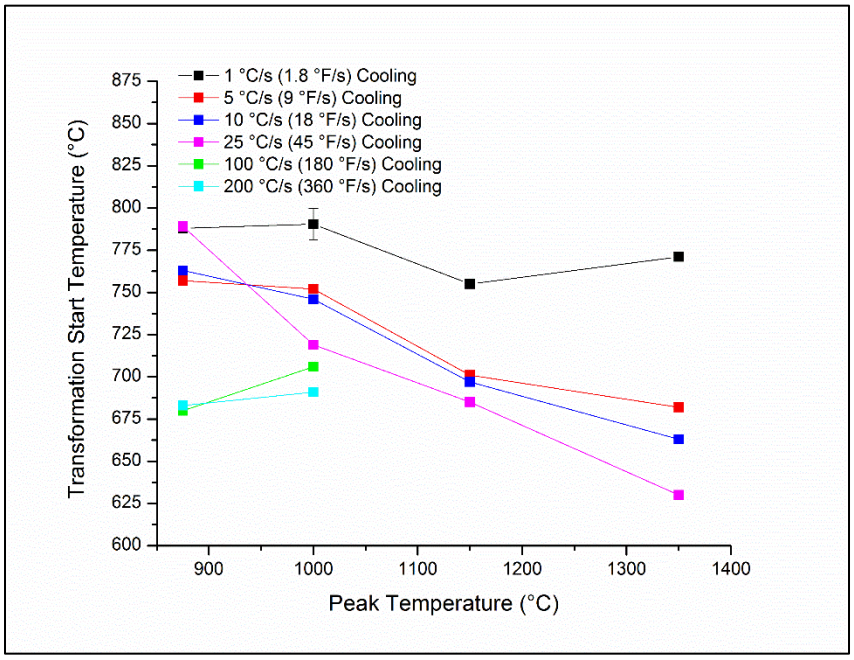


**Figure 14.** Variation of start temperature for the ferrite transformation shown in **Figures 10-13**.

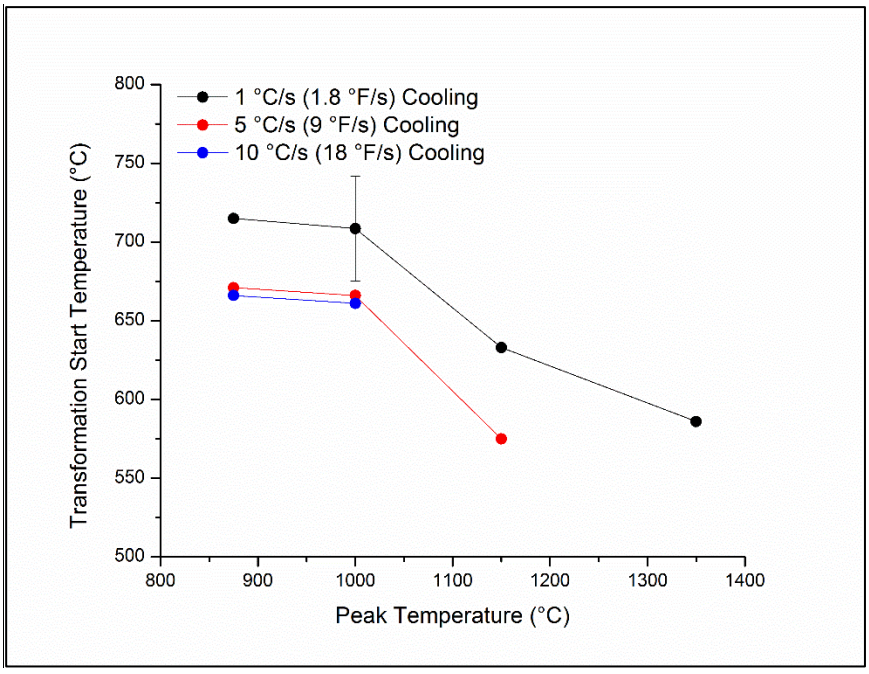


**Figure 15.** Variation of start temperature for the transformation to pearlite and related constituents shown in **Figures 10-13**.

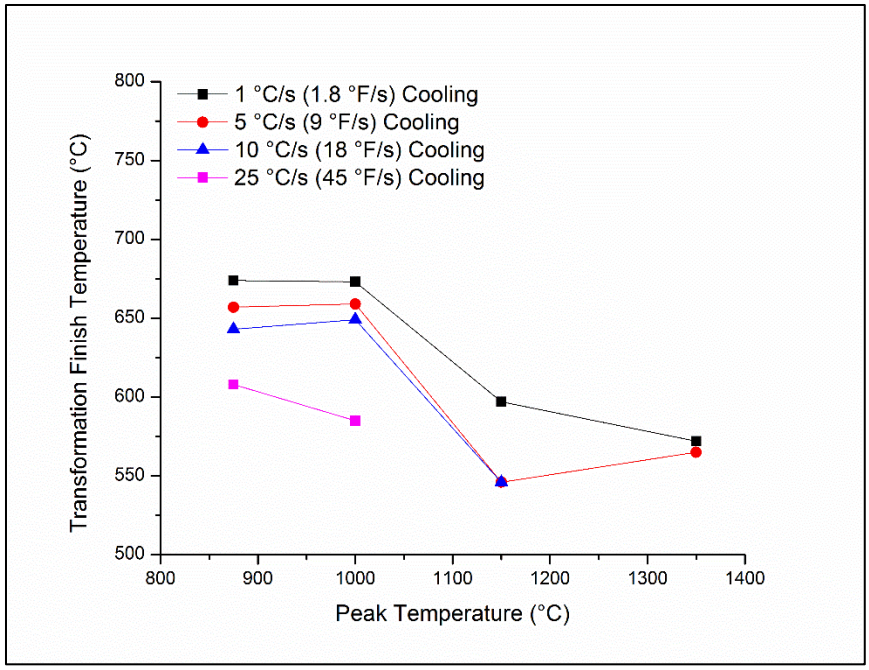


**Figure 16.** Variation of finish temperature for the pearlite and related constituent transformation shown in **Figures 10-13**.

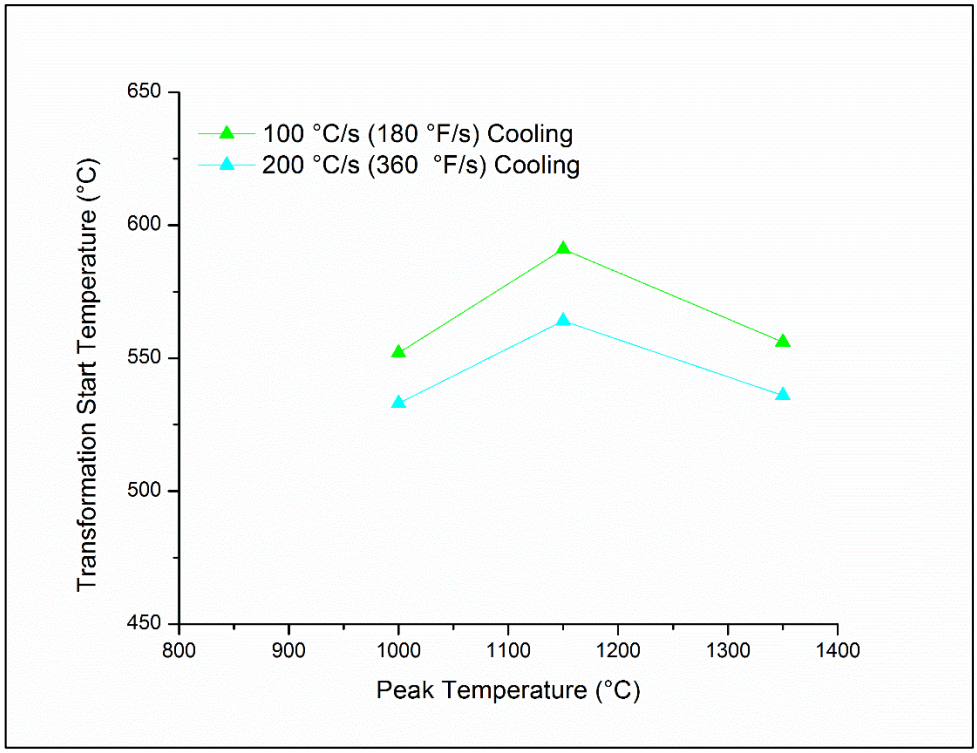


**Figure 17.** Variation of start temperature for the bainite transformation shown in **Figure 12-13**.

In order to confidently establish the identities of the on-cooling phase transformations, LOM was performed on all dilatometry specimens, and select specimens were analyzed via SEM. Micrographs collected from the dilatometry specimens are given in **Figures 62-74** of **Appendix C.** Additionally, the

measured microhardness for each specimen is given in **Figure 18** below and **Table 13** of **Appendix D**. For this discussion, the following definitions for the morphology of microstructural constituents are adopted [26] [27] [28] [29] [30]. The typical definitions for crystal structure and composition of the constituents are assumed.

*Primary ferrite ($F_P$)* – Carbide-free grain boundary or intragranular allotriomorphic ferrite
*Widmanstätten ferrite with second phase ($WF_{SP}$)* –High aspect ratio ferrite with either aligned or unaligned carbide
*Acicular ferrite (AF)* – Fine, interlocking structure formed by impingement of multiple Widmanstätten plates growing from intragranular inclusions
*Bainitic ferrite ($F_B$)* – Lath- or plate-like ferrite with either aligned or unaligned carbide
*Pearlite (P)* – Aggregate of discrete ferrite and cementite particles. Can manifest as alternating lamellae in classical pearlite or as a non-lamellar ferrite-carbide aggregate sometimes termed degenerate pearlite or ferrite-carbide aggregate [29]
*Unclassified constituent (U)* – Non-lamellar clustering of constituents of unidentified composition
*Bainite (B)* – General term for fine aggregates of ferrite laths or plates and cementite particles
*Upper bainite ($B_U$)* – Bainite consisting of fine (less than 0.5 μm wide) ferrite plates with carbide precipitation limited to the interlath boundaries

The microstructures of specimens heated to a peak temperature of 875 °C (1607 °F) are shown in **Figure 62**. These microstructures are intended to be representative of the ICHAZ, wherein only a partial transformation to austenite occurs on heating. This partial transformation is expected to occur via austenite nucleation at the pearlite colonies as the cementite solvus temperature is exceeded and austenite-stabilizing carbon is released into solution [28]. The specimen subjected to a cooling rate of 1 °C/s (1.8 °F/s) consisted of primary ferrite ($F_P$) and pearlite (P) which were very similar in appearance to those observed in the base material. The amount of pearlite seen in this specimen was small because the carbon content in DH36 is low. The pearlite reaction is promoted by rejection of carbon out of the ferrite and concomitant supersaturation of the austenite with carbon during cooling. In the case of a low carbon hypoeutectoid steel like DH36, the ferrite transformation nears completion prior to the solubility limit of carbon in austenite being exceeded. The final pearlite fraction would therefore be expected to be small and the pearlite transformation range during continuous cooling would be expected to be narrow, as observed.

A third, light-etching constituent was observed to form in addition to the $F_P$ and P in specimens with cooling rates from 5 to 25 °C/s (9 to 45 °F/s). This constituent exhibited significantly less etching contrast than the areas identified as pearlite in the base material and 1 °C/s (1.8 °F/s) specimen but was frequently observed adjacent to pearlite colonies. This consistency in distribution suggests that locally carbon-rich regions may be a prerequisite for its formation, as is the case for pearlite. It was interrogated at higher magnifications via SEM as shown in **Figure 63-Figure** 64. As shown, the constituent does not appear to contain ferrite and is therefore consistent with neither classical lamellar pearlite nor other pearlite morphologies (e.g., degenerate). Also shown by **Figure 63-Figure** 64 is evidence of an association between increased cooling rate and a qualitative shift from primarily P to primarily light-etched constituent within the $F_P$ matrix. This implies a dependency on undercooling. **Figure 69** demonstrates an apparent transition between the cementite portion of granular pearlite and the unidentified constituent, further implying a strong association with high carbon content, but no carbides could be resolved via SEM. The slow cooling rates and high transformation temperatures would typically preclude bainitic or martensitic transformation products in DH36 steel, but solute segregation—particularly in the case of carbon—could create locally hardenable regions and thus transformation products such as martensite-austenite constituent cannot be ruled out without further investigation. Further analysis is required to positively identify the constituent, thus at this time it is simply referred to as an unclassified constituent (U). Its low volume fraction and similar formation conditions to pearlite

suggest a small effect on overall material properties, therefore its presence will be noted in the discussion portion of this report but it will not represented in the *SYSWELD* database.

The specimens cooled at 100 and 200 °C/s (180 and 360 °F/s, **Figures 62e-f**) contain remnant primary ferrite from the base metal microstructure, particles that appear to be dispersed carbides, and dark-etching areas. It is surmised that the dark-etching areas are located in the regions that transformed to austenite on heating. The identity of the dark-etching areas was not apparent from the LOM images, so SEM micrographs of them were acquired and are shown in **Figures 65** and **66.** They contain high aspect ratio constituents and what may be aligned carbides. Again, advanced characterization would be needed to confirm the identity of the presumed carbides. Because the measured transformation start temperatures for these specimens were high (approximately 675 °C [1247 °F]) and both their absolute hardness and the relative change in hardness over that of the 25 °C/s (45 °F/s) specimen were not very large (see **Figure 18**), the dark-etching areas are considered to be primarily Widmanstätten ferrite with second phase ($WF_{SP}$) [29]. The overall microstructures of the 100 and 200 °C/s (180 and 360 °F/s) specimens are therefore judged to be $F_P$ + $WF_{SP}$. It is possible that some portion of the dark-etching areas in **Figures 62-66** are bainitic because of the carbon enrichment (and associated increase in hardenability) described above. However, this cannot be determined for certain without more detailed characterization. **Table 4** gives the measured fractions of each microstructural constituent for these specimens. Ferrite, pearlite, and carbides are not tracked separately in *SYSWELD* databases, so for the purposes of inclusion into a database for that software, all ferrite and pearlite morphologies, along with the unclassified constituent, were grouped together.

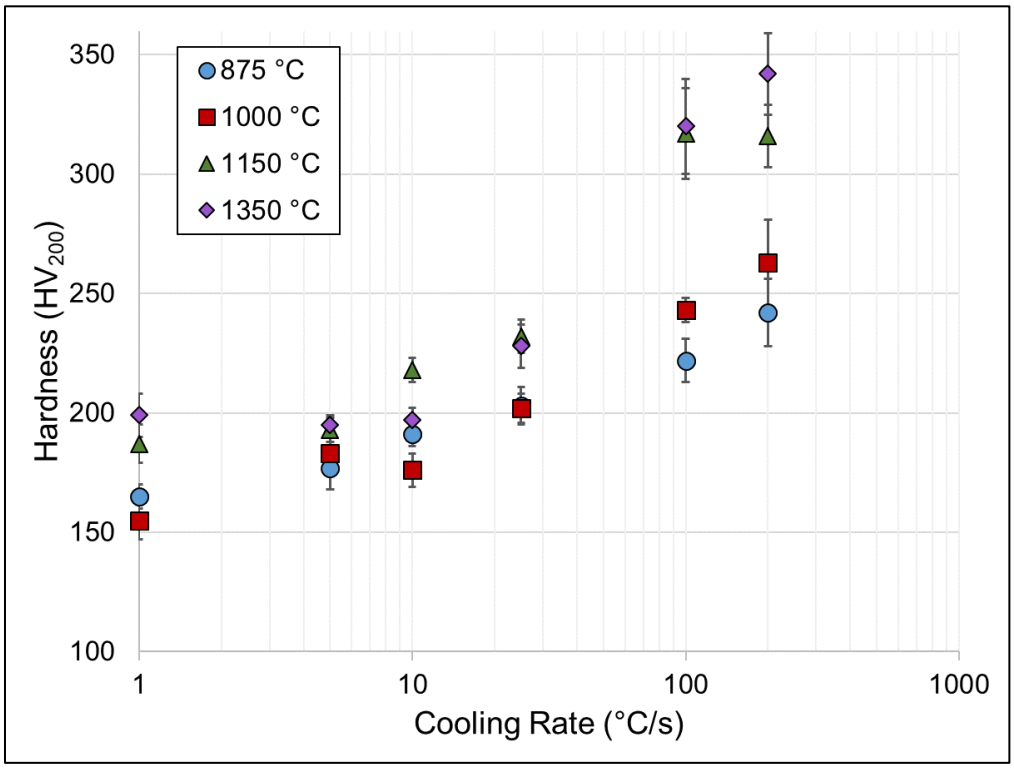


**Figure 18.** Measured Vickers microhardness for DH36 dilatometry specimens as a function of peak temperature and cooling rate. Error bars are one standard deviation. The number of indents per specimen ranged from 12 to 300, as given in **Table 13**.

Micrographs from DH36 specimens heated to 1000 °C (1832 °F) are shown in **Figure 67**. Cooling at 1 °C/s (1.8 °F/s) resulted in a ferrite-pearlite microstructure that was similar to the base metal.

Increasing the cooling rate to 5 and 10 °C/s (9 and 18 °F/s) introduced the unknown constituent into the microstructure and shifted the pearlite morphology from lamellar to degenerate (**Figures 68-70**). At 25 °C/s (45 °F/s) cooling, the microstructure was entirely $F_P$ and U, with pearlite no longer identifiable. A distinct drop in the transformation finish temperature was observed, falling from 649 °C (1200 °F) in the 10 °C/s (18 °F/s) specimen to 585 °C (1085 °F) in the 25 °C/s (45 °F/s) specimen. Comparison of this transformation finish temperature with the calculated equilibrium bainite start temperature of 586 °C (1087 °F) suggests that this is not a bainitic transformation product, particularly when the effects of undercooling are considered (i.e., the bainite start temperature in a rapidly cooled sample is expected to be below the calculated equilibrium temperature). Also shown in **Figure 67b-d** is an increasing fraction of very fine (less than 5 μm diameter) ferrite grains for specimens cooled between 1 °C/s (1.8 °F/s) and 25 °C/s (45 °F/s). These likely form because 1000 °C (1832 °F) is only slightly above $Ac_3$, so as cooling rate increases the newly nucleated austenite grains do not have sufficient time to reach their equilibrium size. As shown in **Figure 18**, the hardness of these four specimens was slightly lower than those of the 875 °C (1607 °F) specimens cooled at the same rates. At 100 and 200 °C/s (180 and 360 °F/s) cooling, the resultant microstructures are significantly different than those observed in the 875 °C (1607 °F) specimens because of the complete transformation of the starting microstructure to austenite. As shown in **Figure 67**, they appear to contain three separate constituents – polygonal ferrite grains (classified here as $F_P$), high aspect ratio ferrite with what appears to be intergranular second phase ($WF_{SP}$), and islands of a darker etching constituent, which are more prevalent in the 200 °C/s (360 °F/s) specimen. As in the case of simulated ICHAZ specimens, the transformation start temperature for these rapidly cooled specimens is most consistent with a ferritic reaction, which is consistent with the presence of $F_P$ and $WF_{SP}$. Targeted microhardness measurement of the dark etching constituent indicated a hardness in excess of 300 $HV_{25}$, which was substantially harder than the averaged values for the 100 and 200 °C/s (180 and 360 °F/s) specimens. It is therefore possible that a small amount of bainite or martensite formed in specimens subjected to these combinations of peak temperature and cooling rate. A more definitive discussion of which constituent this was likely to be can be found below. **Table 5** shows the measured fractions of each microstructural constituent for the 1000 °C (1832 °F) specimens.

Representative images from the specimens heated to 1150 °C (2102 °F) are given in **Figure 72**. As shown, 1 °C/s (1.8 °F/s) cooling has resulted in a ferritic matrix with some lamellar pearlite and a dispersion of discrete particles (likely carbides) located mostly along the grain boundaries. As anticipated from increased PAG size with increasing peak temperature, the resultant ferrite grains are much larger than were observed in specimens heated to lower peak temperatures. During cooling at 5 °C/s (9 °F/s), the formation of pearlite colonies appears to be almost completely suppressed in favor of islands of particles that are in some cases aligned along ferrite grain boundaries. The ferritic matrix is now a mixture of allotriomorphic and idiomorphic $F_P$ with areas of $WF_{SP}$. The differences observed between this microstructure and those at the same cooling rate but lower peak temperatures are likely tied to the PAG size. As shown in **Figure 14**, the increase in PAG size has led to a 50 °C (90 °F) decrease in the transformation start temperature, which would be expected to favor a Widmanstätten-type reaction [29]. Additionally, the large decrease (100 °C [180 °F]) in the pearlite/carbide transformation noted above (**Figure 15**) occurred beginning with specimens heated to this peak temperature. This behavior is likely related to both the decreased number of nucleation sites (grain boundaries) and the extent of carbon diffusion. When the DH36 base metal microstructure is heated above $Ac_1$, the pearlite will dissolve. At temperatures close to the dissolution temperature, this carbon will remain relatively local to the position of the original pearlite colony. It will therefore need to diffuse a shorter distance to re-form $Fe_3C$ during cooling. As peak temperature increases, so will the carbon diffusivity, such that for specimens heated to 1150 °C (2462 °F) and above, the carbon is likely to be much more homogeneously distributed in the austenite [28]. As a result, the austenite-to-pearlite/carbide transformation will be pushed to lower temperatures as the peak temperature increases and larger carbon diffusion distances are required to allow their formation. Slow cooling (e.g., 1 °C/s [1.8 °F/s]) also increases the amount of time spent above $Ac_3$ and permits further carbon homogenization. The pearlite transformation for specimens cooled at 1 °C/s

(1.8 °F/s) would therefore be expected to be dependent on peak temperature, as shown in **Figure 15**. The hardness of these microstructures is slightly higher than measured for the simulated low-temperature FGHAZ specimens.

Similar decreases in transformation start temperature were observed in the 10 and 25 °C/s (18 and 45 °F/s) samples relative to their lower peak temperature counterparts. The microstructures for both of these specimens appear to be primarily $WF_{SP}$. A higher degree of undercooling prior to the onset of transformation for the 25 °C/s (45 °F/s) specimen has given rise to finer ferrite laths, some areas consistent in morphology with acicular ferrite, and a higher hardness. A small amount of fine carbide aggregates were noted along ferrite grain boundaries in the 10 °C/s (185 °F/s) sample. There was no pearlite or carbide aggregate observed in the 25 °C/s (45 °F/s) sample. The microstructures of the 100 and 200 °C/s (180 and 360 °F/s) specimens are distinguishable from the others described so far by three observations: the scale of the laths is much finer (2 to 3 μm), the transformation start temperature is much lower (approximately 575 °C [1067 °F]), and the hardness is much higher (316 HV). Given the cooling rates associated with these transformations, they were assumed to be bainitic or martensitic.

Various constitutive equations for predicting the start temperatures for bainite and martensite transformations based on alloy chemistry are available in the literature [31] [32]. Such models are generally oversimplifications and often are only accurate for alloys similar to those used to create them, but they offer the ability to gather an initial understanding of whether this intermediate temperature transformation was likely to be bainite or martensite. As such, the models developed by Capdevilla et. al. [33] and Kirkaldy [34] were applied to the DH36 composition given in **Table 3**:

$$M_s = 491.05 - 302.6w_C - 30.6w_{Mn} - 16.6w_{Ni} - 8.9w_{Cr} + 2.4w_{Mo} - 11.3w_{Cu} + 8.58w_{Co} + 7.4w_W - 14.5w_{Si} \quad \textbf{(5)}$$

$$B_s = 656 - 57.7w_C - 75w_{Si} - 35w_{Mn} - 15.3w_{Ni} - 32w_{Cr} - 41.2w_{Mo} \quad \textbf{(6)}$$

where $M_s \equiv$ martensite start temperature (°C)
$B_s \equiv$ bainite start temperature (°C)
$w_i \equiv$ concentration of element $i$ (wt%)

From **Equations 5** and **6**, the $M_s$ and $B_s$ temperatures for DH36 are predicted to be 425 and 586 °C (797 and 1087 °F), respectively. The measured transformation start temperatures for the 100 and 200 °C/s (180 and 360 °F/s) specimens were 591 and 564 °C (1096 and 1047 °F), respectively. In addition, upon inspection of the relevant dilation curves in **Appendix B,** it is seen that this transformation does not exhibit the same very high transformation rate common to martensitic transformations [29]. It is therefore concluded that the transformation observed in the 100 and 200 °C/s (180 and 360 °F/s) specimens cooled from 1150 °C (2102 °F) was bainitic. Finally, since the measured transformation start temperature is well above what is typically expected from lower bainite (250 to 400 °C [482 to 752 °F] [27]) and the LOM-level morphology is generally more consistent with that of upper bainite, it is surmised that the transformation product is $B_U$.

This analysis indicates that the hard, dark-etching constituent described above in specimens heated to 1000 °C (1832 °F) and cooled at 100 and 200 °C/s (180 and 360 °F/s) (**Figure 67**) was likely also bainite. However, because of the difficulty in observing the morphology of those small colonies, they are denoted here as simply ‘bainite’ (B). **Table 6** shows the measured fractions of each microstructural constituent for the 1000 °C (1832 °F) specimens.

**Figure 73** presents micrographs of the dilatometry specimens heated to 1350 °C (2462 °F). As shown, cooling at 1 °C/s (1.8 °F/s) has created a microstructure consisting of areas of primary ferrite,

pearlite colonies, and very coarse $WF_{SP}$ with what appear to be aligned carbides. Cooling at both 5 and 10 °C/s (9 and 18 °F/s) produced a primarily coarse $WF_{SP}$ microstructure with some areas of $F_P$. The onset of $WF_{SP}$ at slower cooling rates was again likely driven by increases in PAG size, which resulted in more undercooling prior to the initial on-cooling transformation, as shown in **Figure 14**. The hardness of specimens cooled at these three rates was very similar (**Figure 18**). The microstructure of the specimen cooled at 25 °C/s (45 °F/s) is primarily $WF_{SP}$, as was observed in the high temperature FGHAZ at the same cooling rate. Areas of AF also appear to be present in this specimen. Finally, the microstructure of the 100 and 200 °C/s (180 and 360 °F/s) specimens appears consistent with their 1150 °C (2402 °F) counterparts and are identified as upper bainite. The hardness of these microstructures are in line with those described above for the simulated high-temperature FGHAZ, and a slight decrease in transformation start temperature with peak temperature was observed, as previously reported in [35]. **Table 7** shows the measured fractions of each microstructural constituent for the 1350 °C (2462 °F) specimens.

**Table 4.** Measured phase fraction of DH36 CCT specimens thermally cycled to a peak temperature of 875 °C (1607 °F)

| Cooling Rate | | Peak Temperature = 875 °C (1607 °F) | | |
|---|---|---|---|---|
| °C/s | °F/s | F + P | B | M |
| 1 | 1.8 | 1 | 0 | 0 |
| 5 | 9 | 1 | 0 | 0 |
| 10 | 18 | 1 | 0 | 0 |
| 25 | 45 | 1 | 0 | 0 |
| 100 | 180 | 1 | 0 | 0 |
| 200 | 360 | 1 | 0 | 0 |

**Table 5.** Measured phase fraction of DH36 CCT specimens thermally cycled to a peak temperature of 1000 °C (1832 °F)

| Cooling Rate | | Peak Temperature = 1000 °C (1832 °F) | | |
|---|---|---|---|---|
| °C/s | °F/s | F + P | B | M |
| 1 | 1.8 | 1 | 0 | 0 |
| 5 | 9 | 1 | 0 | 0 |
| 10 | 18 | 1 | 0 | 0 |
| 25 | 45 | 1 | 0 | 0 |
| 100 | 180 | 0.60 | 0.40 | 0 |
| 200 | 360 | 0.40 | 0.60 | 0 |

**Table 6.** Measured phase fraction of DH36 CCT specimens thermally cycled to a peak temperature of 1150 °C (2102 °F)

| Cooling Rate | | Peak Temperature = 1150 °C (2102 °F) | | |
|---|---|---|---|---|
| °C/s | °F/s | F + P | B | M |
| 1 | 1.8 | 1 | 0 | 0 |
| 5 | 9 | 1 | 0 | 0 |
| 10 | 18 | 1 | 0 | 0 |
| 25 | 45 | 1 | 0 | 0 |
| 100 | 180 | 0 | 1 | 0 |
| 200 | 360 | 0 | 1 | 0 |

**Table 7.** Measured phase fraction of DH36 CCT specimens thermally cycled to a peak temperature of 1350 °C (2462 °F)

| Cooling Rate | | Peak Temperature = 1350 °C (2462 °F) | | |
|---|---|---|---|---|
| °C/s | °F/s | F + P | B | M |
| 1 | 1.8 | 1 | 0 | 0 |
| 5 | 9 | 1 | 0 | 0 |
| 10 | 18 | 1 | 0 | 0 |
| 25 | 45 | 1 | 0 | 0 |
| 100 | 180 | 0 | 1 | 0 |
| 200 | 360 | 0 | 1 | 0 |

The phase transformation information developed here is critically important for ensuring that weld simulation software can draw on thermo-physical and thermo-mechanical property information from the appropriate phases at the appropriate times during calculations. The results in **Figures 10-17** highlight the importance of developing multiple HAZ-related CCT diagrams.

## Weldment Microstructures

Metallographic specimens were removed from both weldments and analyzed in a manner similar to the Gleeble specimens. **Figure 19** shows representative light optical micrographs highlighting the microstructural differences across the HAZ regions for the fillet weld, and the average measured microhardness from three linear traverses across the fillet weld HAZ. Note that the HAZ region labels in **Figure 19** are to allow comparison of the relative hardness of the regions only and are not reflective of their actual width because of challenges associated with collecting hardness traverses perpendicular to the non-semicircular HAZ boundaries in thin plates. **Figure 20** presents similar information for the butt joint, except that the hardness measurements could not be averaged because of the complex thermal history associated with multi-pass welding on thin plate. Both welds demonstrate monotonically increasing HAZ hardness, as is common for plain carbon and low alloy steels and was observed in the dilatometry specimens (**Figure 18)**. The pass 1 ICHAZ and FGHAZ were on average approximately 10 to 15 HV harder than those of pass 2 as a result of reheating. The raw data points for **Figure 19** and **Figure 20** can be found in **Appendix D**.

The fillet weld hardness data was used for comparisons to the dilatometry results because, as a single pass weld, it was not subject to the complex microstructural evolution associated with reheating in the multi-pass butt joint. The fillet weld CGHAZ hardness fell between the hardness of the simulated CGHAZs cooled at 10 and 25 °C/s (18 and 45 °F/s). The average weldment FGHAZ hardness corresponded to that of a simulated cooling rate between 5 and 10 °C/s (9 and 18 °F/s). The average weld ICHAZ hardness was closest to that of the simulated ICHAZ cooled at 10 °C/s (18 °F/s).

**Figure 21** presents representative micrographs from the fillet weld. **Figure 21a** shows that the fusion zone was a mixture of primary ferrite (along prior austenite grain boundaries) and acicular ferrite. **Figures 21b-c** show that the CGHAZ and FGHAZ were mixtures of $F_P$ and $WF_{SP}$. The CGHAZ $F_P$ was more localized to the grain boundaries, and the $WF_{SP}$ appeared slightly coarser in the CGHAZ. **Figure 21d** shows that the fillet weld ICHAZ consisted of ferrite dispersed carbides and pearlite colonies. As such, the dilatometry specimen microstructures that most closely correspond with those observed in the fillet weld CGHAZ, FGHAZ, and ICHAZ are those associated with 10 °C/s (18 °F/s) cooling. This is in good agreement with the hardness measurements described above.

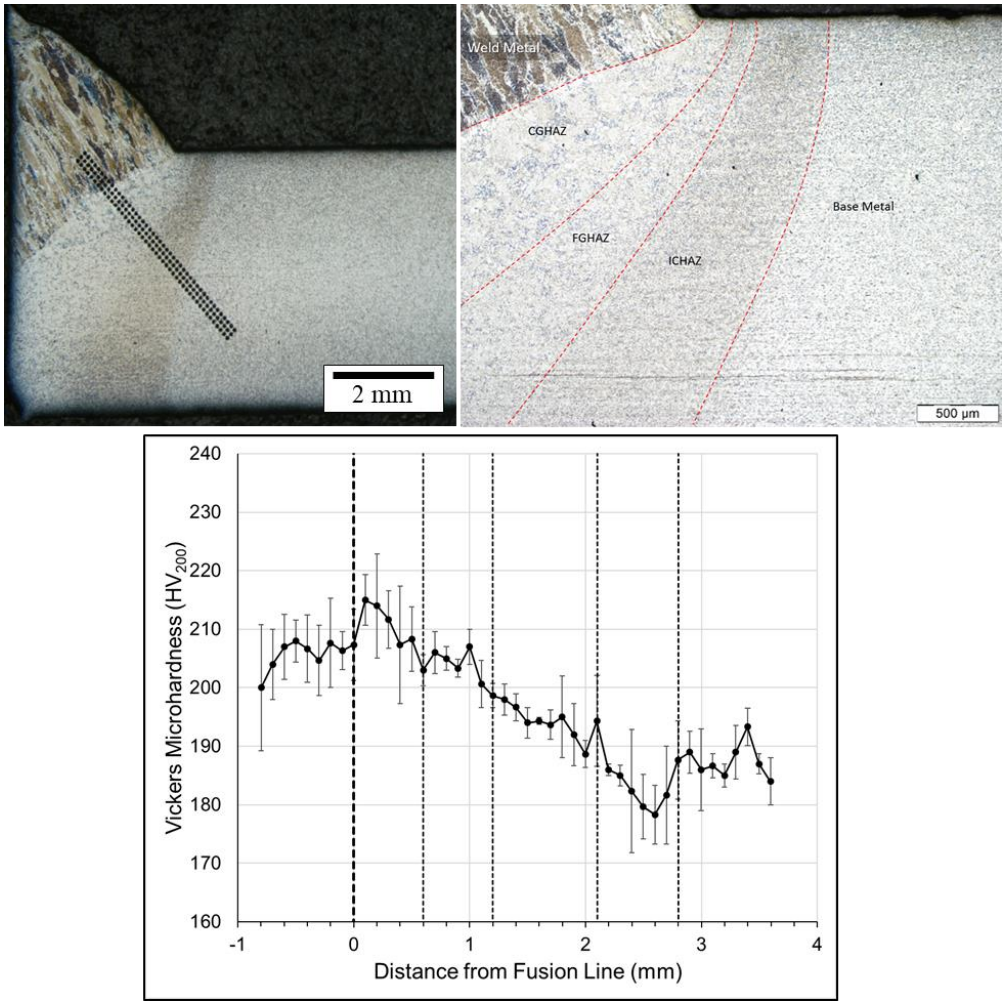


**Figure 19.** **(Top)** Light optical micrographs of the DH36 fillet weld showing the different HAZ regions and their approximate boundaries. **(Bottom)** Average Vickers microhardness across the three black lines in the top-left micrograph. Error bars are one standard deviation.

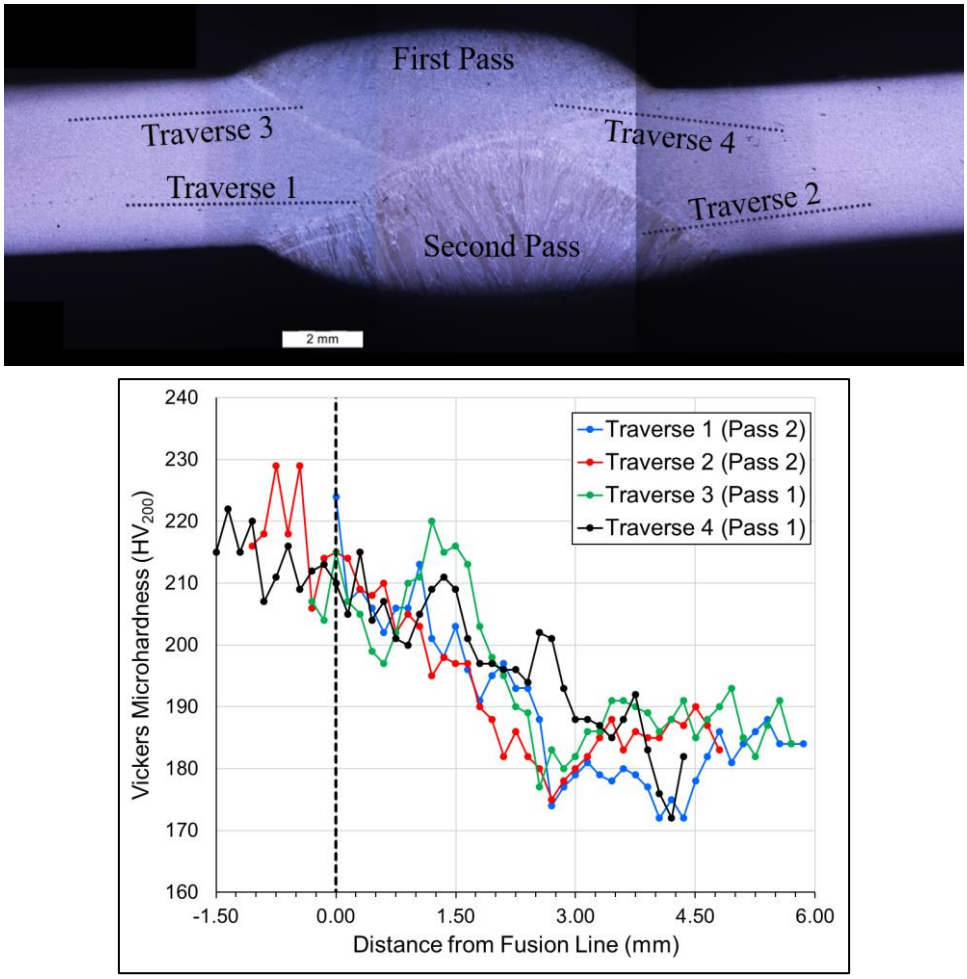


**Figure 20.** **(Top)** Light optical micrograph of the DH36 butt joint. **(Bottom)** Vickers microhardness traverses across the four black lines in the micrograph.

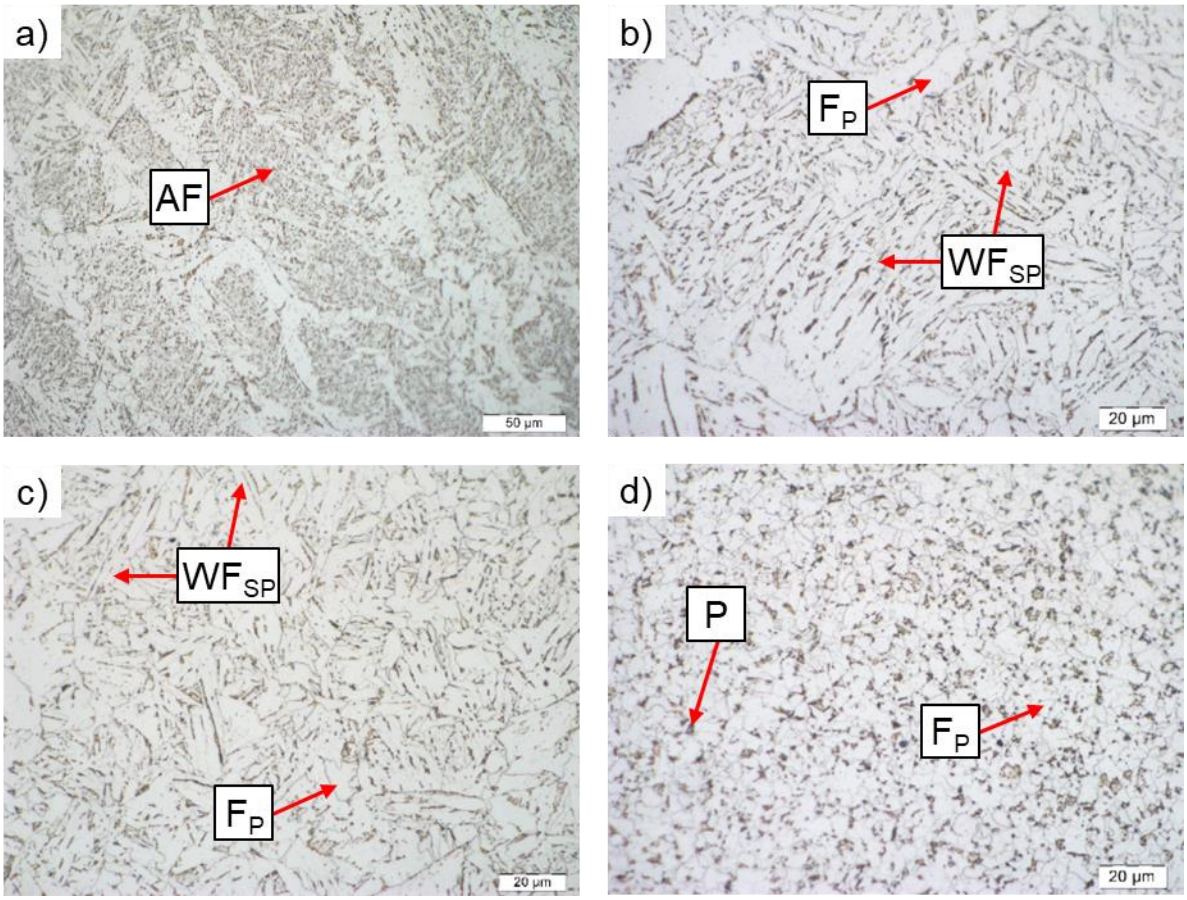


**Figure 21.** Representative light optical micrographs of the DH36 fillet weld **a)** fusion zone, **b)** CGHAZ, **c)** FGHAZ, and **d)** ICHAZ.

### Thermo-Physical Property Analysis

The CTE values measured from the dilation curves (n=11) were 15.6 x $10^{-6}$ ± 0.6 x $10^{-6}$ °$C^{-1}$ (8.7 x $10^{-6}$ ± 0.3 x $10^{-6}$ °$F^{-1}$) for the untransformed base metal below 650 °C (1202 °F) and 20.9 x $10^{-6}$ ± 2.1 x $10^{-6}$ °$C^{-1}$ (12.0 x $10^{-6}$ ± 1.2 x $10^{-6}$ °$F^{-1}$) for austenite above 950 °C (1742 °F). A representative graph showing the CTE measurement is given in **Figure 22**, and the raw data is included in **Appendix E**

Temperature-dependent density values are shown in **Figure 23**. A comparison dataset from a study conducted as part of a Navy Manufacturing Technology (ManTech) program with the Naval Metalworking Center from the mid-2000s is also included in the figure [36]. This data is labeled “CTC” for Concurrent Technologies Corporation, where the testing was conducted. Note that the comparison dataset from CTC was for DH36 controlled-rolled plate with a nominal thickness of 15.9 mm (5/8-in.). As shown, the density values generated in this work are approximately 3.5% higher than those measured by CTC. Since the slopes of the lines (i.e., the CTE) are nearly identical, this difference can be primarily attributed to a difference in the room temperature densities between the two studies.

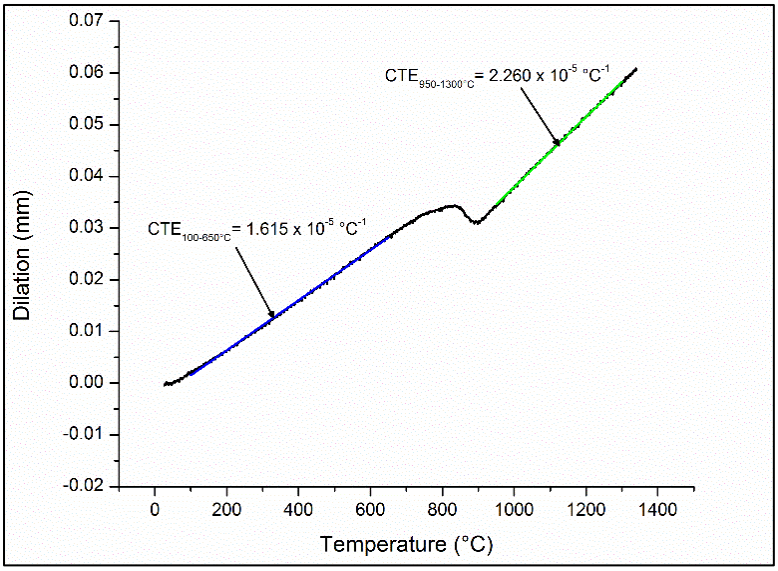


**Figure 22.** Representative on-heating dilatometry curve for DH36, showing typical CTE analysis and results.

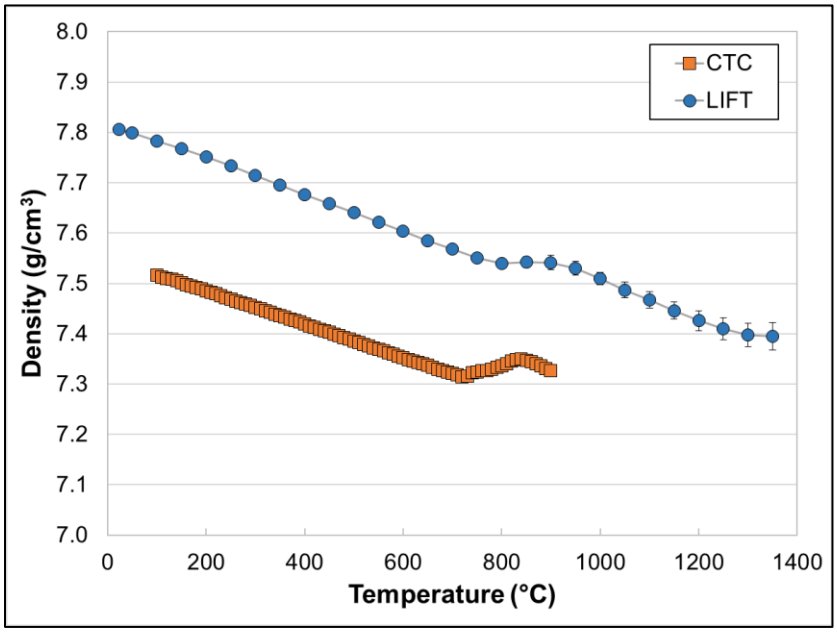


**Figure 23.** Density of DH36 steel as a function of temperature. LIFT data measured using analysis of Gleeble-based dilation curves in accordance with **Equations 2** and **3**. CTC data adapted from reference [36]. Error bars on LIFT data are one standard deviation from the mean of three tests.

The measured specific heat and thermal diffusivity data for DH36 can be found in **Figures 24-25**. The peaks or cusps in the data correspond to the effects of thermal energy absorption during phase transformations, particularly during the austenitic transformation between approximately 750 to 850 °C (1352 to 1562 °F) and the δ ferrite and melting transformations beginning around 1450 °C (2552 °F). The δ ferrite transformation is only visible in **Figure 24** (beginning at approximately 1340 °C [2444 °F]) and is missed by **Figure 25** because of the larger temperature increment between thermal diffusivity

measurements. Thermo-Calc equilibrium calculations predict a δ ferrite stability range of 1426 to 1466 °C (2599 to 2671 °F). As shown, the data from this program compare very well with the data generated in the Navy ManTech study.

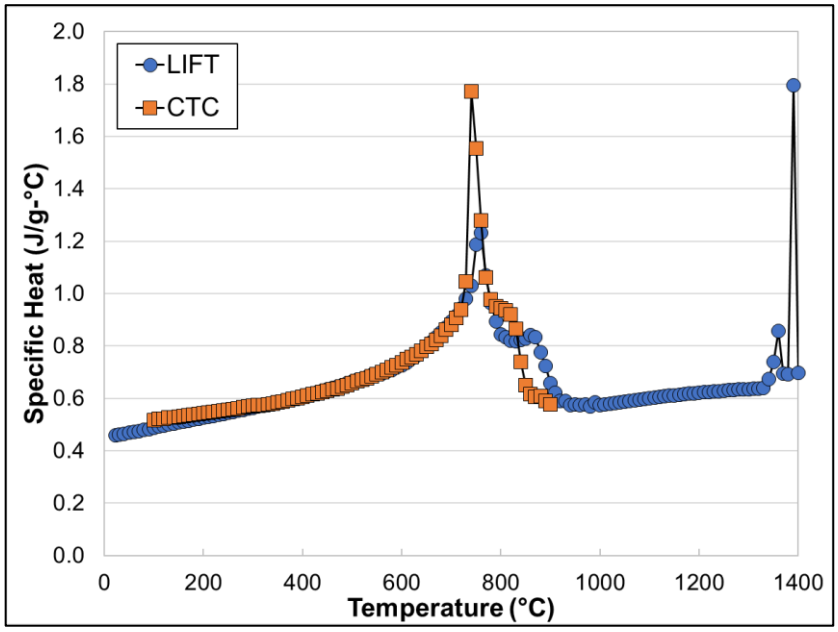


**Figure 24.** Measured specific heat for DH36 steel at various temperatures. CTC data adapted from reference [36].

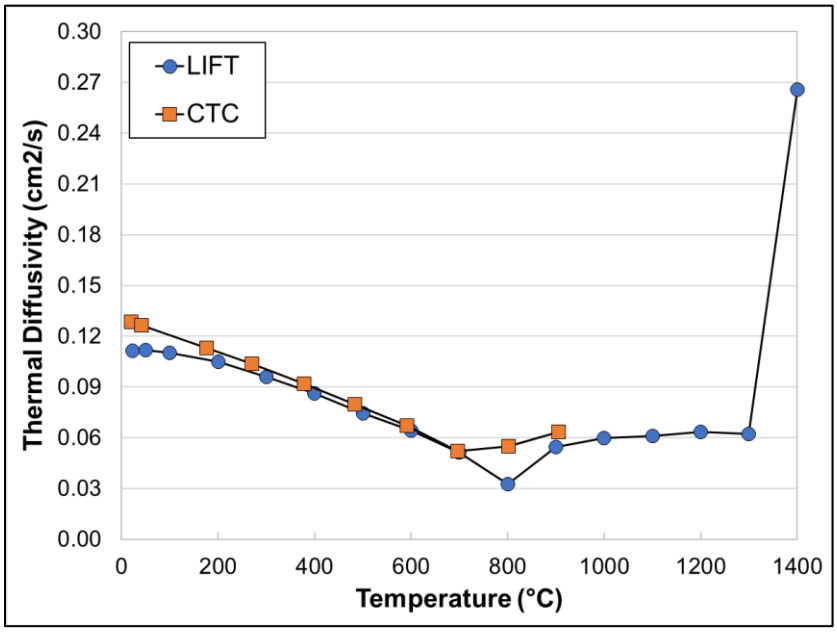


**Figure 25.** Measured thermal diffusivity for DH36 steel at various temperatures. CTC data adapted from reference [36].

Finally, the data from **Figures 23-25** were used in conjunction with **Equation 4** to calculate the temperature-dependent thermal conductivity as shown in **Figure 26**. Once again, the data coincides well

with the previous reporting from CTC. The raw data points for all of the thermo-physical property graphs can be found in **Appendix E**.

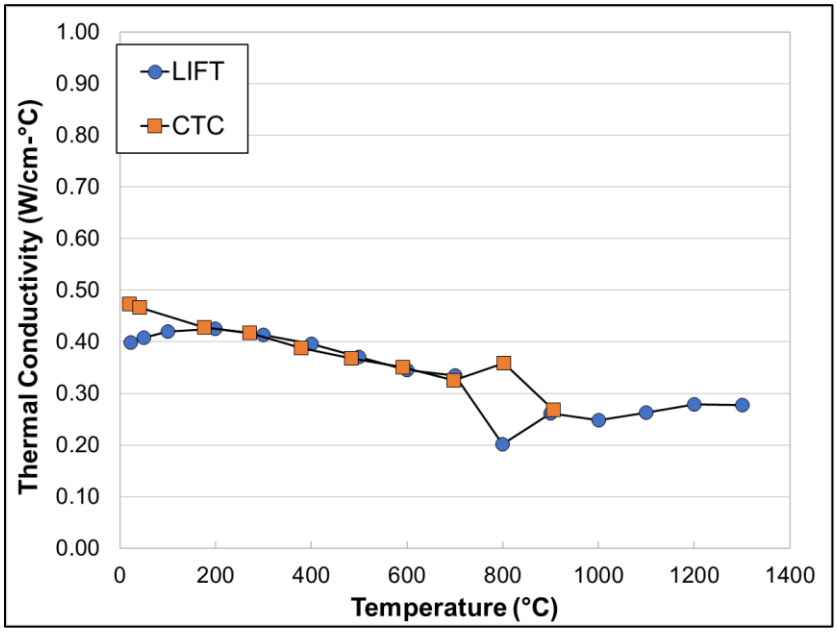


**Figure 26.** Calculated thermal conductivity for DH36 steel at various temperatures. CTC data adapted from reference [36].

### Thermo-Mechanical Property Analysis

**Figure 27** shows the values for elastic modulus as a function of temperature that were assumed in this work. The elevated temperature mechanical testing described above was performed in accordance with ASTM E21 [13] rather than the stricter ASTM E111 [37], which is prescribed when elastic modulus measurements are to be made. As such, it was determined that the experimentally measured elevated temperature elastic moduli were likely inaccurate. In order to provide elevated temperature modulus values for a DH36 property database, the data in **Figure 27** were adapted from the European standard for fire design of steel structures [38] [39]. Of the potential sources for this information, the European standard contained the most complete data covering temperatures relevant to this study. A room temperature elastic modulus of 210 GPa (30.5 Msi) was assumed [38]. It was also assumed that rigorously measured elastic moduli for DH36 steel would be very similar to data presented in **Figure 27** because elastic properties tend to be consistent within a given material class (e.g., steel). **Figure 28** shows the experimentally measured temperature-dependent 0.2% offset yield strength for DH36 base material, and **Figure 29** shows the measured temperature-dependent ultimate tensile strength (UTS). Comparison data for the measured yield strengths were found for AH36 grade plate in reference [40]. As expected, increased temperatures result in significant strength loss. At temperatures above 800 °C (1472 °F), the base metal microstructure is completely transformed to the weaker austenite phase, resulting in only minor differences in strength with increasing temperature.

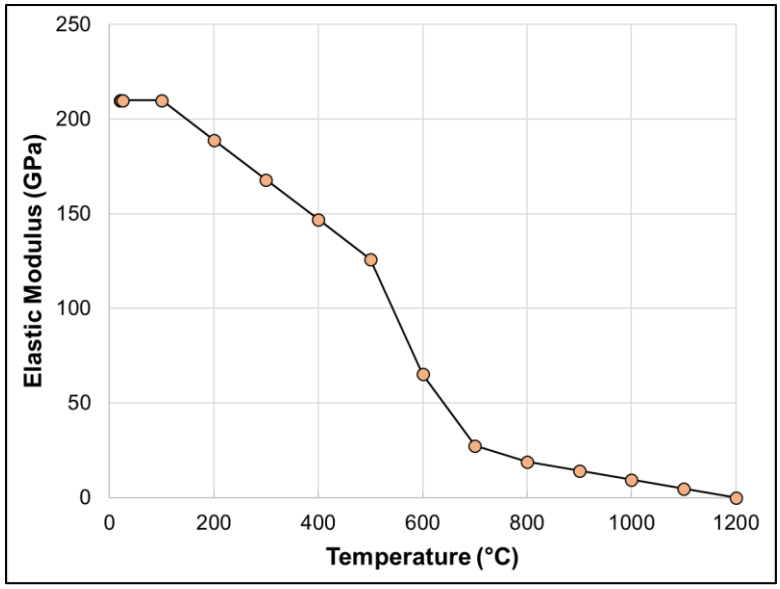


**Figure 27.** Assumed elevated temperature elastic modulus for DH36 steel.

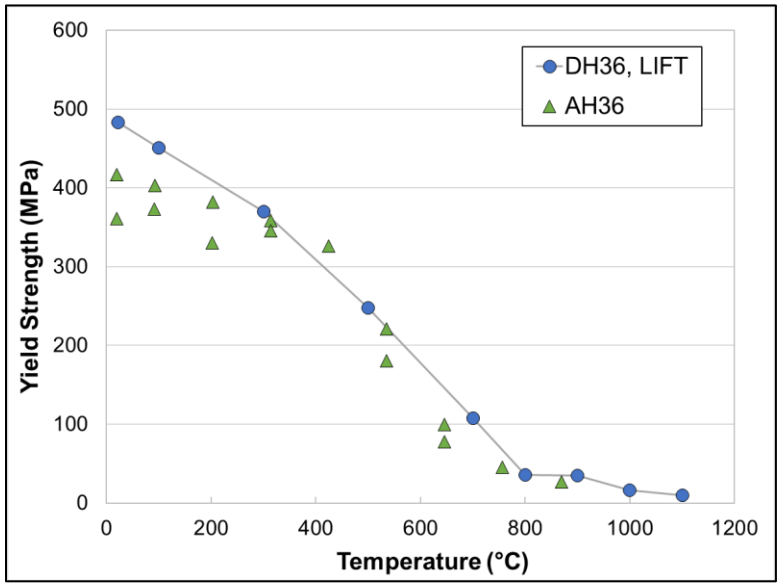


**Figure 28.** Measured elevated temperature 0.2% offset yield strength for DH36 steel, showing good correspondence with AH36 data adapted from reference [40].

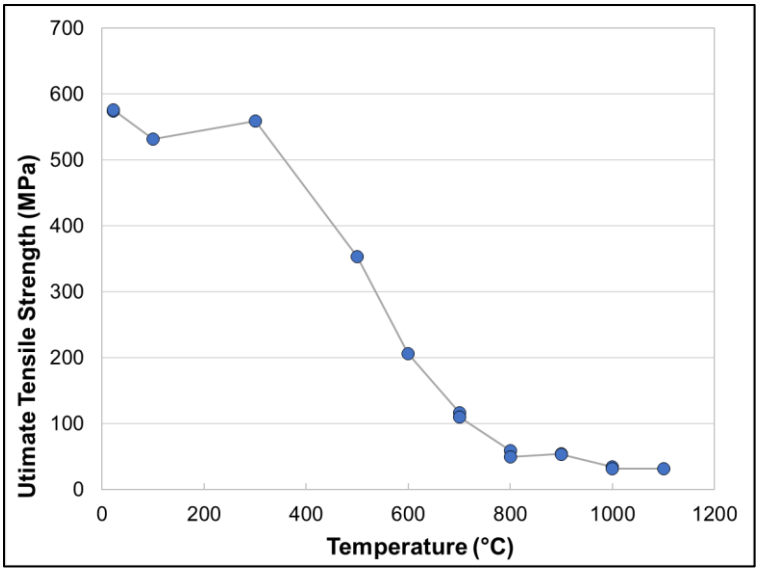


**Figure 29. Measured elevated temperature ultimate tensile strength for DH36 steel.**

**Figure 29** shows the measured yield strengths from specimens cycled to a peak temperature of 1350 °C (2462 °F). The stress-strain curves associated with the data are given in **Figures 75-77** of **Appendix F**. At room temperature, the 100 °C/s (180 °F/s) specimen was nearly 50% stronger than the 10 °C/s (18 °F/s) specimen, but the yield strength of 10 °C/s (18 °F/s) specimen was nearly identical to that of the 1 °C/s (1.8 °F/s) specimen. The yield strengths of the slower-cooled specimens were nominally the same as the base material. These observations are consistent with the change in transformation products from various ferrite and pearlite morphologies to bainite. At 200 °C (392 °F), the 1 and 100 °C/s (1.8 and 180 °F/s) specimens experienced virtually no change in yield strength from room temperature, but the 10 °C/s (18 °F/s) specimen saw a 10% increase. It is unclear why this occurred. The 10 °C/s (18 °F/s) specimen $F_P/WF_{SP}$ starting microstructure may have experienced some additional carbide precipitation during reheating to 200 °C (392 °F), but confirmation of that would require additional microstructural analysis. As expected, for the austenite on cooling, the yield strength was below 20 MPa (2.9 ksi).

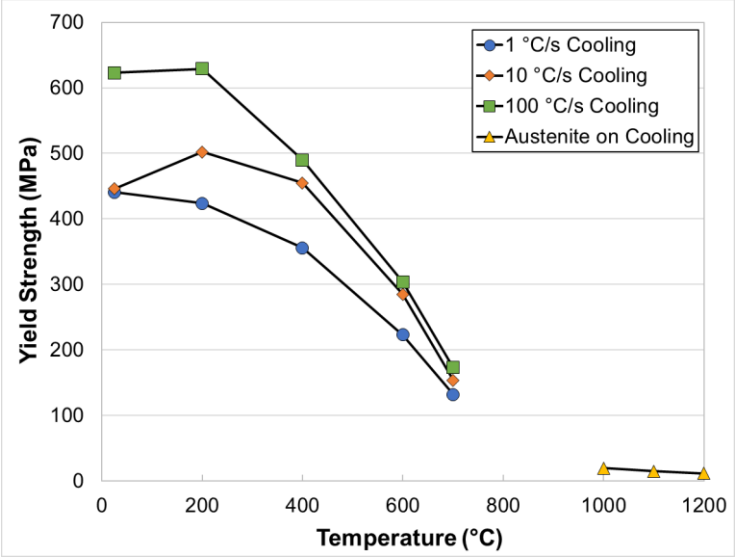


**Figure 30.** Yield strength of simulated DH36 CGHAZs after heating to 1350 °C (2462 °F) and cooling at different rates.

As indicated in **Figure 30**, there was in a monotonic decrease in yield strength with increasing temperature for all specimens above 200 °C (392 °F). The effect of a stronger starting microstructure was wiped out for the 100 °C/s (180 °F/s) specimens above 400 °C (752 °F) as their strength converged with those of the 10 °C/s (18 °F/s) samples. The yield strengths of all specimens then converged to that of the 1 °C/s (1.8 °F/s) specimen at 700 °C (1292 °F).

On-heating flow stress measurements for the DH36 base material are shown in **Figure 31** for all temperatures, and **Figure 32** highlights the flow behavior for tests at temperatures above 700 °C (1292 °F). The raw data points for these graphs can be found in **Appendix F**. The data are true stresses and strains calculated by applying the traditional conversion equations to engineering stress-strain data provided by the test lab. The data terminate at approximately 3.5 % strain, which corresponds to removal of the extensometers from the specimens by the test lab for protective reasons. In cases where the test temperature was 500 °C (932 °F) or below, this removal occurred well before UTS was reached. As a result, the flow stress behavior is not fully characterized for those samples. It is possible, however, to extrapolate the work hardening behavior to the onset of necking using the UTS values, which are also provided in **Appendix F**. As expected, increasing the test temperature tends to flatten the flow stress curves, since work hardening is made more difficult by dynamic recovery and/or recrystallization effects.

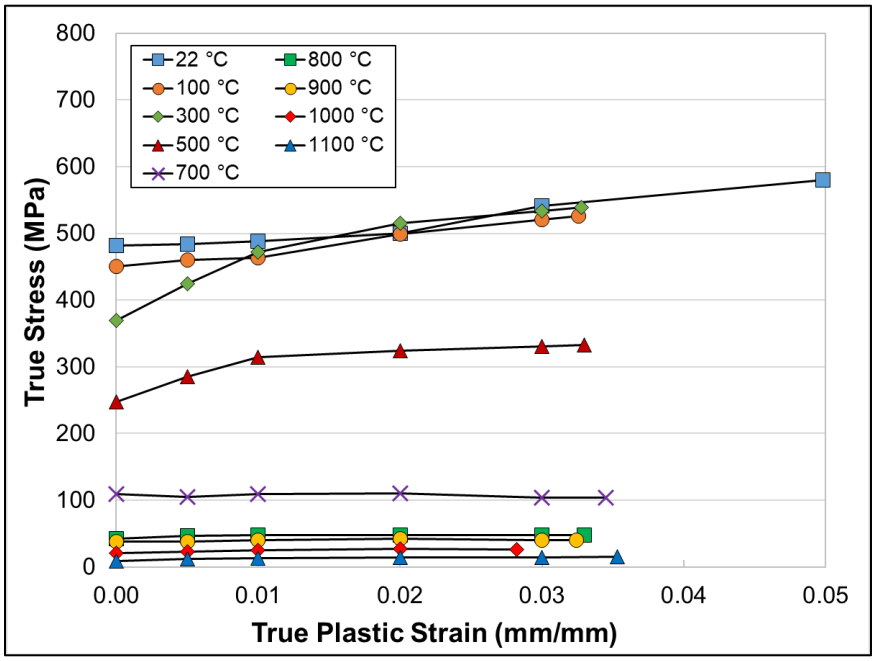


**Figure 31.** On-heating flow stress behavior for DH36 steel at various temperatures.

Flow stress curves for the thermally cycled DH36 are given in **Figures 33-36**. Since these tests were performed under inert atmosphere at OSU and NSWCCD, the extensometer was not removed during the tests, and more complete flow stress information is available. Once again, the data are true stresses and strains calculated by conversion from engineering stress-strain data. Such conversions are invalid past the onset of necking, so the terminal data points in **Figures 33-36** are at the UTS. All raw data points for these figures, along with the engineering fracture strains for the specimens, are found in **Appendix F**.

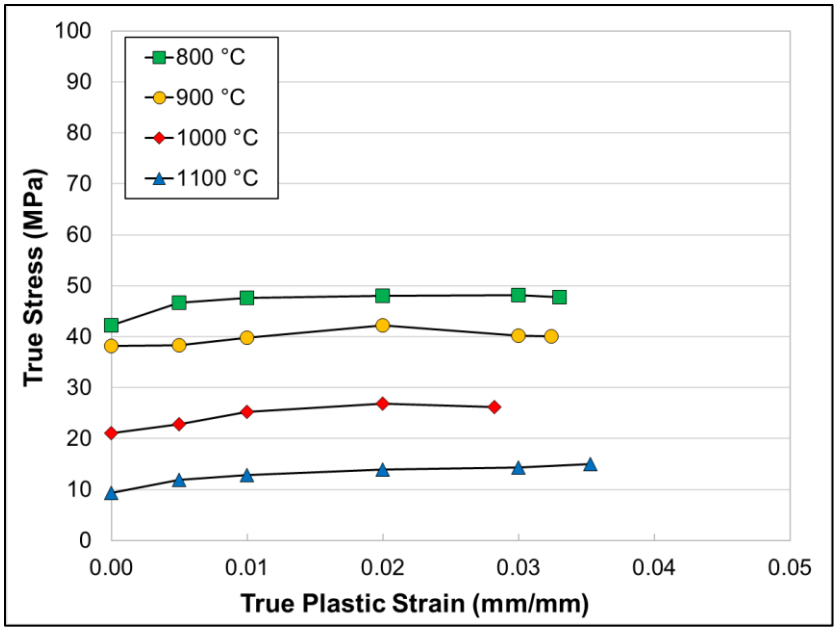


**Figure 32.** On-heating flow stress behavior for DH36 steel at testing temperatures above the austenitic phase transformation.

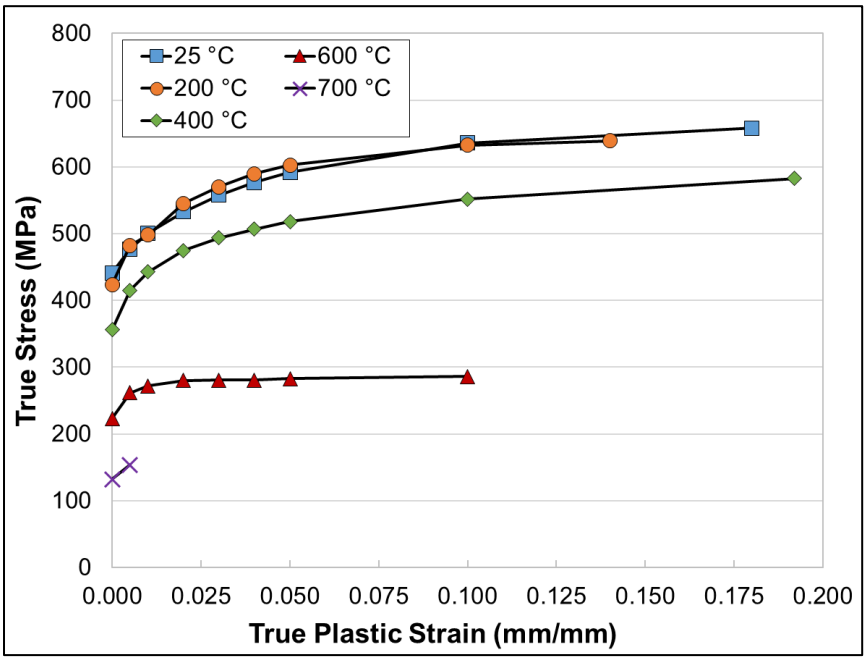


**Figure 33.** Flow stress behavior at various temperatures for DH36 steel after cooling at 1 °C/s (1.8 °F/s) from a peak temperature of 1350 °C (2462 °F). Terminal data points are at the UTS.

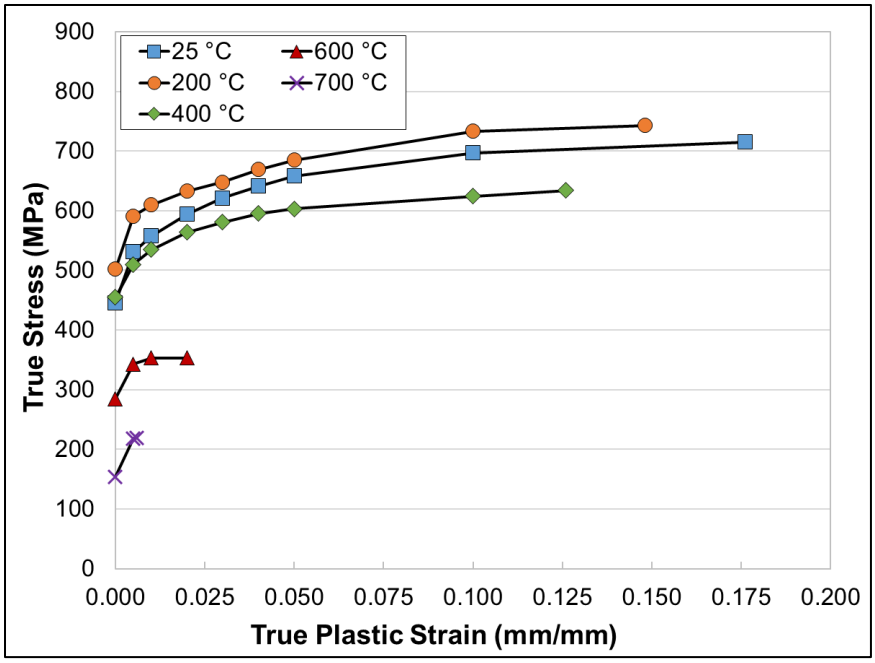


**Figure 34.** Flow stress behavior at various temperatures for DH36 steel after cooling at 10 °C/s (18 °F/s) from a peak temperature of 1350 °C (2462 °F). Terminal data points are at the UTS.

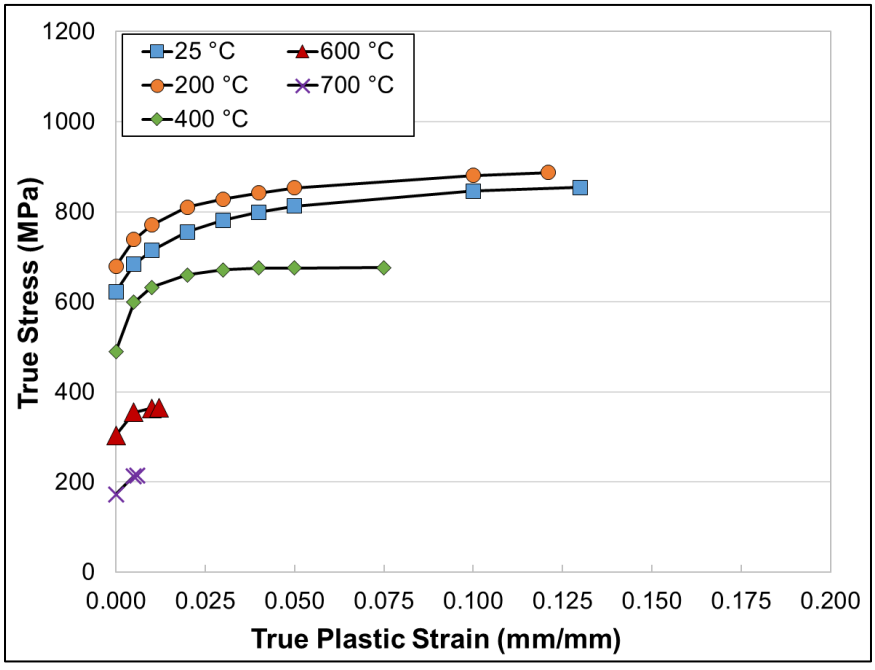


**Figure 35.** Flow stress behavior at various temperatures for DH36 steel after cooling at 100 °C/s (180 °F/s) from a peak temperature of 1350 °C (2462 °F). Terminal data points are at the UTS.

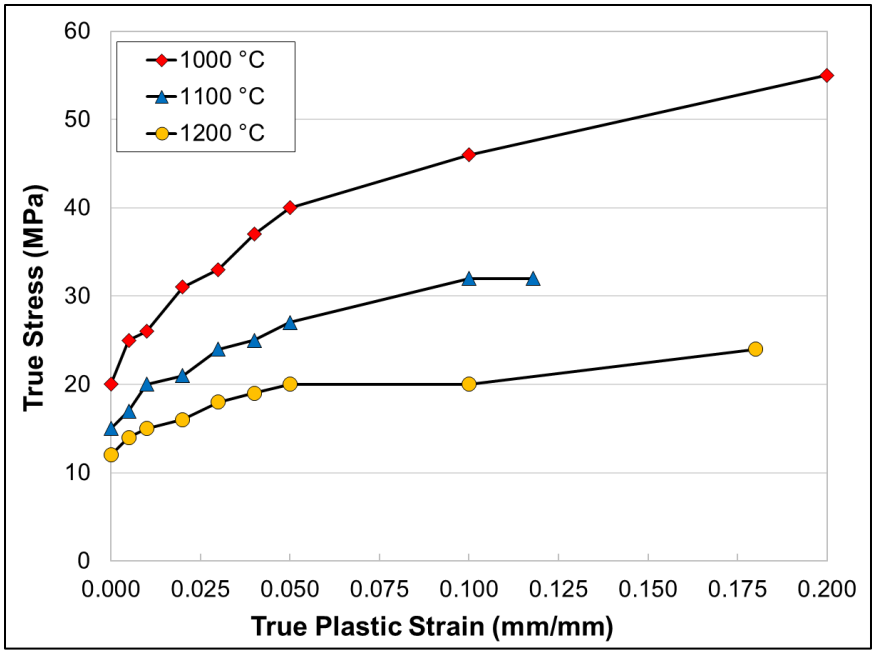


**Figure 36.** Flow stress behavior for austenitic DH36 steel after thermal cycling to 1350 °C (2462 °F). Terminal data points are at the UTS.

## SUMMARY

Temperature-dependent material property data of a pedigreed plate of DH36 steel from room temperature up to nearly the steel's melting point were determined. The thermo-physical properties investigated include specific heat, thermal diffusivity, thermal conductivity, coefficient of thermal expansion, and density. Thermo-mechanical properties including elastic modulus, yield strength, and flow stress were also measured. The temperatures associated with on-heating and on-cooling phase transformations and their variation with heating rate, cooling rate, and peak temperature were determined and used to develop welding-focused continuous cooling transformation (CCT) diagrams. Investigation of heat-affected zone microstructures from the CCT specimens and arc welds concluded the analysis. This effort is essential for increasing the fidelity of finite element models used to predict welding-induced distortion and residual stress in marine structures. The data generated in this program have been provided to ESI for immediate incorporation into their *SYSWELD* software. A machine-readable version of the collected data will be uploaded to the University of Michigan's *Materials Commons* data repository <https://materialscommons.org> at a later date.

# APPENDIX

## Appendix A: Plate Conformance Certificate for DH36 Steel

ArcelorMittal Burns Harbor Plate

QUALITY ASSURANCE
REPORT OF TEST AND ANAYLSES

| SHIPMENT NO. | DATE SHIPPED | CAR OR VEHICLE NO. | PAGE |
|---|---|---|---|
| 803-06510 | 05-20-16 | TRLR 806 | 1 |

SOLD TO:
HUNTINGTON INGALLS INDUSTRIES INC
INGALLS SHIPBUILDING DIV
PO BOX 149
PASCAGOULA MS 39568-0149

SHIP TO:
HUNTINGTON INGALLS INDUSTRIES INC
INGALLS SHIPBUILDING DIV
C/O METALS USA PLATES & SHAPES SE I
1 FOUNDRY RD
WAGGAMAN LA 70094-2349

| NOTE | SERIAL NUMBER | PAT NO. | HEAT NUMBER | NO. PCS. | SIZE AND QUANTITY: THICKNESS | WIDTH OR DIA. | LENGTH | WEIGHT | YIELD POINT | TENSILE STRENGTH | ELONG. | RED. |
|---|---|---|---|---|---|---|---|---|---|---|---|---|
| | | | | | INCHES | INCHES | INCHES | POUNDS | PSI | PSI | IN % | % |

QUALITY STEEL MELTED & MANUFACTURED IN THE U. S. A.
PLATES - MIL-S -22698C GR DH-36 MOD S.010
MAX NO WELD REPAIR KLD FINE GRAIN
PRAC AMEND 2 CLASS U CE=.38X PER
IIW FORMULA, CH-V A673 FREQ (P) T
17 FTLB AT -4F --- PLT CONTROL ROLL
NO WELD REPAIR WAS PERFORMED ON BELOW PLATE(S)
MFST - MFST MILL SERIAL# MFST MILL SERIAL# & PATTERN#
MFST PPI 0045045- 0001 LIFT MAX 30 TON UNLDG
OH-MAGNET
CO# 902619 GH 823-2341
OUTSIDE INSPECTION BY AMERICAN BUREAU OF SHIPPING

| | | | | | | | | | | |
|---|---|---|---|---|---|---|---|---|---|---|
| B058430 | 821S05650 | 2 | .1875 | 96 | 300 | 3062 | 77500 | 84100 | 2 | 40 |
| (M67)MFST CUST ITEM NO:001 | | | | | | | | | | |
| B058431 | 821S05650 | 2 | .1875 | 96 | 300 | 3062 | 77500 | 84100 | 2 | 40 |
| (M67)MFST CUST ITEM NO:001 | | | | | | | | | | |
| B058432 | 821S05650 | 1 | .1875 | 96 | 300 | 1531 | 77500 | 84100 | 2 | 40 |
| (M67)MFST CUST ITEM NO:001 | | | | | | | | | | |
| B058433 | 821S05650 | 2 | .1875 | 96 | 300 | 3062 | 77500 | 84100 | 2 | 40 |
| (M67)MFST CUST ITEM NO:001 | | | | | | | | | | |

Q-QUENCH TEMPERATURE T-TEMPER TEMPERATURE N-NORMALIZE TEMPERATURE

WE HEREBY CERTIFY THAT THE MATERIAL DESCRIBED HEREIN HAS BEEN MADE BY THE ARCELORMITTAL BH PLNT TO THE APPLICABLE SPECIFICATION BY AN APPROVED PROCESS AND HAS BEEN TESTED IN ACCORDANCE WITH THE REQUIREMENTS OF THE AMERICAN BUREAU OF SHIPPING RULES FOR THE INSPECTION AND TESTING OF MATERIALS TO THE SATISFACTION OF THE SURVEYORS.

| SERIAL NUMBER | PAT NO. | HEAT NUMBER | HARD BHN | BEND | THICKNESS INCHES | TYPE | SIZE | DIR | TEST TEMP F | CHARPY IMPACT ENERGY FT LBS 1 | 2 | 3 | SHEAR(%) 1 | 2 | 3 | LAT. EXP MILS 1 | 2 | 3 |
|---|---|---|---|---|---|---|---|---|---|---|---|---|---|---|---|---|---|---|
| B058430 | | 821S05650 | | | .187 | V | 1/3 | T | -4 | 35 | 35 | 37 | | | | | | |
| B058431 | | 821S05650 | | | .187 | V | 1/3 | T | -4 | 29 | 29 | 34 | | | | | | |
| B058432 | | 821S05650 | | | .187 | V | 1/3 | T | -4 | 36 | 36 | 38 | | | | | | |
| B058433 | | 821S05650 | | | .187 | V | 1/3 | T | -4 | 39 | 38 | 38 | | | | | | |

| HEAT NUMBER | CHEMICAL ANALYSIS C | Mn | P | S | Si | Cu | Ni | Cr | Mo | V | Ti | Al | B | Cb | N | Sn | MQUAID GRAIN SIZE |
|---|---|---|---|---|---|---|---|---|---|---|---|---|---|---|---|---|---|
| 821S05650 | .07 | 1.31 | .011 | .004 | .241 | .028 | .02 | .04 | .006 | .044 | .014 | .033 | .0002 | .028 | .009 | .007 | |
| | CE .31 | | | | | | | | | | | | | | | | |

I certify that the above results are a true and correct copy of actual results contained in records maintained by ArcelorMittal Burns Harbor and are in full compliance with the requirements of the specification cited above. This test report connot be altered and must be transmitted intact with any subsquent third party test reports, if required.

R. SPANGLER II PER LSS

BHPLTRPT.TIF SUPV. QUALITY ASSURANCE

## ArcelorMittal Burns Harbor Plate

QUALITY ASSURANCE
REPORT OF TEST AND ANAYLSES

| SHIPMENT NO. | DATE SHIPPED | CAR OR VEHICLE NO. | PAGE |
|---|---|---|---|
| 803-06510 | 05-20-16 | TRLR 806 | 2 |

SOLD TO
HUNTINGTON INGALLS INDUSTRIES INC
INGALLS SHIPBUILDING DIV
PO BOX 149
PASCAGOULA MS 39568-0149

SHIP TO
HUNTINGTON INGALLS INDUSTRIES INC
INGALLS SHIPBUILDING DIV
C/O METALS USA PLATES & SHAPES SE I
1 FOUNDRY RD
WAGGAMAN LA 70094-2349

| SERIAL NUMBER | PAT NO. | HEAT NUMBER | NO. PCS. | SIZE AND QUANTITY: THICKNESS | WIDTH OR DIA. | LENGTH | WEIGHT | YIELD POINT | TENSILE STRENGTH | ELONG. | RED. |
|---|---|---|---|---|---|---|---|---|---|---|---|
| | | | | INCHES | INCHES | INCHES | POUNDS | PSI | PSI | IN | % % |

QUALITY STEEL MELTED & MANUFACTURED IN THE U. S. A.
PLATES - MIL-S -22698C GR DH-36 MOD S.010
MAX NO WELD REPAIR KLD FINE GRAIN
PRAC AMEND 2 CLASS U CE=.38X PER
IIW FORMULA, CH-V A673 FREQ (P) T
17 FTLB AT -4F --- PLT CONTROL ROLL
NO WELD REPAIR WAS PERFORMED ON BELOW PLATE(S)
MFST - MFST MILL SERIAL# MFST MILL SERIAL# & PATTERN#
MFST PPI 0045045- 0001 LIFT MAX 30 TON UNLDG
OH-MAGNET
CO# 902619 GH 823-2341
OUTSIDE INSPECTION BY AMERICAN BUREAU OF SHIPPING

| | | | | | | | | | | | |
|---|---|---|---|---|---|---|---|---|---|---|---|
| B058434 | 821S05650 | 2 | .1875 | 96 | 300 | 3062 | 77500 | 84100 | 2 | 40 | |
| (M67)MFST CUST ITEM NO:001 | | | | | | | | | | | |
| B058435 | 821S05650 | 2 | .1875 | 96 | 300 | 3062 | 77500 | 84100 | 2 | 40 | |
| (M67)MFST CUST ITEM NO:001 | | | | | | | | | | | |

Q-QUENCH TEMPERATURE T-TEMPER TEMPERATURE N-NORMALIZE TEMPERATURE

WE HEREBY CERTIFY THAT THE MATERIAL DESCRIBED HEREIN HAS BEEN MADE BY THE ARCELORMITTAL BH PLNT TO THE APPLICABLE SPECIFICATION BY AN APPROVED PROCESS AND HAS BEEN TESTED IN ACCORDANCE WITH THE REQUIREMENTS OF THE AMERICAN BUREAU OF SHIPPING RULES FOR THE INSPECTION AND TESTING OF MATERIALS TO THE SATISFACTION OF THE SURVEYORS.

| SERIAL NUMBER | PAT NO. | HEAT NUMBER | HARD BHN | BEND | THICKNESS INCHES | TYPE | SIZE | DIR | TEST TEMP F | CHARPY IMPACT ENERGY FT LBS 1 | 2 | 3 | SHEAR(%) 1 | 2 | 3 | LAT. EXP MILS 1 | 2 | 3 |
|---|---|---|---|---|---|---|---|---|---|---|---|---|---|---|---|---|---|---|
| B058434 | | 821S05650 | | | .187 | V | 1/3 | T | -4 | 38 | 36 | 37 | | | | | | |
| B058435 | | 821S05650 | | | .187 | V | 1/3 | T | -4 | 35 | 34 | 37 | | | | | | |

| HEAT NUMBER | CHEMICAL ANALYSIS C | Mn | P | S | Si | Cu | Ni | Cr | Mo | V | Ti | Al | B | Cb | N | Sn | MQUAID GRAIN SIZE |
|---|---|---|---|---|---|---|---|---|---|---|---|---|---|---|---|---|---|
| 821S05650 | .07 | 1.31 | .011 | .004 | .241 | .028 | .02 | .04 | .006 | .044 | .014 | .033 | .0002 | .028 | .009 | .007 | |
| | CE | | | | | | | | | | | | | | | | |
| | .31 | | | | | | | | | | | | | | | | |

I certify that the above results are a true and correct copy of actual results contained in records maintained by ArcelorMittal Burns Harbor and are in full compliance with the requirements of the specification cited above. This test report connot be altered and must be transmitted intact with any subsquent third party test reports, If required.

R. SPANGLER II PER LSS

BHPLTRPT.TIF SUPV. QUALITY ASSURANCE

## Appendix B: Continuous Cooling Transformation Curves

**Table 8.** Austenite transformation temperatures illustrated in **Figure 9**.

| Heating Rate (°C/s) | $A_{c1}$ (°C) | $A_{c3}$ (°C) |
|---|---|---|
| **100** | 722 | 916 |
| **200** | 745 | 910 |
| **500** | 752 | 920 |
| **1000** | 759 | 909 |
| **2000** | 777 | 904 |

**Table 9.** Experimentally measured on-cooling transformation temperatures for DH36 dilatometry specimens cooled from 875 °C (1607 °F). Colors correspond to the transformation products discussed in **Figures 10-17**.

| Cooling Rate (°C/s) [°F/s] | 1 [1.8] | 5 [9] | 10 [18] | 25 [45] | 100 [180] | 200 [360] |
|---|---|---|---|---|---|---|
| Transformation Temperature (°C) [°F] | 788 [1450] | 757 [1395] | 763 [1405] | 757 [1395] | 680 [1256] | 683 [1264] |
| | 715 [1319] | 671 [1240] | 666 [1231] | 657 [1215] | 542 [1008] | 547 [1017] |
| | 674 [1245] | 657 [1215] | 643 [1189] | | | |

**Table 10.** Experimentally measured on-cooling transformation temperatures for DH36 dilatometry specimens cooled from 1000 °C (1832 °F). Colors correspond to the transformation products discussed in **Figures 10-17**.

| Cooling Rate (°C/s) [°F/s] | 1 [1.8] | 1 [1.8], Retest | 5 [9] | 10 [18] | 25 [45] | 100 [180] | 200 [360] |
|---|---|---|---|---|---|---|---|
| Transformation Temperature (°C) [°F] | 784 [1443] | 797 [1467] | 752 [1386] | 746 [1345] | 719 [1326] | 706 [1303] | 691 [1276] |
| | 685 [1265] | 732 [1350] | 666 [1231] | 661 [1221] | 585 [1085] | 552 [1026] | 533 [991] |
| | 673 [1243] | 687 [1269] | 659 [1218] | 649 [1200] | | 540 [1004] | 529 [984] |

**Table 11.** Experimentally measured on-cooling transformation temperatures for DH36 dilatometry specimens cooled from 1150 °C (2102°F). Colors correspond to the transformation products discussed in **Figures 10-17**.

| Cooling Rate (°C/s) [°F/s] | 1 [1.8] | 5 [9] | 10 [18] | 25 [45] | 100 [180] | 200 [360] |
|---|---|---|---|---|---|---|
| Transformation Temperature (°C) [°F] | 755 [1391] | 701 [1294] | 697 [1287] | 685 [1265] | 591 [1096] | 564 [1047] |
| | 633 [1171] | 575 [1067] | 546 [1015] | 513 [955] | 412 [774] | 418 [784] |
| | 597 [1107] | 546 [1015] | | | | |

**Table 12.** Experimentally measured on-cooling transformation temperatures for DH36 dilatometry specimens cooled from 1350 °C (2462°F). Colors correspond to the transformation products discussed in **Figures 10-17**.

| Cooling Rate (°C/s) [°F/s] | 1 [1.8] | 5 [9] | 10 [18] | 25 [45] | 100 [180] | 200 [360] |
|---|---|---|---|---|---|---|
| Transformation Temperature (°C) [°F] | 771 [1420] | 682 [1260] | 663 [1225] | 630 [1166] | 556 [1033] | 536 [997] |
| | 586 [1087] | 565 [1049] | 548 [1018] | 495 [923] | 404 [759] | 402 [756] |
| | 572 [1062] | | | | | |

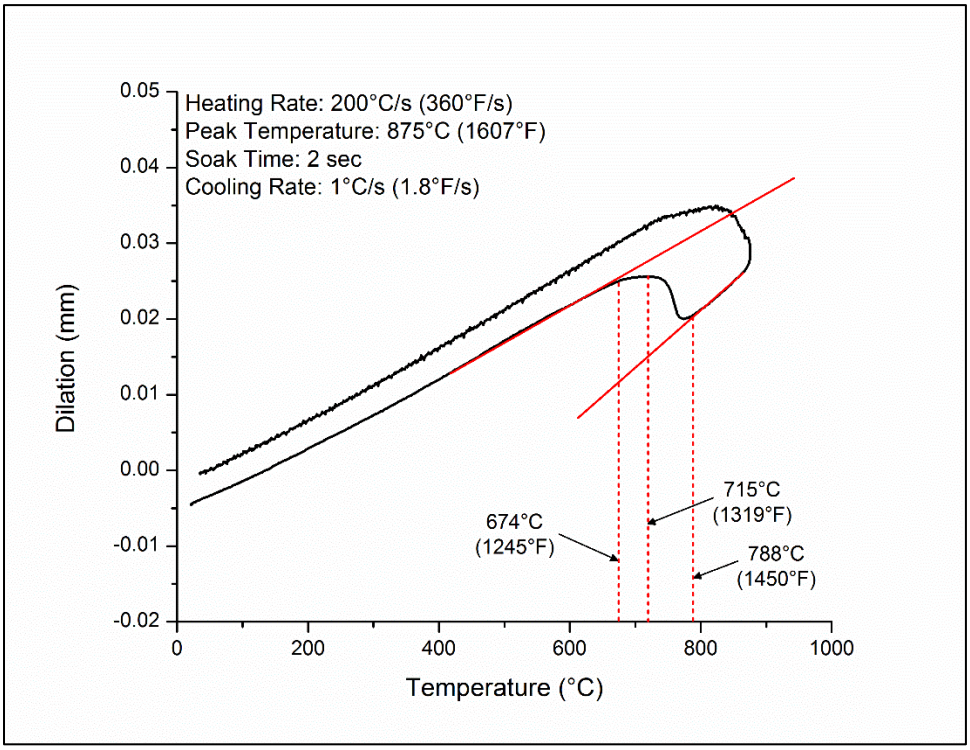


**Figure 37.** Dilation curve from a DH36 Gleeble sample heated to a peak temperature of 875 °C and cooled at 1 °C/s.

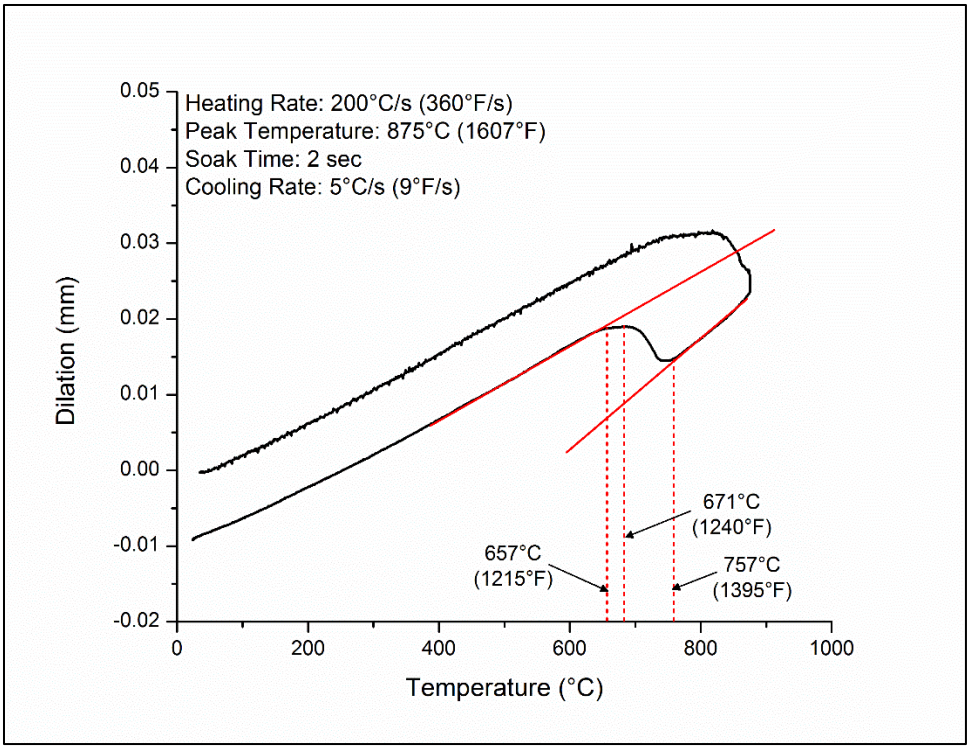


**Figure 38.** Dilation curve from a DH36 Gleeble sample heated to a peak temperature of 875 °C and cooled at 5 °C/s.

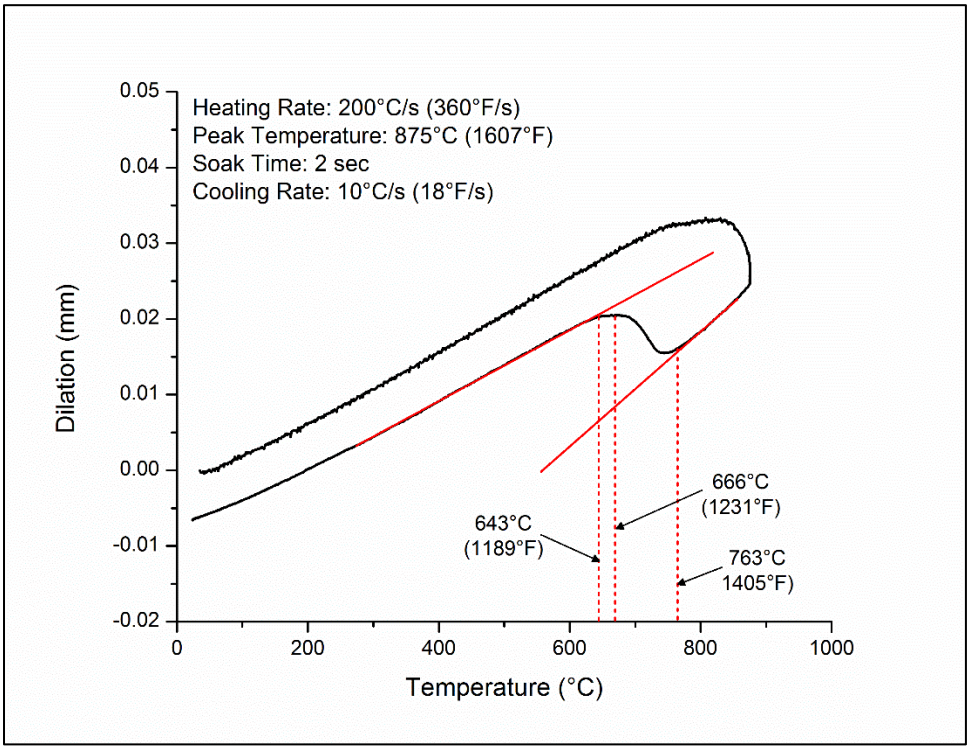


**Figure 39.** Dilation curve from a DH36 Gleeble sample heated to a peak temperature of 875 °C and cooled at 10 °C/s.

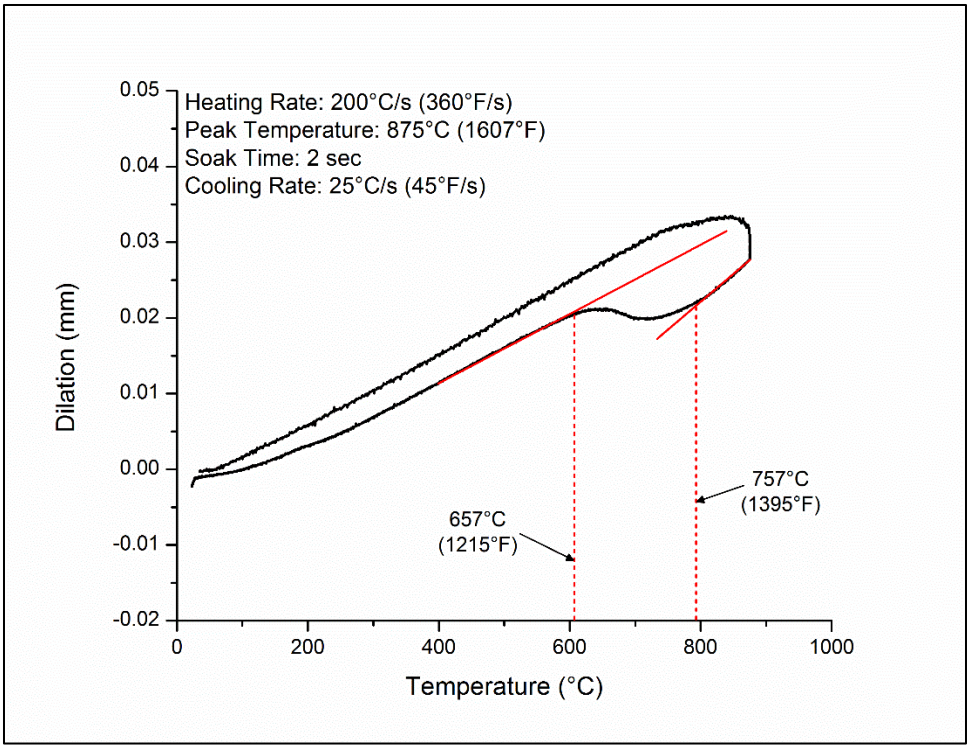


**Figure 40.** Dilation curve from a DH36 Gleeble sample heated to a peak temperature of 875 °C and cooled at 25 °C/s.

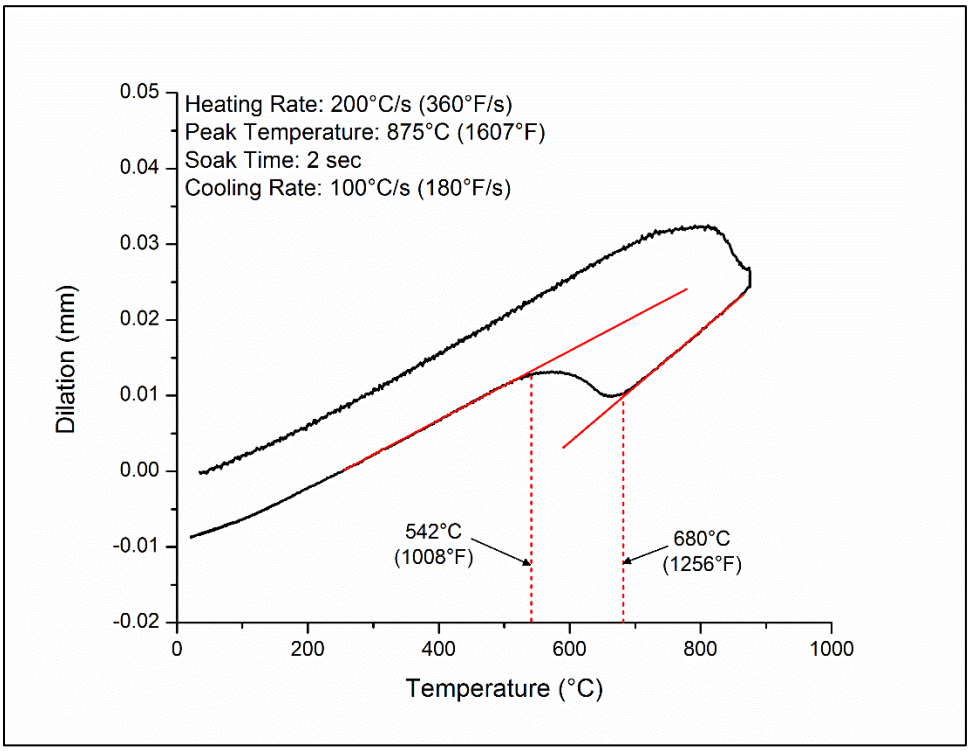


**Figure 41.** Dilation curve from a DH36 Gleeble sample heated to a peak temperature of 875 °C and cooled at 100 °C/s.

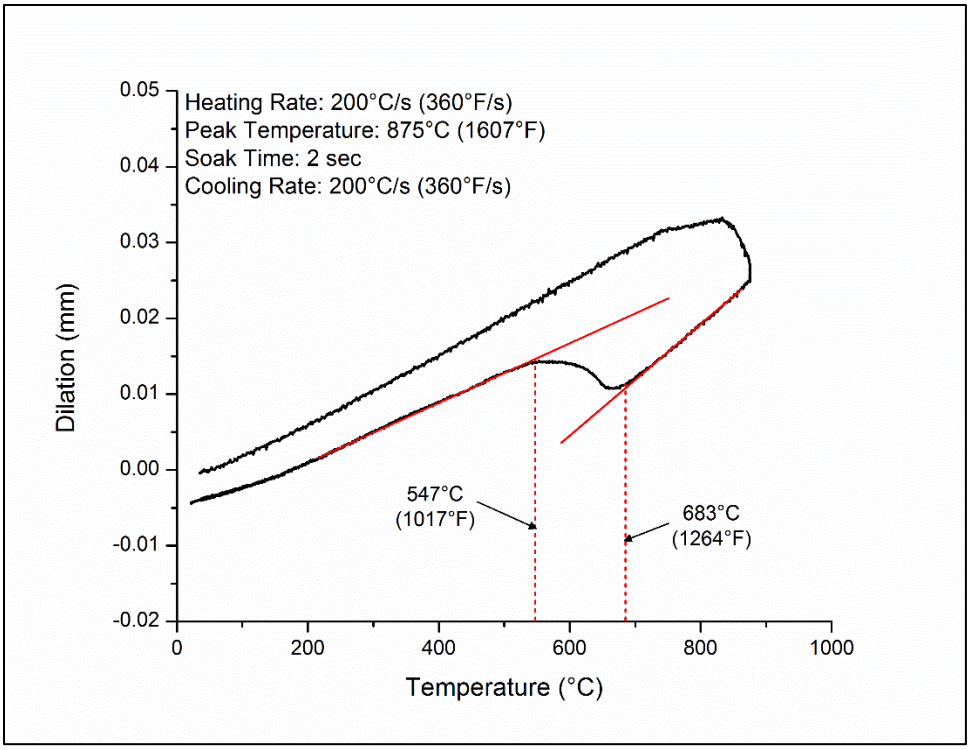


**Figure 42.** Dilation curve from a DH36 Gleeble sample heated to a peak temperature of 875 °C and cooled at 200 °C/s.

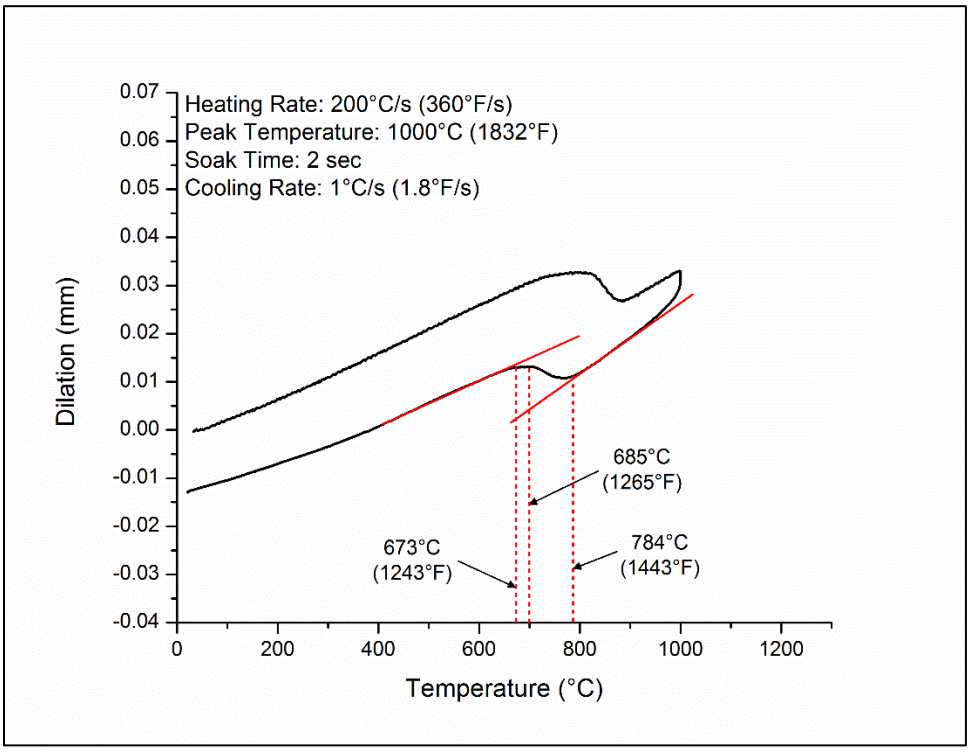


**Figure 43.** Dilation curve from a DH36 Gleeble sample heated to a peak temperature of 1000 °C and cooled at 1 °C/s.

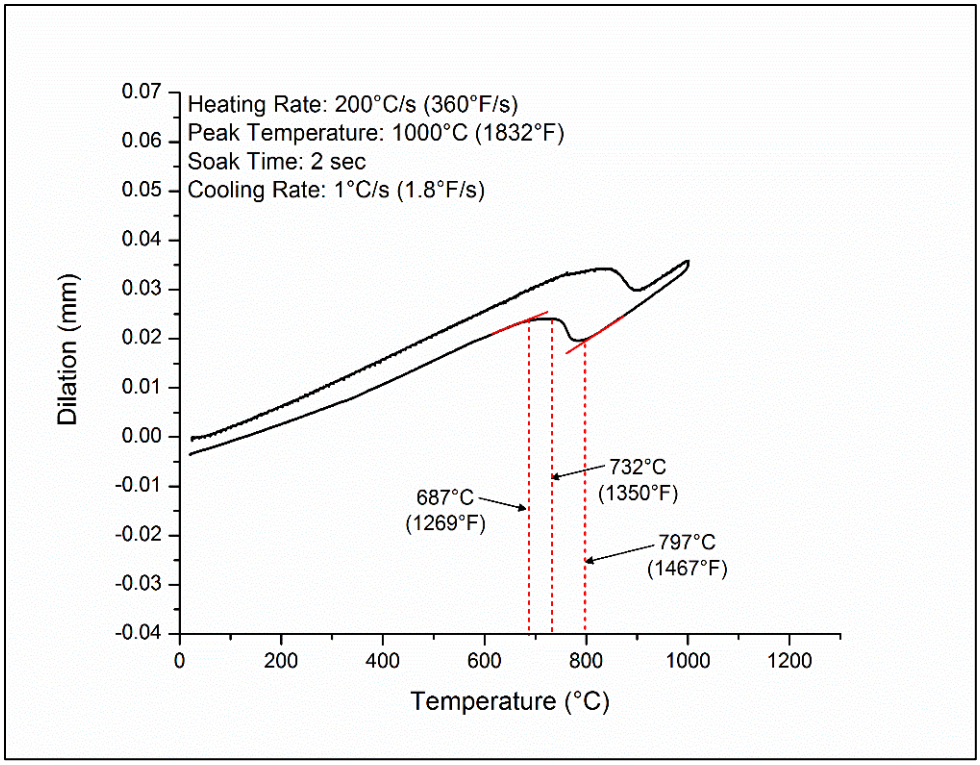


**Figure 44.** Dilation curve from duplicate DH36 Gleeble sample heated to a peak temperature of 1000 °C and cooled at 1 °C/s.

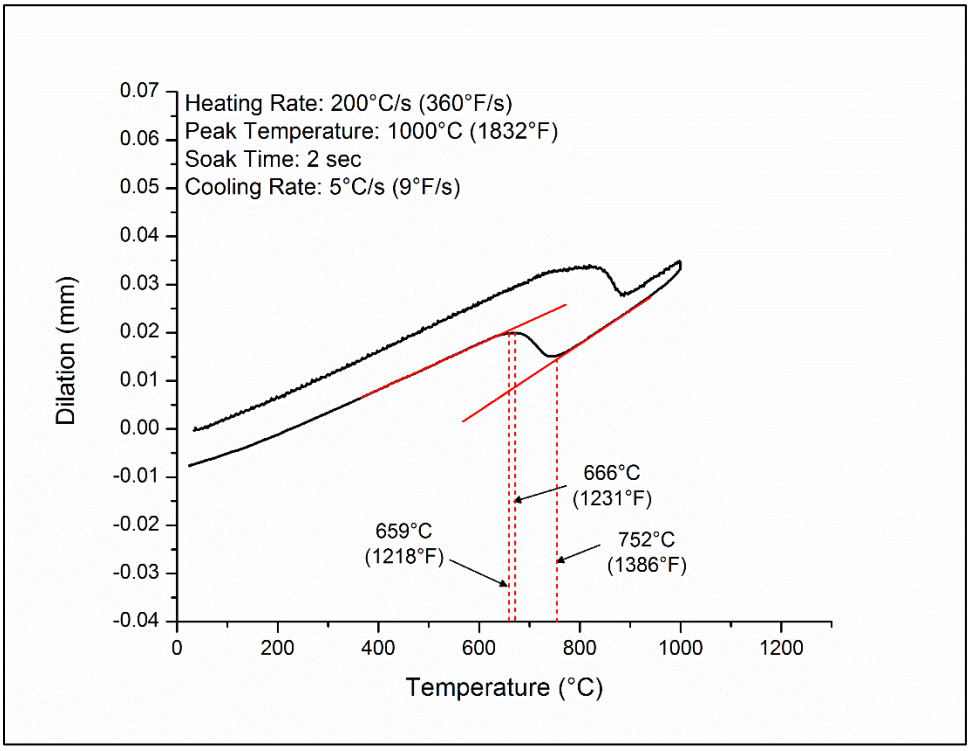


**Figure 45.** Dilation curve from a DH36 Gleeble sample heated to a peak temperature of 1000 °C and cooled at 5 °C/s.

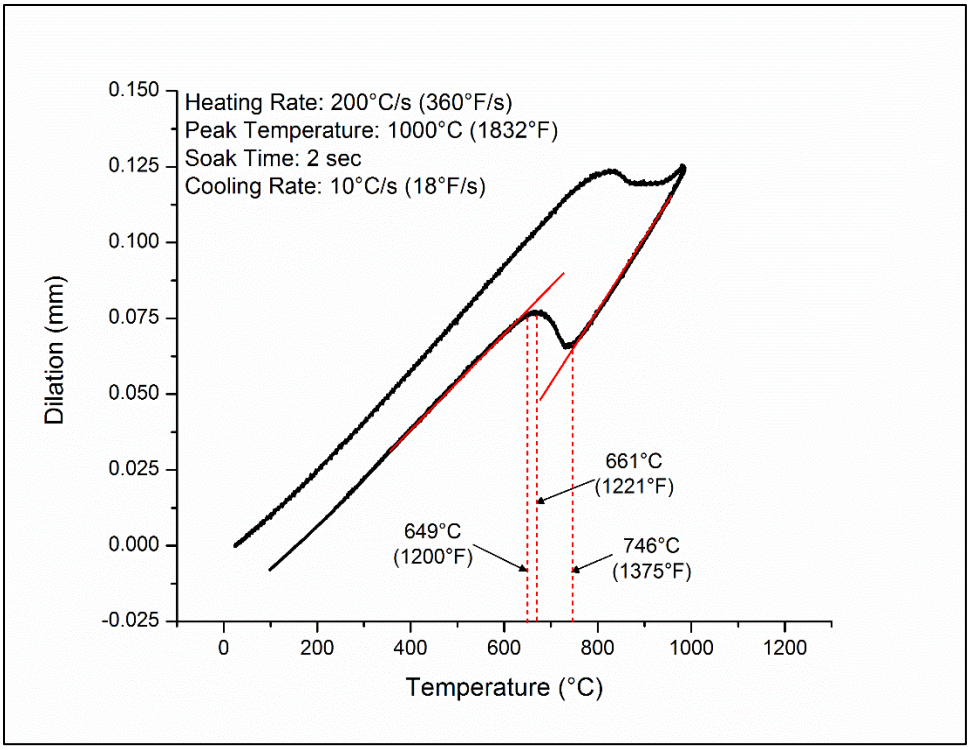


**Figure 46.** Dilation curve from a DH36 Gleeble sample heated to a peak temperature of 1000 °C and cooled at 10 °C/s.

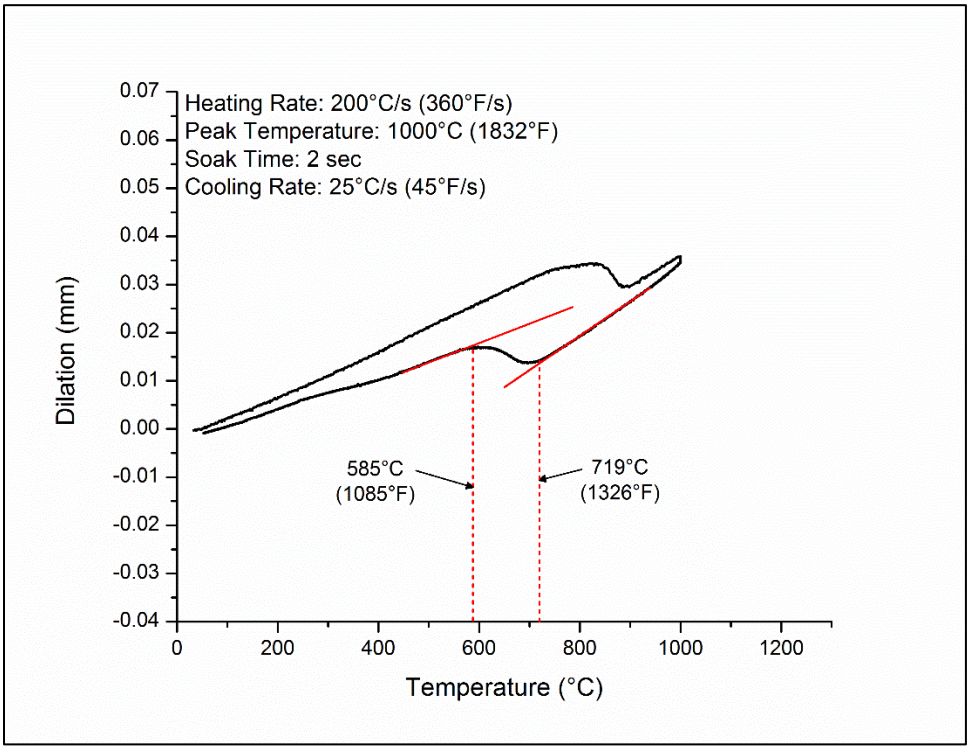


**Figure 47.** Dilation curve from a DH36 Gleeble sample heated to a peak temperature of 1000 °C and cooled at 25 °C/s.

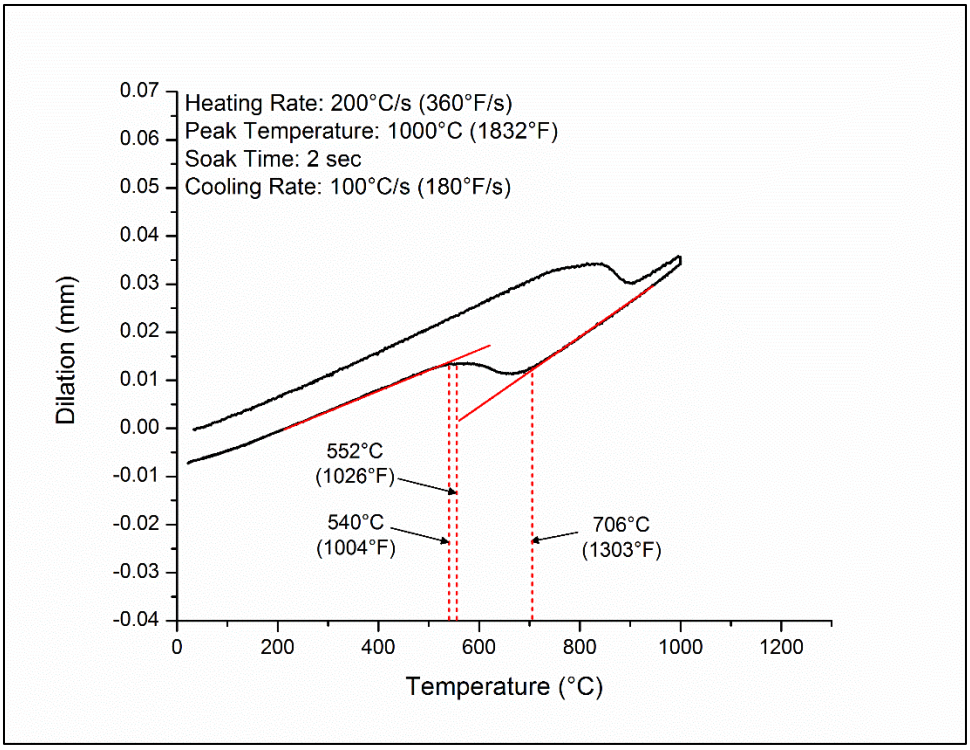


**Figure 48.** Dilation curve from a DH36 Gleeble sample heated to a peak temperature of 1000 °C and cooled at 100 °C/s.

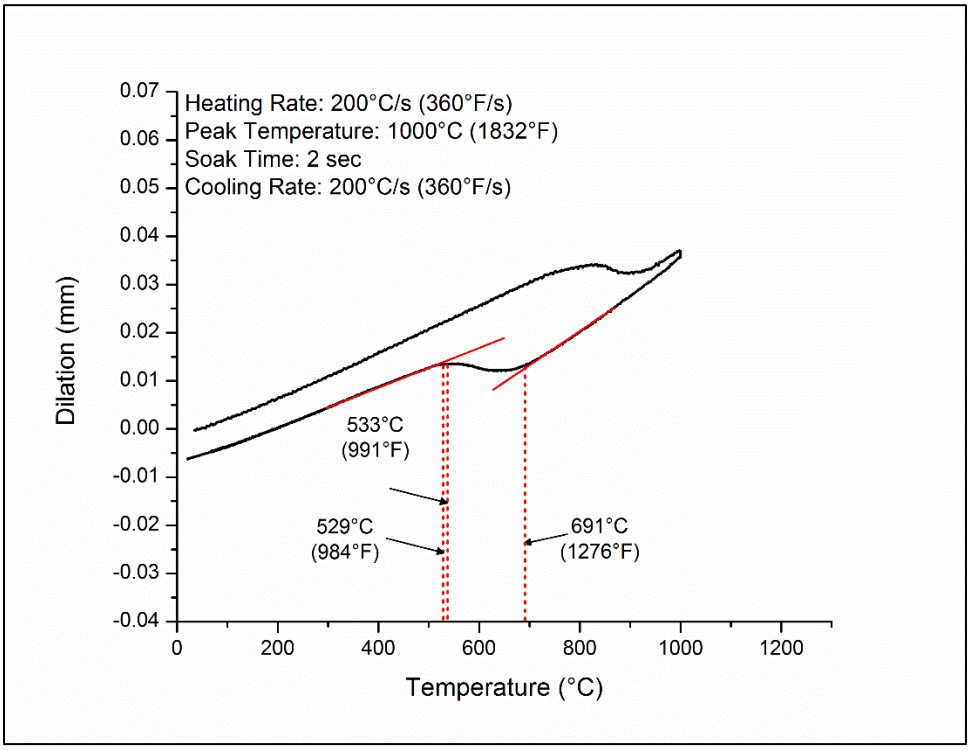


**Figure 49.** Dilation curve from a DH36 Gleeble sample heated to a peak temperature of 1000 °C and cooled at 200 °C/s.

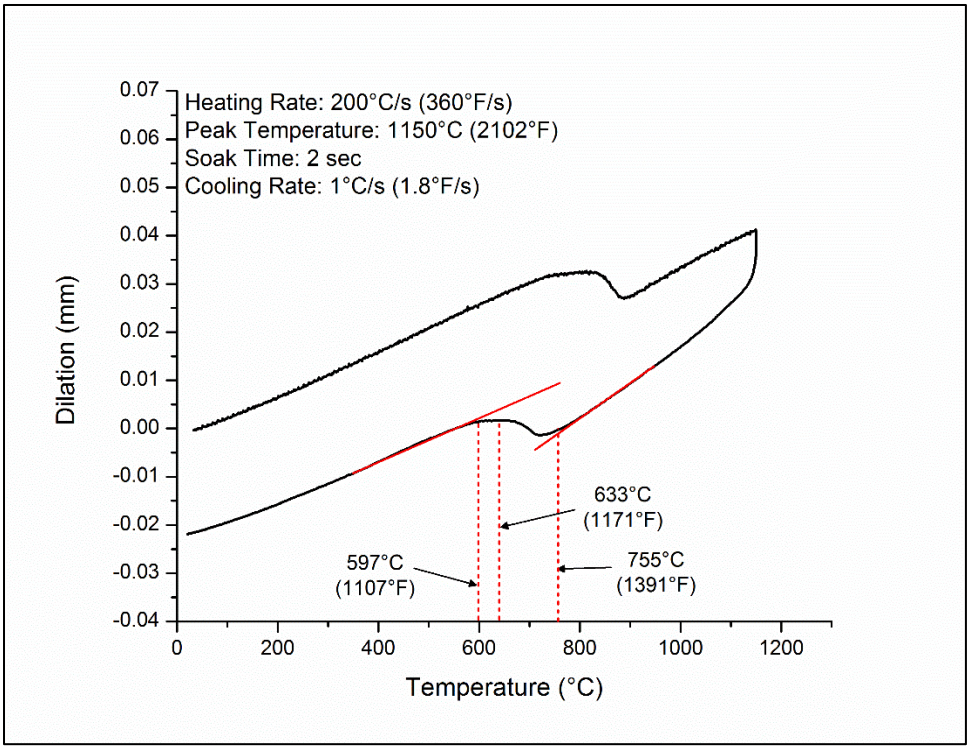


**Figure 50.** Dilation curve from a DH36 Gleeble sample heated to a peak temperature of 1150 °C and cooled at 1 °C/s.

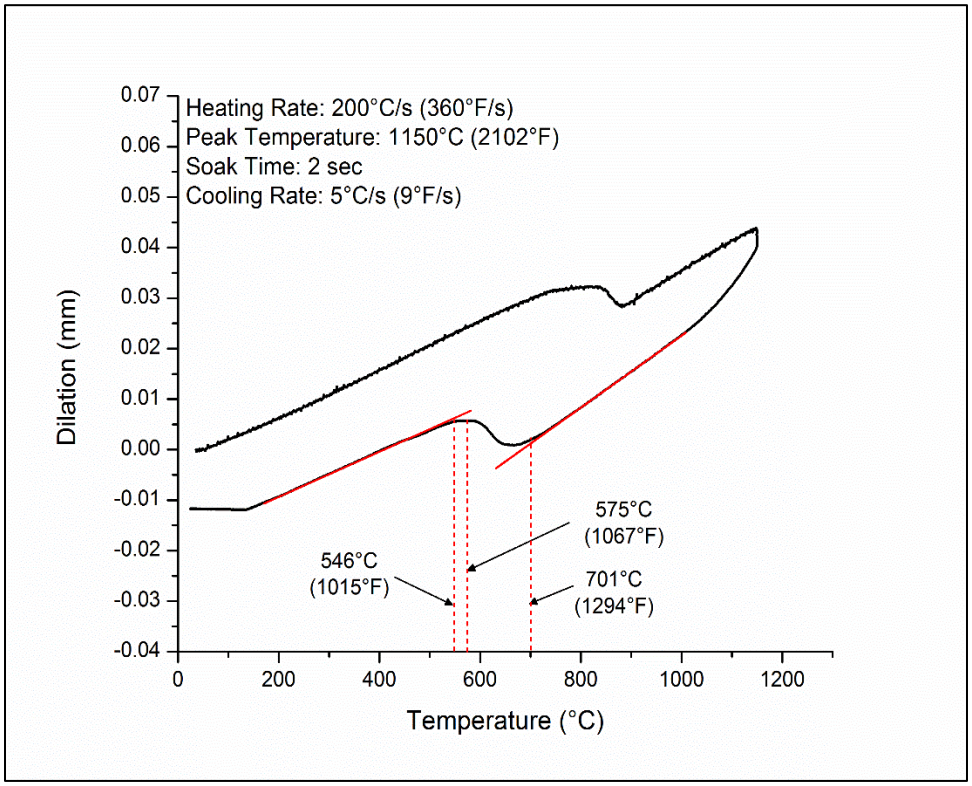


**Figure 51.** Dilation curve from a DH36 Gleeble sample heated to a peak temperature of 1150 °C and cooled at 5 °C/s.

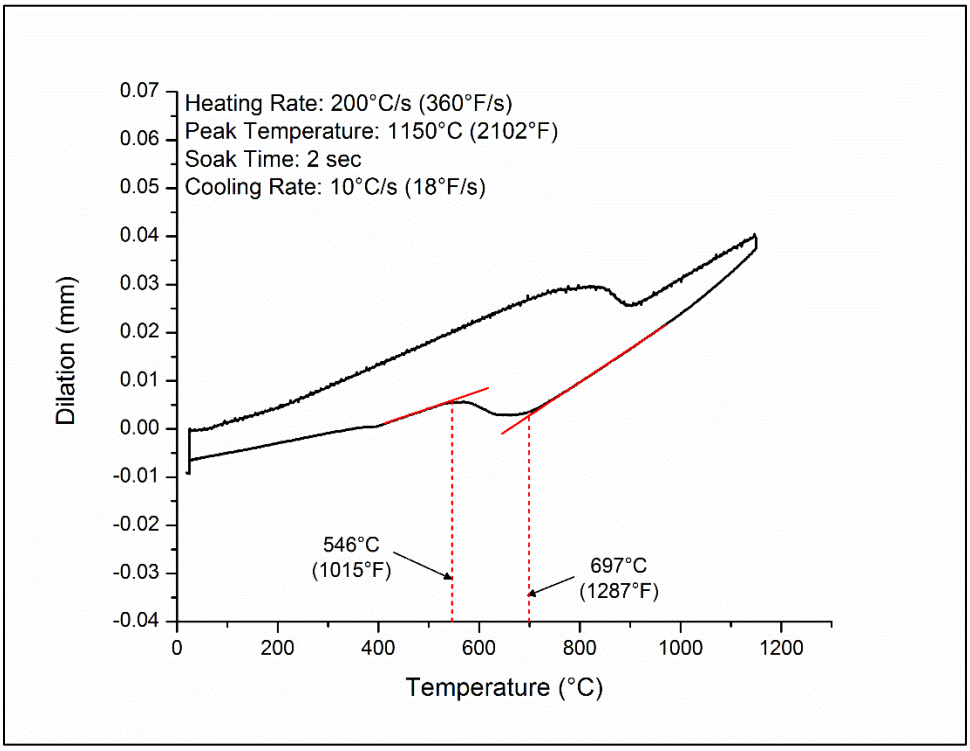


**Figure 52.** Dilation curve from a DH36 Gleeble sample heated to a peak temperature of 1150 °C and cooled at 10 °C/s.

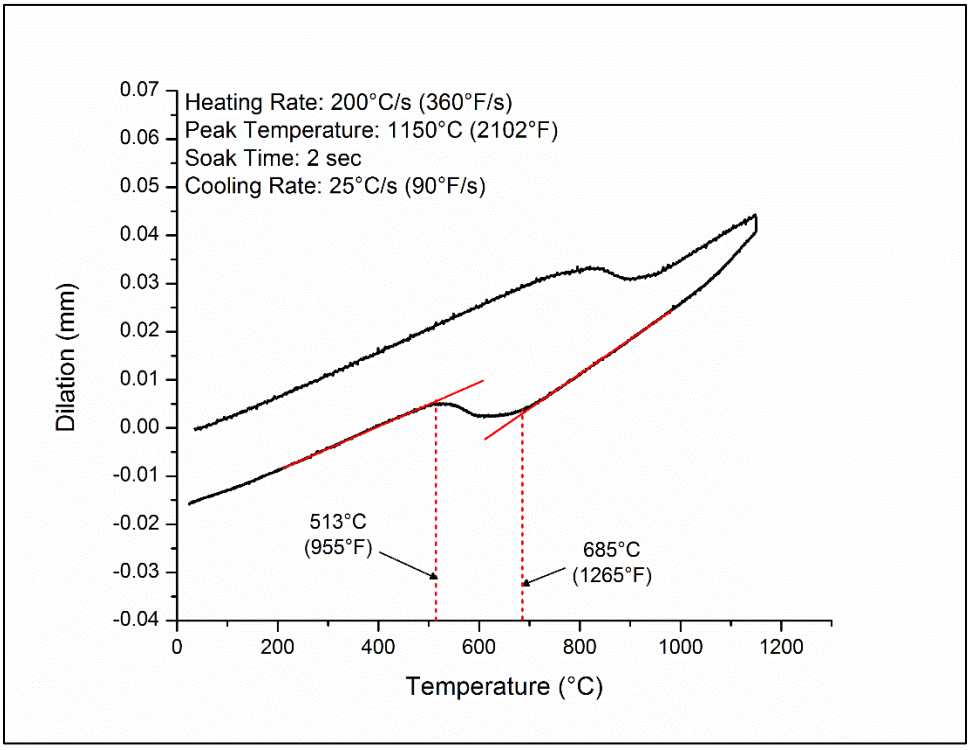


**Figure 53.** Dilation curve from a DH36 Gleeble sample heated to a peak temperature of 1150 °C and cooled at 25 °C/s.

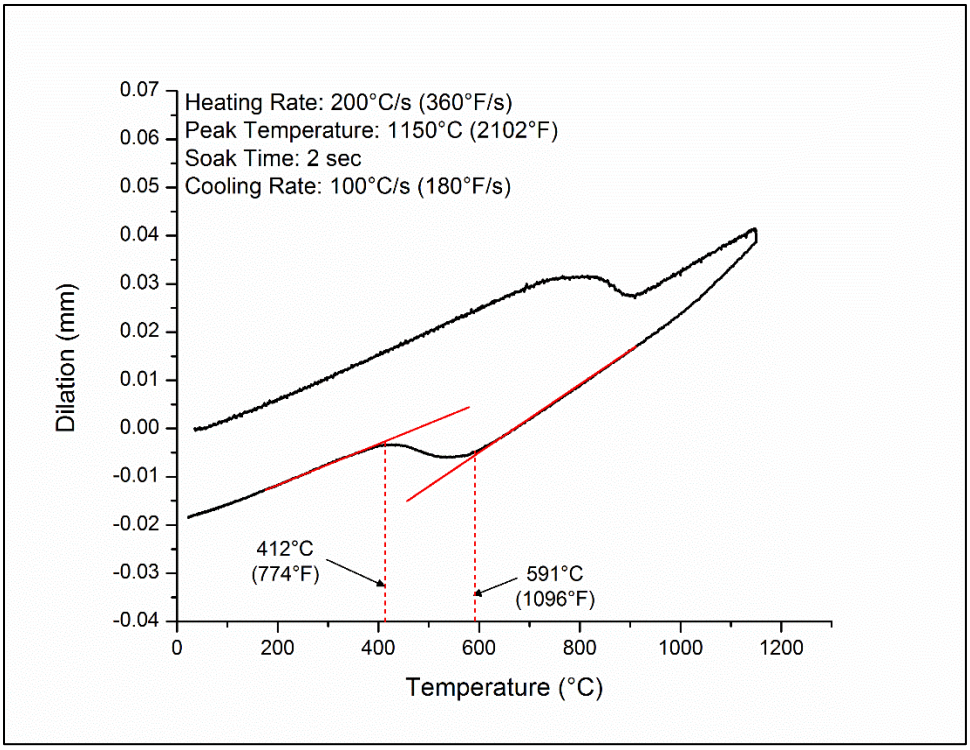


**Figure 54.** Dilation curve from a DH36 Gleeble sample heated to a peak temperature of 1150 °C and cooled at 100 °C/s.

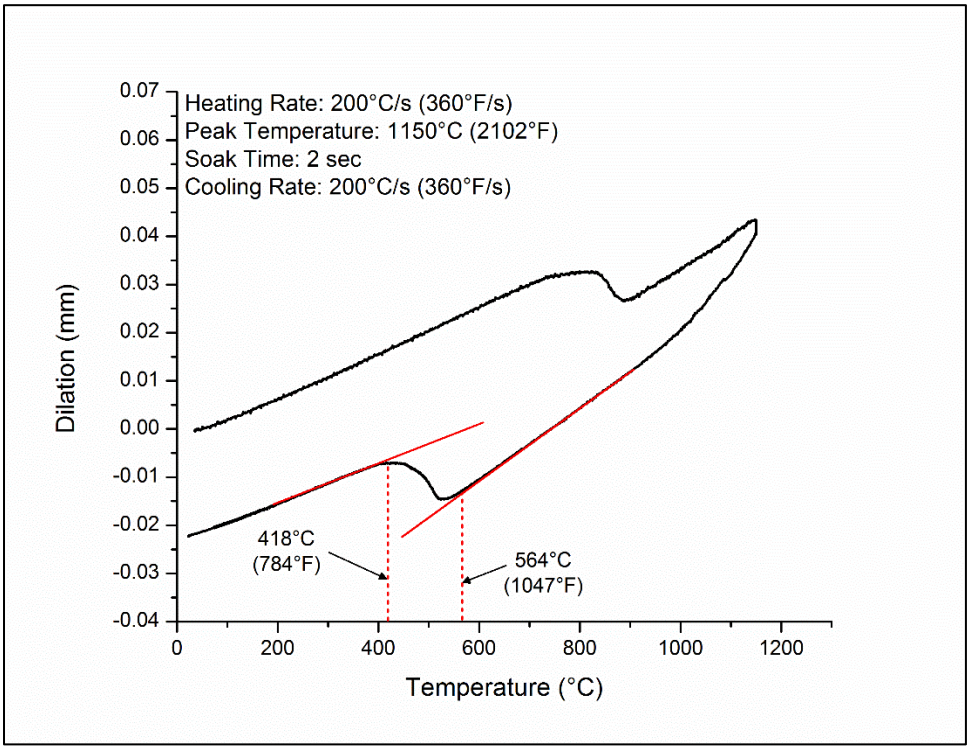


**Figure 55.** Dilation curve from a DH36 Gleeble sample heated to a peak temperature of 1150 °C and cooled at 200 °C/s.

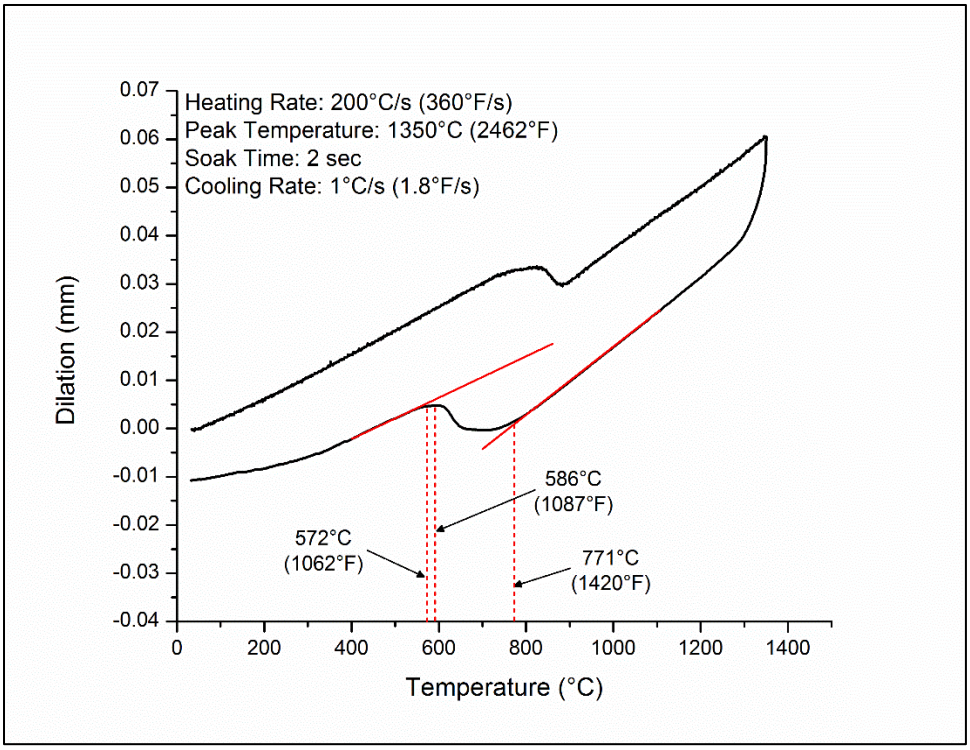


**Figure 56.** Dilation curve from a DH36 Gleeble sample heated to a peak temperature of 1350 °C and cooled at 1 °C/s.

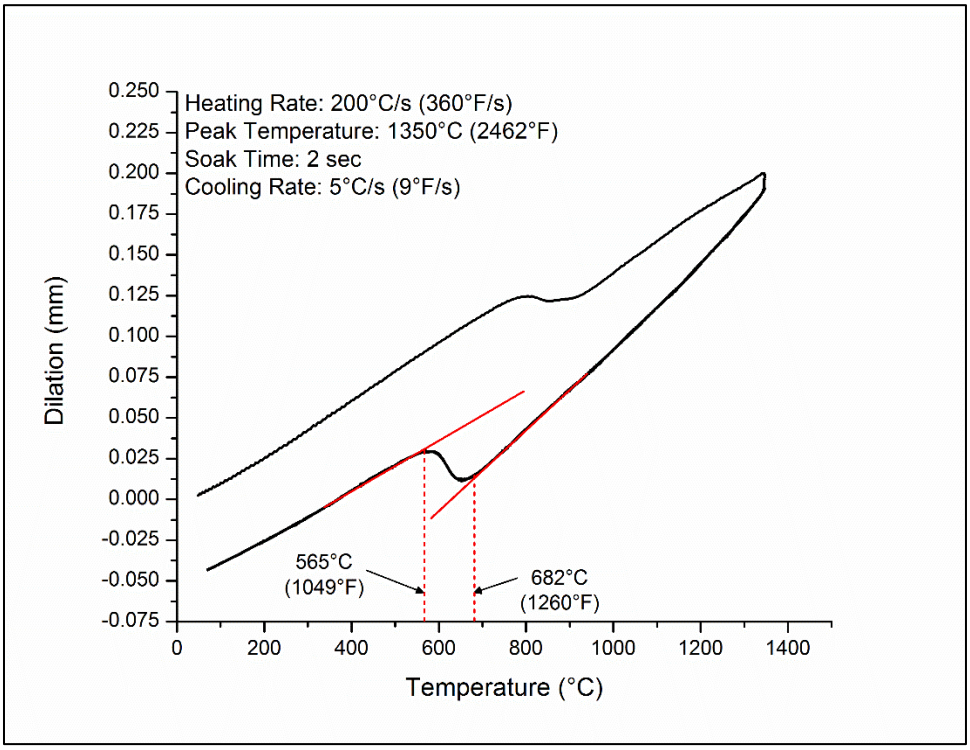


**Figure 57.** Dilation curve from a DH36 Gleeble sample heated to a peak temperature of 1350 °C and cooled at 5 °C/s.

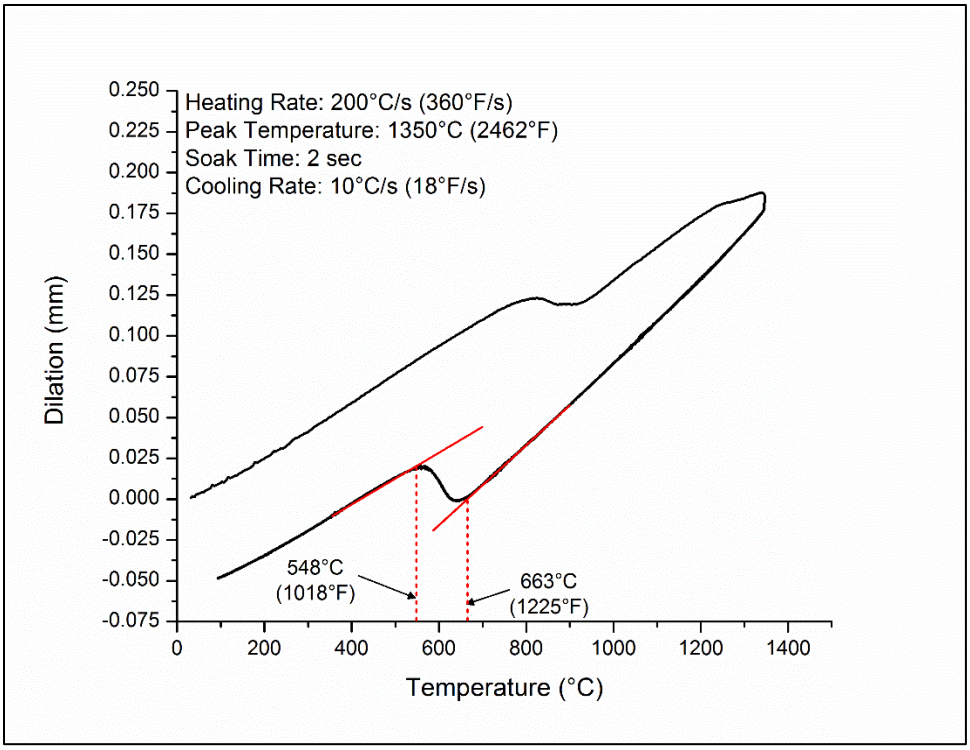


**Figure 58.** Dilation curve from a DH36 Gleeble sample heated to a peak temperature of 1350 °C and cooled at 10 °C/s.

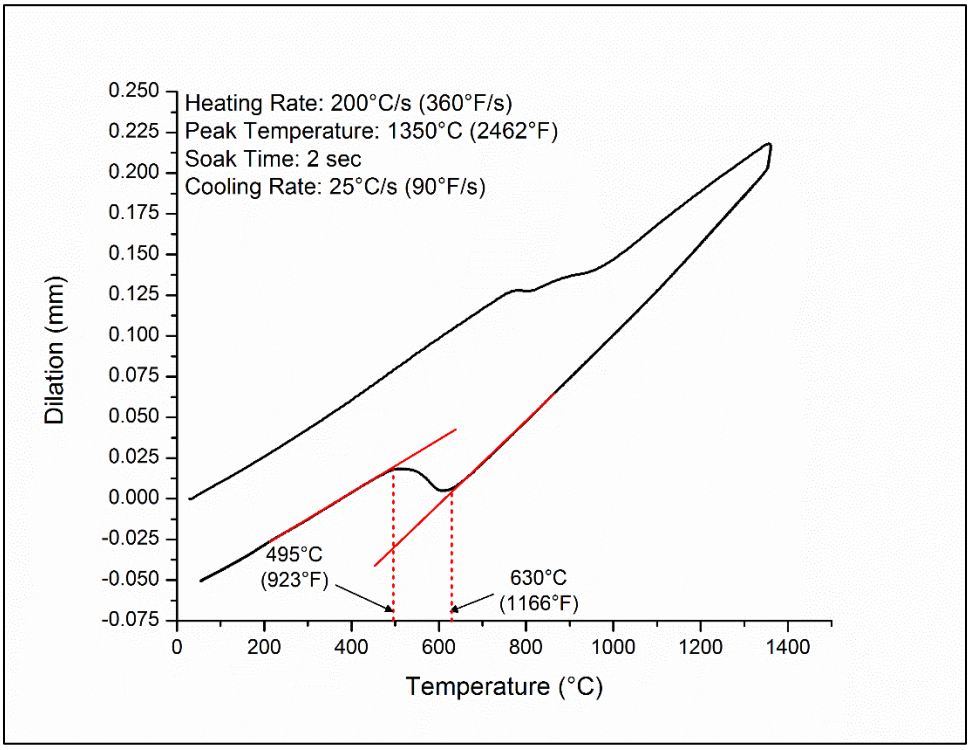


**Figure 59.** Dilation curve from a DH36 Gleeble sample heated to a peak temperature of 1350 °C and cooled at 25 °C/s.

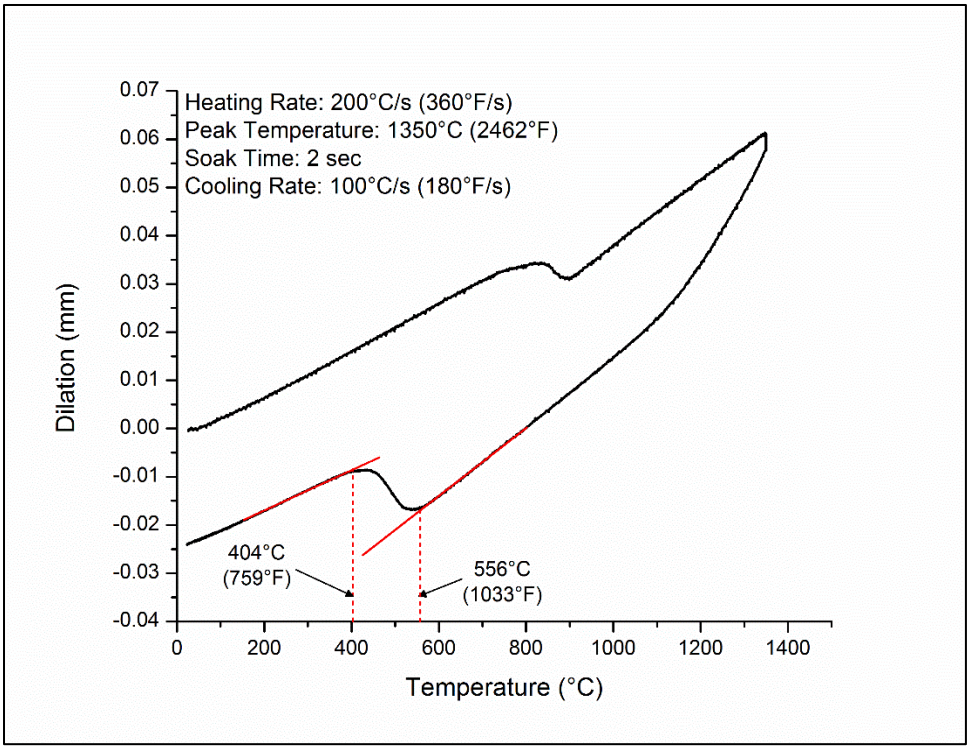


**Figure 60.** Dilation curve from a DH36 Gleeble sample heated to a peak temperature of 1350 °C and cooled at 100 °C/s.

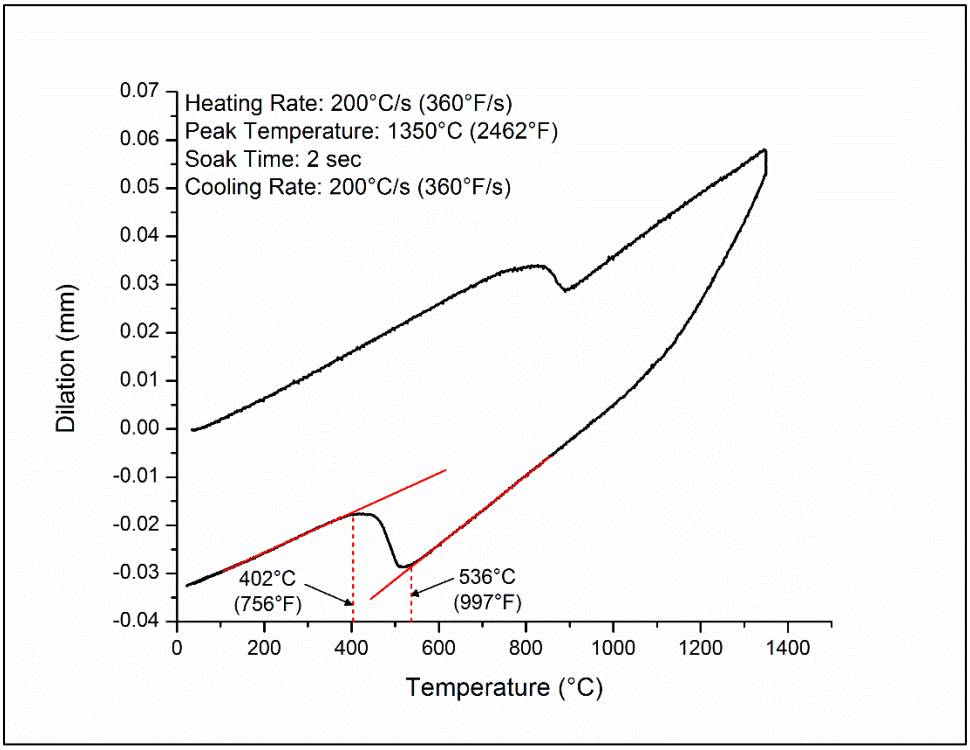


**Figure 61.** Dilation curve from a DH36 Gleeble sample heated to a peak temperature of 1350 °C and cooled at 200 °C/s.

## Appendix C: Representative Microstructures of DH36 CCT Specimens

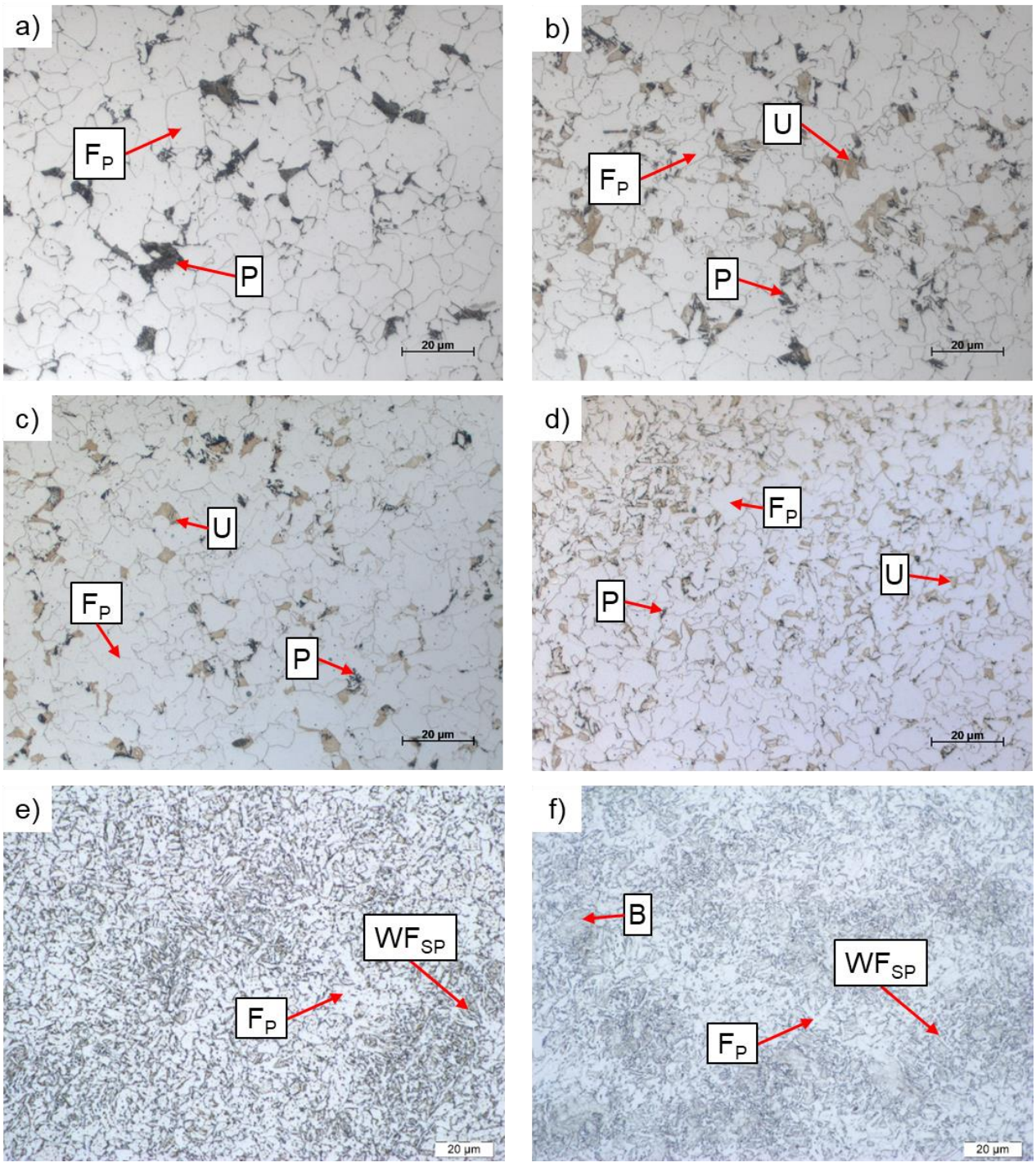


**Figure 62.** Representative microstructures from DH36 dilatometry specimens heated to a peak temperature of 875 °C (1607 °F) and continuously cooled at various rates. **(a-f)**: 1, 5, 10, 25, 100, and 200 °C/s (1.8, 9, 18, 45, 180, and 360 °F/s).

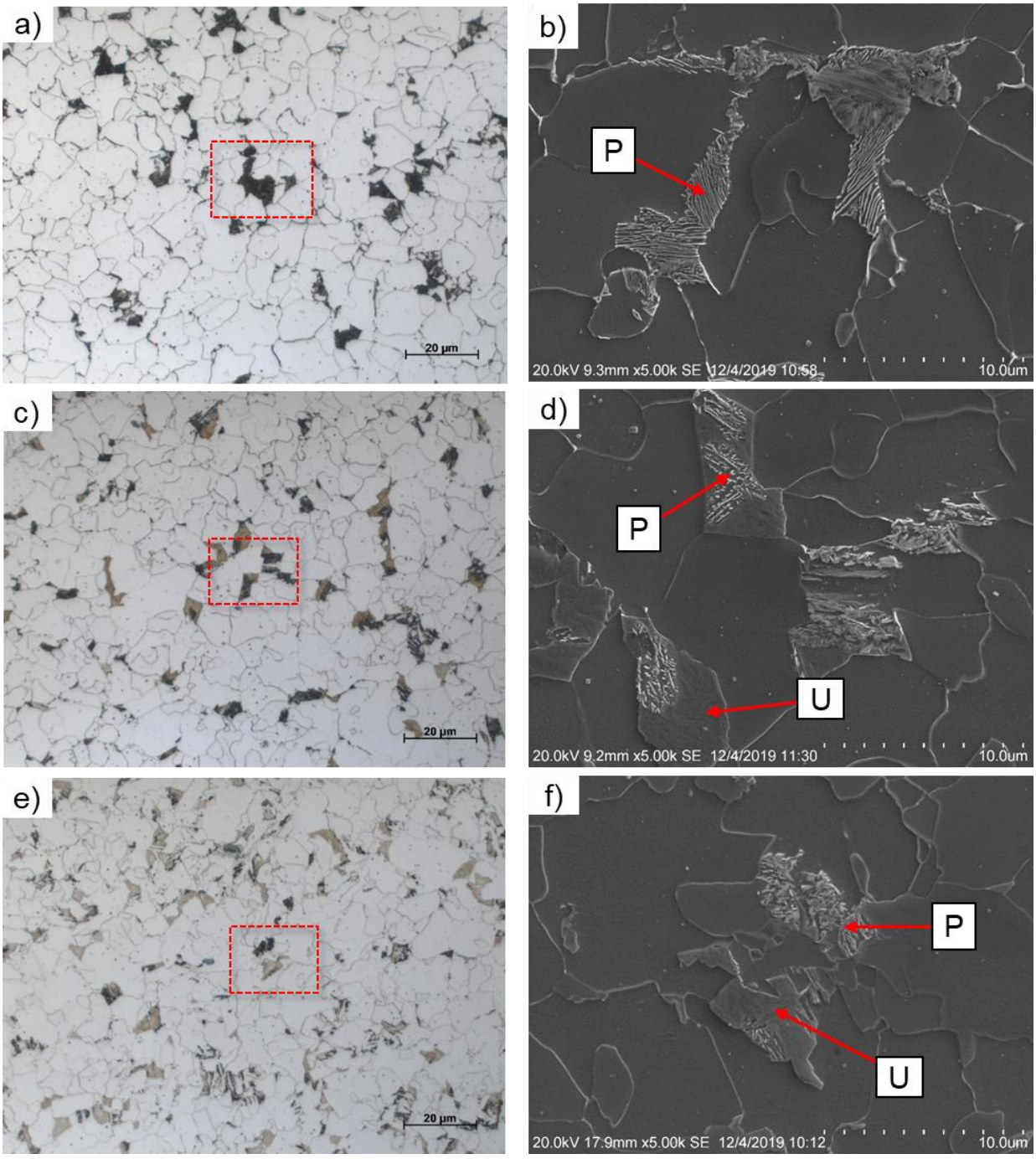


**Figure 63.** Corresponding LOM and SEM images of the pearlite (P) and light etching microstructural constituents (U) in a DH36 dilatometry specimen heated to a peak temperature of 875 °C (1607 °F) and cooled at 1, 5, and 10 °C/s (1.8, 9, and 18 °F/s). Boxes in the left images highlight the regions presented in the right images.

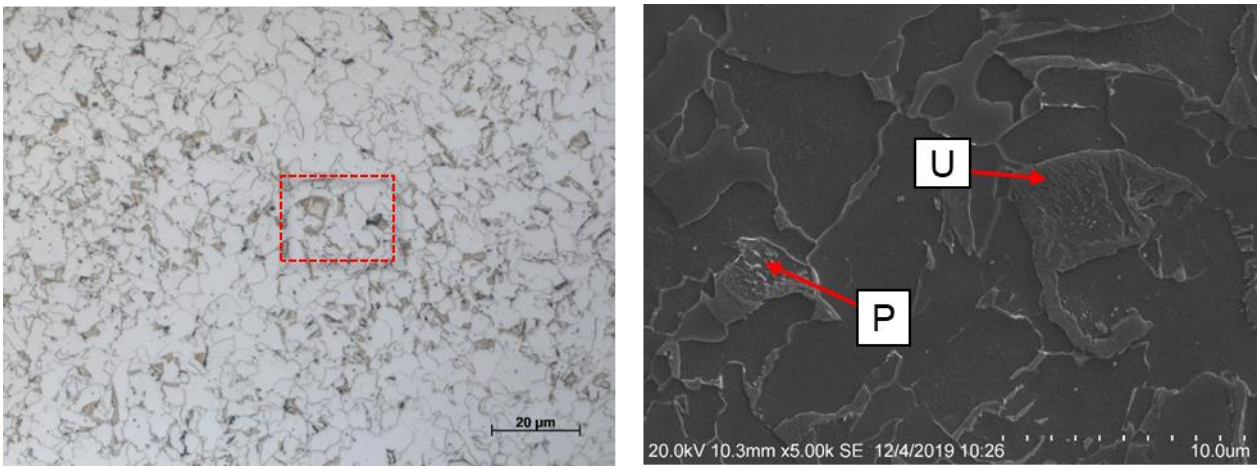


**Figure 64.** Corresponding LOM and SEM images of the pearlite (P) and light etching microstructural constituents (U) in a DH36 dilatometry specimen heated to a peak temperature of 875 °C (1607 °F) and cooled at 25 °C/s (45 °F/s). Box in the left image highlights the region presented in the right image.

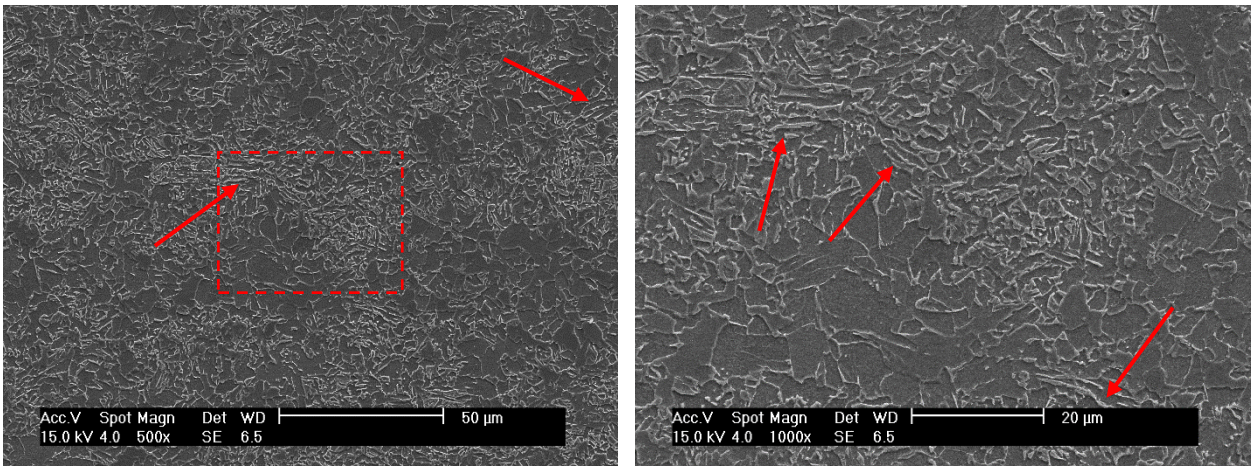


**Figure 65.** SEM images of the microstructure of a DH36 dilatometry specimen heated to a peak temperature of 875 °C (1607 °F) and cooled at 100 °C/s (180 °F/s). Arrows indicate high aspect ratio constituents. Box in the left image highlights the region presented in the right image.

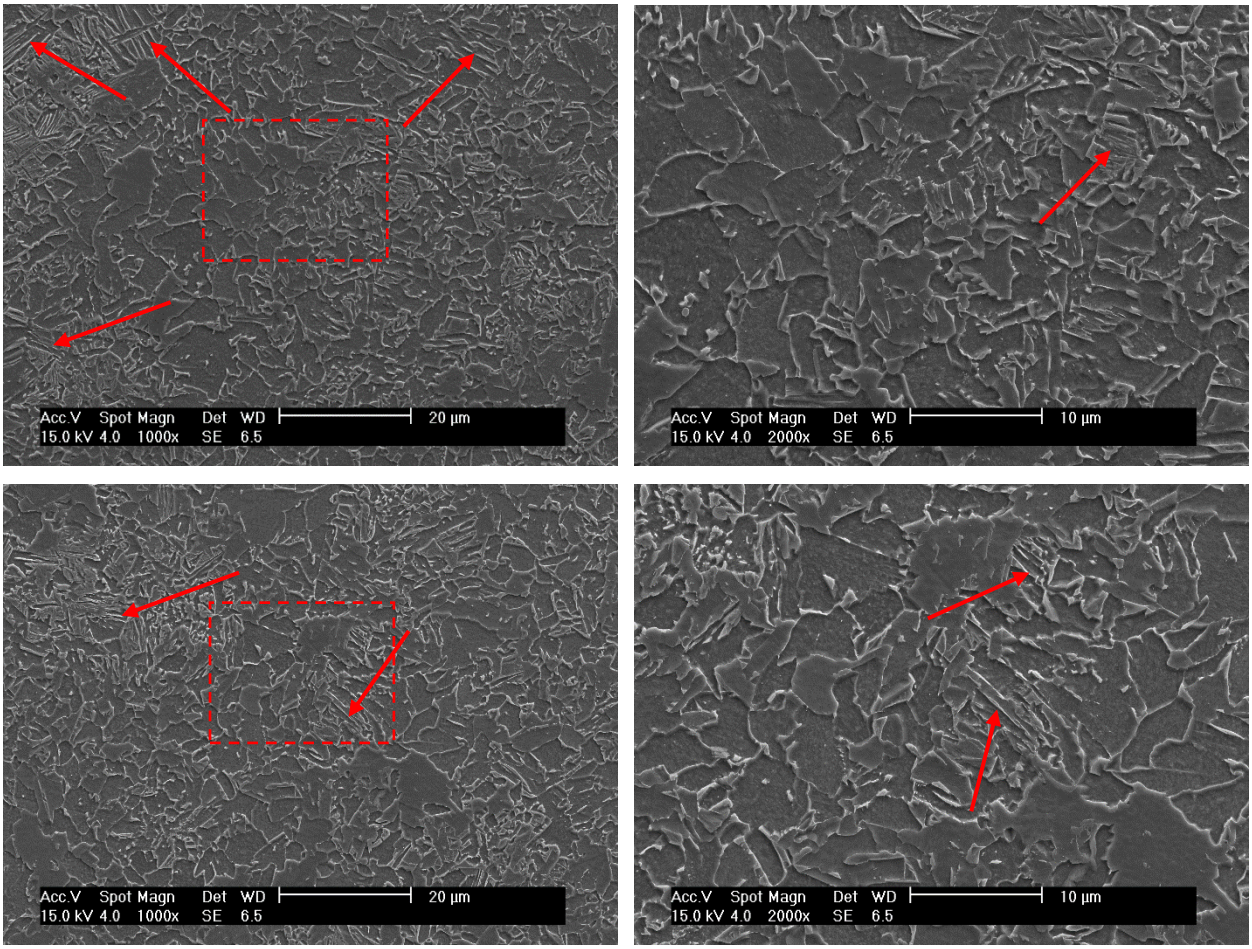


**Figure 66.** SEM images of microstructure of a DH36 dilatometry specimen heated to a peak temperature of 875 °C (1607 °F) and cooled at 200 °C/s (360 °F/s). Arrows indicate high aspect ratio constituents and possible aligned carbides. Boxes in the left images highlight the regions presented in the right images.

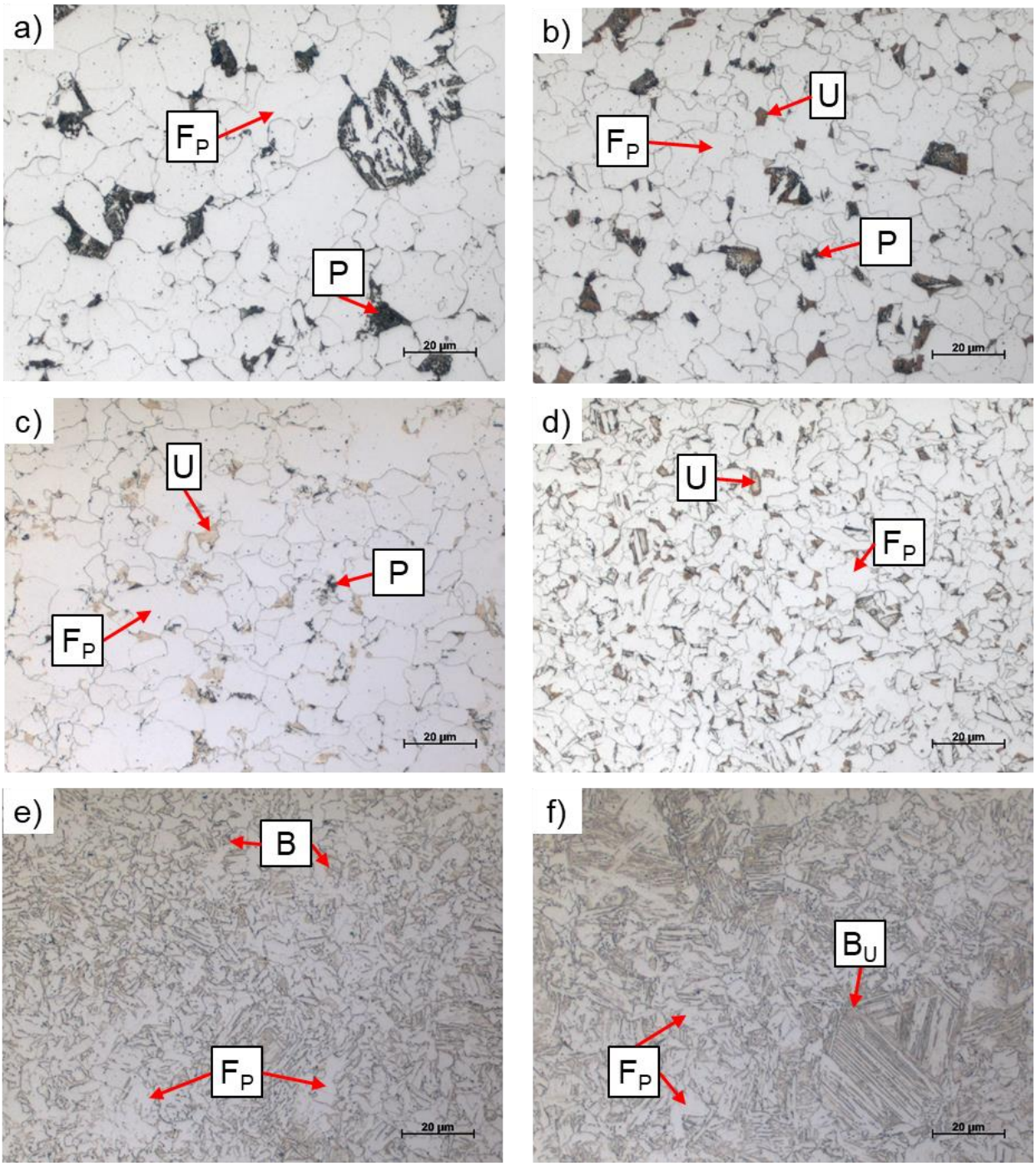


**Figure 67.** Representative microstructures from DH36 dilatometry specimens heated to a peak temperature of 1000 °C (1832 °F) and continuously cooled at various rates. **(a-f)**: 1, 5, 10, 25, 100, and 200 °C/s (1.8, 9, 18, 45, 180, and 360 °F/s).

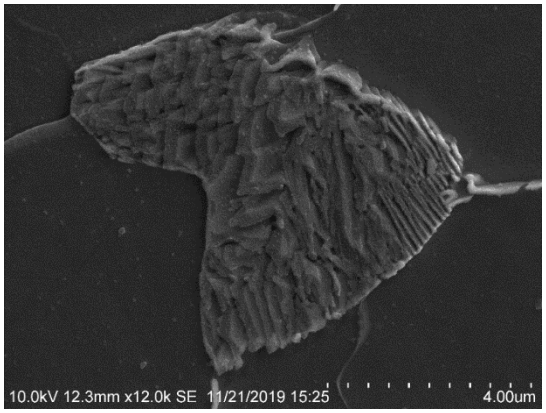


**Figure 68.** SEM image of a lamellar pearlite colony in a DH36 dilatometry specimen heated to a peak temperature of 1000 °C (1832 °F) and cooled at 1 °C/s (1.8 °F/s).

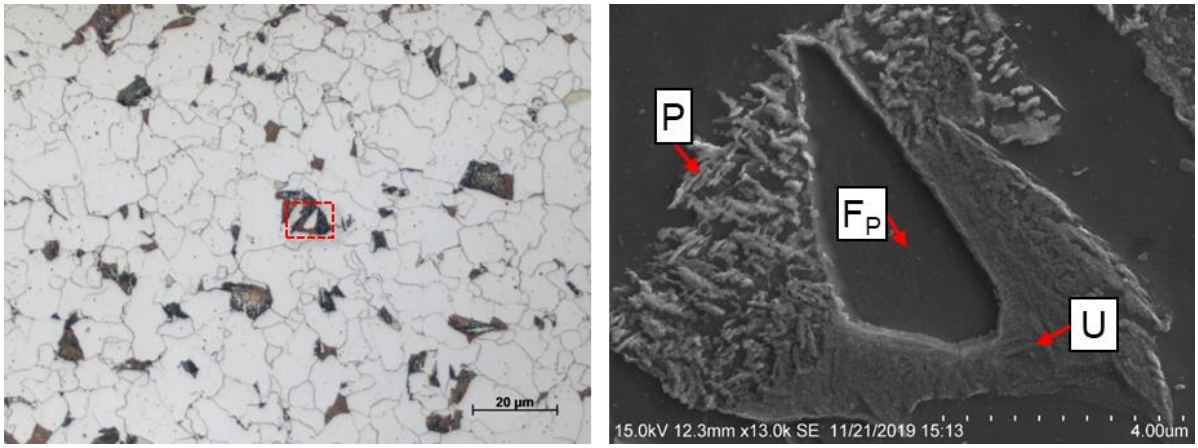


**Figure 69.** Corresponding LOM and SEM images of degenerate pearlite (P), primary ferrite ($F_P$) and light-etching carbide aggregate (C) in the microstructure of a DH36 dilatometry specimen heated to a peak temperature of 1000 °C (1832 °F) and cooled at 5 °C/s (9 °F/s). Box in the left image highlights the region presented in the right image.

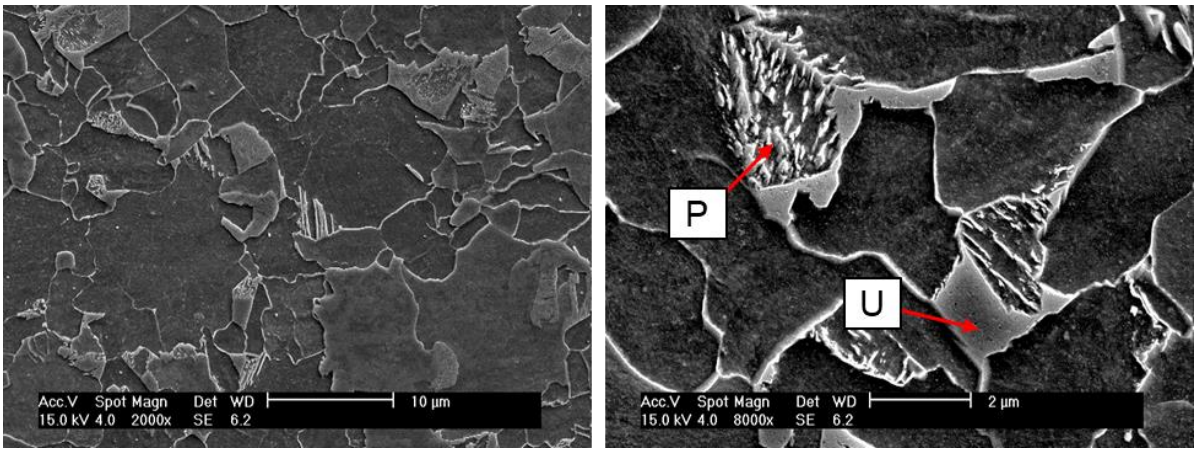


**Figure 70.** SEM images of degenerate pearlite and light etching carbide aggregate in the microstructure of a DH36 dilatometry specimen heated to a peak temperature of 1000 °C (1832 °F) and cooled at 10 °C/s (18 °F/s).

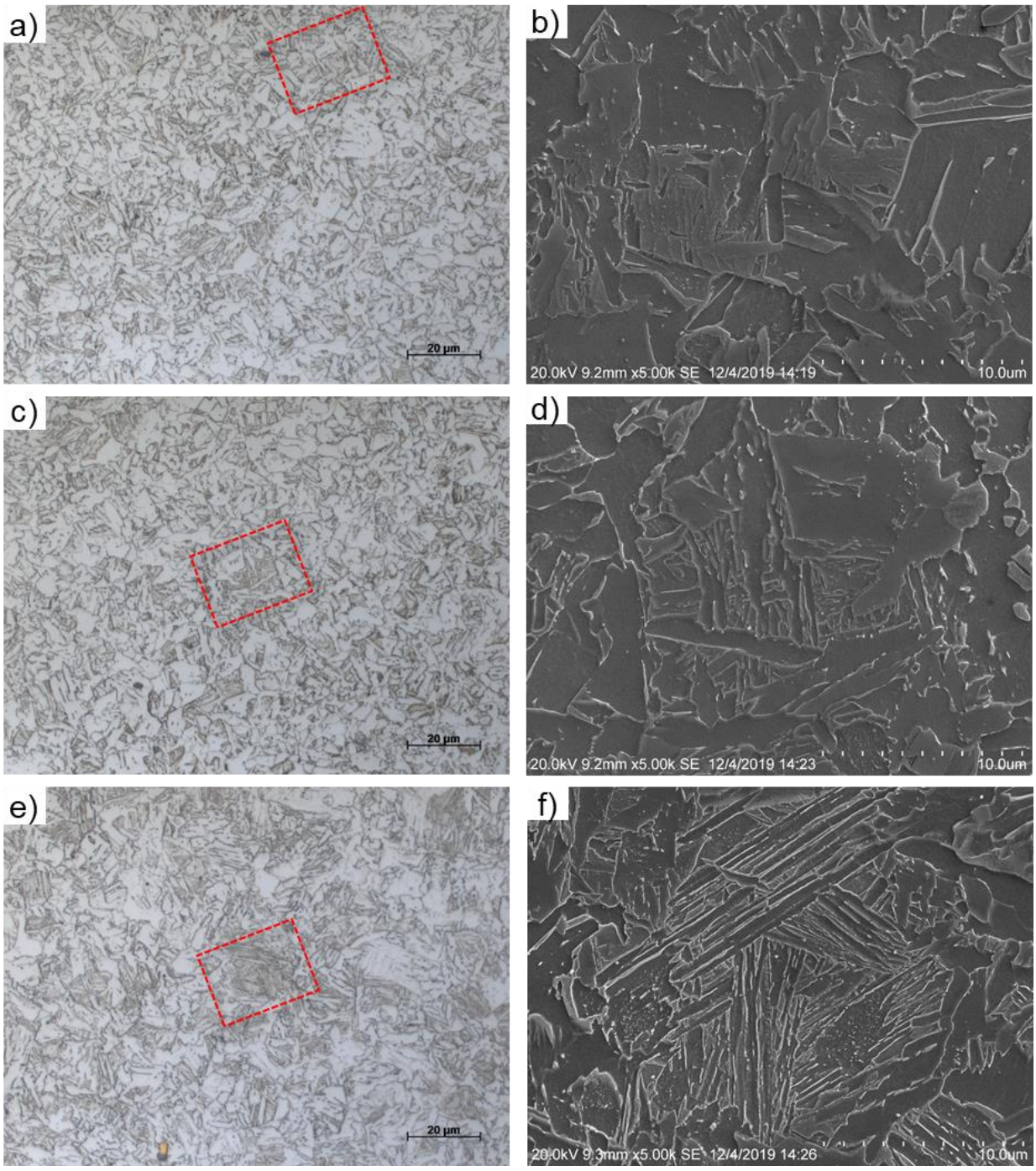


**Figure 71.** Corresponding LOM and SEM images of degenerate pearlite and light etching carbide aggregate in the microstructure of a DH36 dilatometry specimen heated to a peak temperature of 1000 °C (1832 °F) and cooled at (a-d): 100 °C/s (180 °F/s), (e-f): 200 °C/s (360 °F/s). Boxes in the left images highlight the regions presented in the right images.

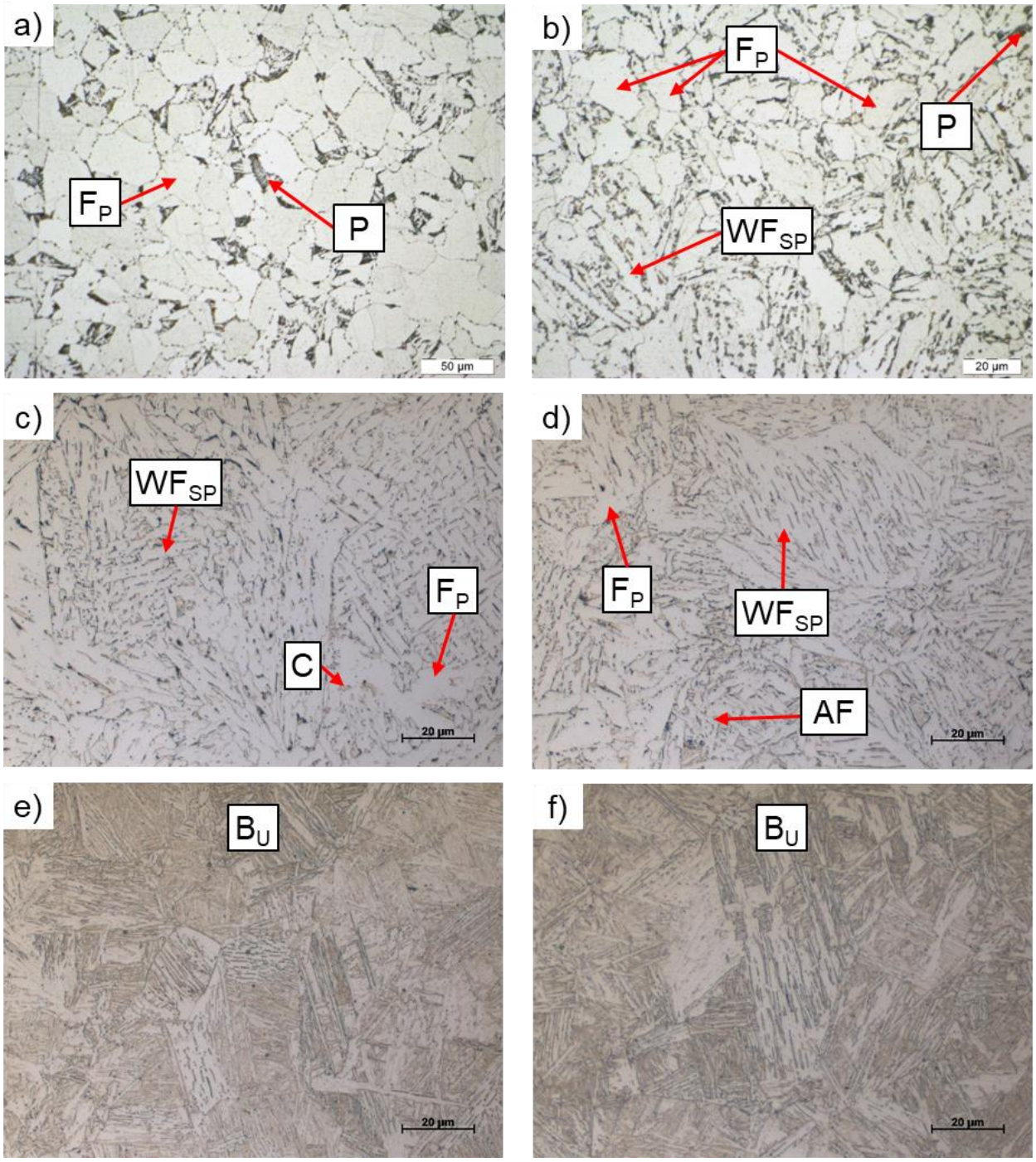


**Figure 72.** Representative microstructures from DH36 dilatometry specimens heated to a peak temperature of 1150 °C (2102 °F) and continuously cooled at various rates. **(a-f)**: 1, 5, 10, 25, 100, and 200 °C/s (1.8, 9, 18, 45, 180, and 360 °F/s).

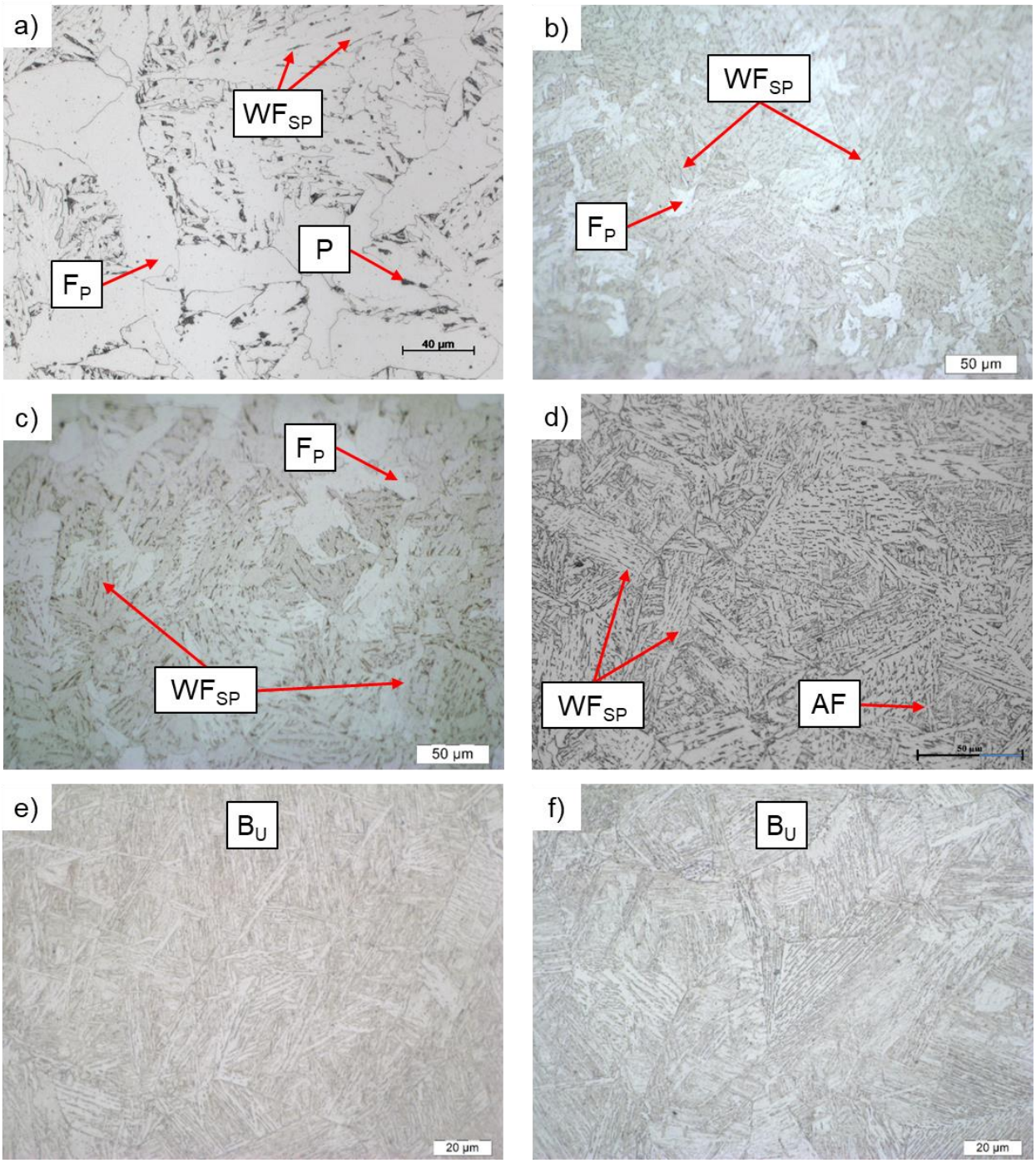


**Figure 73.** Representative microstructures from DH36 dilatometry specimens heated to a peak temperature of 1350 °C (2462 °F) and continuously cooled at various rates. **(a-f)**: 1, 5, 10, 25, 100, and 200 °C/s (1.8, 9, 18, 45, 180, and 360 °F/s).

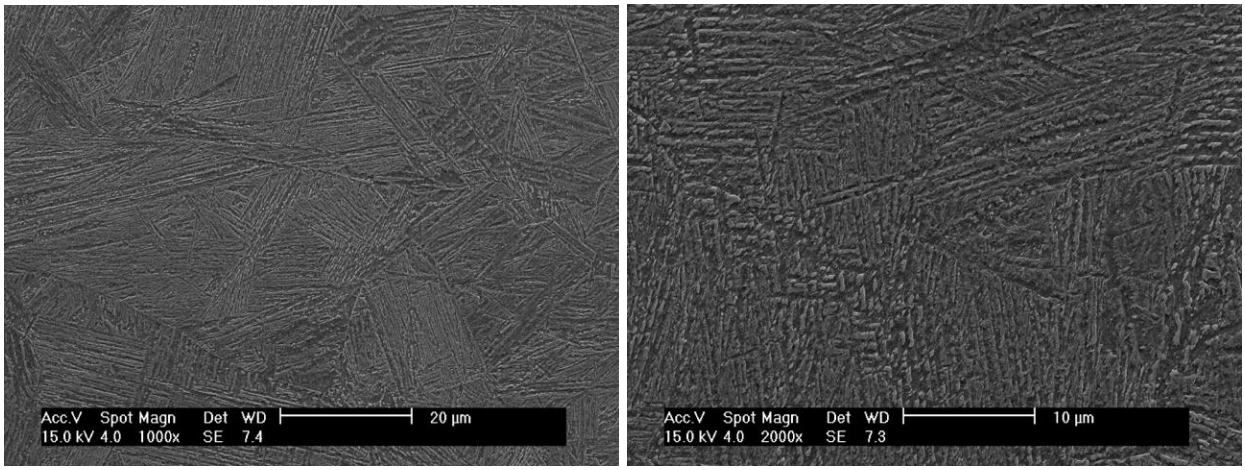


**Figure 74.** SEM images of the microstructure of a DH36 dilatometry specimen heated to a peak temperature of 1350 °C (2462 °F) and cooled at 100 °C/s (180 °F/s) showing a morphology that appears to be consistent with upper bainite.

## Appendix D: Microhardness Measurements

**Table 13.** Vickers microhardness of DH36 as a function of peak temperature and cooling rate. Errors are one standard deviation. Values in parenthesis are the number of indents measured.

| Cooling Rate | | Peak Temperature | | | | |
|---|---|---|---|---|---|---|
| | | **°C** | **875** | **1000** | **1150** | **1350** |
| **°C/s** | **°F/s** | **°F** | **1607** | **1832** | **2102** | **2432** |
| 1 | 1.8 | 165 ± 5 (45) | | 155 ± 8 (20)<br>146 ± 5 (24) | 187 ± 8 (51) | 199 ± 9 (15) |
| 5 | 9 | 177 ± 9 (15) | | 183 ± 7 (25) | 193 ± 5 (40) | 195 ± 4 (200) |
| 10 | 18 | 191 ± 5 (20) | | 176 ± 7 (297) | 218 ± 5 (27) | 197 ± 5 (100) |
| 25 | 45 | 203 ± 8 (15) | | 202 ± 6 (30) | 232 ± 7 (18) | 228 ± 9 (25) |
| 100 | 180 | 222 ± 9 (31) | | 243 ± 5 (12) | 317 ± 19 (39) | 320 ± 20 (195) |
| 200 | 360 | 242 ± 14 (40) | | 263 ± 18 (20) | 316 ± 13 (52) | 342 ± 17 (115) |

**Table 14.** Microhardness measurements across the experimental tee joint weldment illustrated in **Figure 19**.

| Location | Distance from Fusion Line (μm) | Traverse 1 Hardness (HV) | Traverse 2 Hardness (HV) | Traverse 3 Hardness (HV) |
|---|---|---|---|---|
| Fusion Zone | -799.03 | 188 | 209 | 203 |
| | -700.2 | 198 | 210 | 204 |
| | -599 | 202 | 213 | 206 |
| | -500 | 204 | 209 | 211 |
| | -400 | 200 | 210 | 210 |
| | -300 | 211 | 199 | 204 |
| | -200 | 201 | 206 | 216 |
| | -99 | 205 | 204 | 210 |
| Fusion Line | 0 | 206 | 214 | 202 |
| CGHAZ | 100 | 217 | 210 | 218 |
| | 201 | 211 | 224 | 207 |
| | 300 | 214 | 215 | 206 |
| | 399 | 215 | 211 | 196 |
| | 500 | 214 | 203 | 208 |
| | 600 | 204 | 205 | 200 |
| | 700 | 209 | 207 | 202 |
| FGHAZ | 799 | 207 | 203 | 205 |
| | 899 | 202 | 203 | 205 |
| | 1000 | 204 | 210 | 207 |
| | 1101 | 196 | 203 | 203 |
| | 1199 | 197 | 201 | 198 |
| ICHAZ | 1300 | 197 | 201 | 196 |
| | 1399 | 198 | 198 | 194 |
| | 1499 | 195 | 196 | 191 |
| | 1600 | 194 | 194 | 195 |
| | 1698 | 194 | 191 | 196 |
| | 1799 | 200 | 198 | 187 |
| | 1899 | 194 | 186 | 196 |
| | 1998 | 186 | 190 | 190 |
| | 2099 | 192 | 188 | 203 |
| | 2198 | 185 | 187 | 186 |
| | 2299 | 186 | 186 | 183 |
| Base Metal | 2398 | 172 | 193 | 182 |
| | 2497 | 176 | 186 | 177 |
| | 2598 | 179 | 173 | 183 |
| | 2698 | 172 | 187 | 186 |
| | 2797 | 182 | 186 | 195 |
| | 2899 | 193 | 188 | 186 |
| | 2997 | 194 | 181 | 183 |
| | 3098 | 186 | 189 | 185 |
| | 3198 | 185 | 187 | 183 |
| | 3296 | 188 | 194 | 185 |
| | 3398 | 191 | 192 | 197 |
| | 3496 | 188 | 185 | 188 |
| | 3597 | 180 | 188 | 184 |

**Table 15.** Microhardness measurements across the experimental butt joint weldment illustrated in **Figure 20**.

| Traverse 1 | | Traverse 2 | | Traverse 3 | | Traverse 4 | |
|---|---|---|---|---|---|---|---|
| **Hardness (HV)** | **Distance (µm)** | **Hardness (HV)** | **Distance (µm)** | **Hardness (HV)** | **Distance (µm)** | **Hardness (HV)** | **Distance (µm)** |
| 183 | 4799.78 | 224 | 3.91 | 182 | 4350.37 | 207 | -300.12 |
| 187 | 4650 | 207 | 155 | 172 | 4200 | 204 | -150 |
| 190 | 4500 | 209 | 304 | 176 | 4050 | 215 | 0 |
| 187 | 4350 | 206 | 454 | 183 | 3900 | 207 | 151 |
| 188 | 4200 | 202 | 604 | 192 | 3750 | 205 | 301 |
| 185 | 4050 | 206 | 754 | 188 | 3600 | 199 | 451 |
| 185 | 3901 | 206 | 904 | 185 | 3450 | 197 | 601 |
| 186 | 3750 | 213 | 1054 | 187 | 3300 | 202 | 751 |
| 183 | 3601 | 201 | 1205 | 188 | 3150 | 210 | 900 |
| 188 | 3450 | 198 | 1354 | 188 | 3000 | 211 | 1050 |
| 185 | 3300 | 203 | 1504 | 193 | 2850 | 220 | 1200 |
| 182 | 3150 | 196 | 1654 | 201 | 2701 | 215 | 1351 |
| 180 | 3000 | 191 | 1803 | 202 | 2550 | 216 | 1500 |
| 178 | 2850 | 195 | 1954 | 194 | 2400 | 213 | 1650 |
| 175 | 2700 | 197 | 2104 | 196 | 2250 | 203 | 1800 |
| 180 | 2550 | 193 | 2253 | 196 | 2100 | 198 | 1950 |
| 182 | 2400 | 193 | 2404 | 197 | 1950 | 195 | 2100 |
| 186 | 2250 | 188 | 2554 | 197 | 1800 | 190 | 2250 |
| 182 | 2100 | 174 | 2704 | 201 | 1650 | 189 | 2400 |
| 188 | 1950 | 177 | 2854 | 209 | 1499 | 177 | 2550 |
| 190 | 1800 | 179 | 3004 | 211 | 1350 | 183 | 2700 |
| 197 | 1650 | 181 | 3154 | 209 | 1200 | 180 | 2850 |
| 197 | 1500 | 179 | 3304 | 205 | 1050 | 182 | 2999 |
| 198 | 1350 | 178 | 3454 | 200 | 900 | 186 | 3150 |
| 195 | 1200 | 180 | 3603 | 201 | 751 | 186 | 3300 |
| 203 | 1051 | 179 | 3754 | 207 | 600 | 191 | 3450 |
| 205 | 900 | 177 | 3904 | 204 | 450 | 191 | 3600 |
| 202 | 751 | 172 | 4054 | 215 | 301 | 190 | 3749 |
| 210 | 600 | 175 | 4203 | 205 | 151 | 189 | 3900 |
| 208 | 450 | 172 | 4354 | 210 | 0 | 186 | 4049 |
| 209 | 300 | 178 | 4503 | 213 | -149 | 188 | 4200 |
| 214 | 150 | 182 | 4654 | 212 | -300 | 191 | 4349 |
| 215 | 0 | 186 | 4803 | 209 | -450 | 185 | 4500 |
| 214 | -150 | 181 | 4953 | 216 | -601 | 188 | 4650 |
| 206 | -300 | 184 | 5104 | 211 | -750 | 190 | 4799 |
| 229 | -449 | 186 | 5253 | 207 | -899 | 193 | 4950 |
| 218 | -600 | 188 | 5404 | 220 | -1050 | 185 | 5099 |
| 229 | -751 | 184 | 5553 | 215 | -1200 | 182 | 5250 |
| 218 | -900 | 184 | 5704 | 222 | -1349 | 187 | 5399 |
| 216 | -1049 | 184 | 5854 | 215 | -1500 | 191 | 5550 |
| | | | | | | 184 | 5699 |

## Appendix E: Thermo-Physical Property Datasets for DH36

**Table 16.** Experimentally measured coefficient of thermal expansion (CTE) of DH36.

| Facility | Temperature Range (°C) | Derived CTE ($10^{-6}$ °$C^{-1}$) | Average CTE ($10^{-6}$ °$C^{-1}$) | 1σ ($10^{-6}$ °$C^{-1}$) |
|---|---|---|---|---|
| NSWCCD | 100-650 | 16.0 | 16.0 | 0.4 |
| | | 16.2 | | |
| | | 16.3 | | |
| | | 16.1 | | |
| | | 15.9 | | |
| | | 15.3 | | |
| | 950-1300 | 21.7 | 20.8 | 1.4 |
| | | 22.6 | | |
| | | 21.7 | | |
| | | 19.1 | | |
| | | 19.6 | | |
| | | 20.4 | | |
| Ohio State | 100-650 | 15.5 | 15.2 | 0.5 |
| | | 15.5 | | |
| | | 15.6 | | |
| | | 14.8 | | |
| | | 14.4 | | |
| | 950-1300 | 18.9 | 21.0 | 2.9 |
| | | 17.6 | | |
| | | 20.6 | | |
| | | 24.3 | | |
| | | 23.8 | | |
| Combined | 100-650 | - | 15.6 | 0.6 |
| | 950-1300 | - | 20.9 | 2.1 |

**Table 17.** Experimentally measured specific heat of DH36.

| Temperature (°C) | $c_p$ (J/g-°C) | (°C) | $c_p$ (J/g-°C) | (°C) | $c_p$ (J/g-°C) | (°C) | $c_p$ (J/g-°C) |
|---|---|---|---|---|---|---|---|
| 23 | 0.4587 | 370 | 0.5932 | 720 | 0.9436 | 1070 | 0.5940 |
| 30 | 0.4607 | 380 | 0.5978 | 730 | 0.9796 | 1080 | 0.5965 |
| 40 | 0.4647 | 390 | 0.6023 | 740 | 1.0293 | 1090 | 0.5989 |
| 50 | 0.4686 | 400 | 0.6072 | 750 | 1.1881 | 1100 | 0.6013 |
| 60 | 0.4718 | 410 | 0.6135 | 760 | 1.2325 | 1110 | 0.6036 |
| 70 | 0.4758 | 420 | 0.6192 | 770 | 1.0689 | 1120 | 0.6059 |
| 80 | 0.4798 | 430 | 0.6255 | 780 | 0.9652 | 1130 | 0.6080 |
| 90 | 0.4840 | 440 | 0.6308 | 790 | 0.8932 | 1140 | 0.6102 |
| 100 | 0.4882 | 450 | 0.6348 | 800 | 0.8451 | 1150 | 0.6123 |
| 110 | 0.4923 | 460 | 0.6406 | 810 | 0.8336 | 1160 | 0.6143 |
| 120 | 0.4964 | 470 | 0.6462 | 820 | 0.8215 | 1170 | 0.6162 |
| 130 | 0.5004 | 480 | 0.6512 | 830 | 0.8173 | 1180 | 0.6181 |
| 140 | 0.5042 | 490 | 0.6577 | 840 | 0.8231 | 1190 | 0.6200 |
| 150 | 0.5080 | 500 | 0.6639 | 850 | 0.8293 | 1200 | 0.6218 |
| 160 | 0.5117 | 510 | 0.6705 | 860 | 0.8423 | 1210 | 0.6233 |
| 170 | 0.5153 | 520 | 0.6746 | 870 | 0.8327 | 1220 | 0.6249 |
| 180 | 0.5189 | 530 | 0.6811 | 880 | 0.7754 | 1230 | 0.6265 |
| 190 | 0.5227 | 540 | 0.6904 | 890 | 0.7238 | 1240 | 0.6280 |
| 200 | 0.5263 | 550 | 0.6926 | 900 | 0.6575 | 1250 | 0.6296 |
| 210 | 0.5302 | 560 | 0.6959 | 910 | 0.6212 | 1260 | 0.6312 |
| 220 | 0.5339 | 570 | 0.7031 | 920 | 0.5904 | 1270 | 0.6324 |
| 230 | 0.5378 | 580 | 0.7085 | 930 | 0.5914 | 1280 | 0.6336 |
| 240 | 0.5416 | 590 | 0.7193 | 940 | 0.5747 | 1290 | 0.6348 |
| 250 | 0.5454 | 600 | 0.7273 | 950 | 0.5783 | 1300 | 0.6360 |
| 260 | 0.5491 | 610 | 0.7365 | 960 | 0.5753 | 1310 | 0.6372 |
| 270 | 0.5530 | 620 | 0.7518 | 970 | 0.5774 | 1320 | 0.6384 |
| 280 | 0.5568 | 630 | 0.7622 | 980 | 0.5687 | 1330 | 0.6392 |
| 290 | 0.5607 | 640 | 0.7813 | 990 | 0.5838 | 1340 | 0.6742 |
| 300 | 0.5645 | 650 | 0.7977 | 1000 | 0.5752 | 1350 | 0.7384 |
| 310 | 0.5682 | 660 | 0.8159 | 1010 | 0.5780 | 1360 | 0.8572 |
| 320 | 0.5719 | 670 | 0.8340 | 1020 | 0.5808 | 1370 | 0.6955 |
| 330 | 0.5762 | 680 | 0.8529 | 1030 | 0.5836 | 1380 | 0.6923 |
| 340 | 0.5801 | 690 | 0.8715 | 1040 | 0.5863 | 1390 | 1.7954 |
| 350 | 0.5844 | 700 | 0.8929 | 1050 | 0.5889 | 1400 | 0.6988 |
| 360 | 0.5889 | 710 | 0.9152 | 1060 | 0.5915 | | |

**Table 18.** Experimentally measured thermal properties of DH36.

| Temperature (°C) | Thermal Diffusivity ($cm^2/sec$) | Density ($g/cm^3$) | Thermal Conductivity (W/cm-°C) |
|---|---|---|---|
| **23** | 0.11136 | 7.806 | 0.3987 |
| **50** | 0.11193 | 7.798 | 0.4090 |
| **100** | 0.11040 | 7.783 | 0.4195 |
| **200** | 0.10490 | 7.751 | 0.4279 |
| **300** | 0.09607 | 7.714 | 0.4183 |
| **400** | 0.08621 | 7.677 | 0.4019 |
| **500** | 0.07468 | 7.641 | 0.3788 |
| **600** | 0.06414 | 7.603 | 0.3547 |
| **700** | 0.05114 | 7.569 | 0.3456 |
| **800** | 0.03279 | 7.540 | 0.2089 |
| **900** | 0.05456 | 7.541 | 0.2705 |
| **1000** | 0.05974 | 7.510 | 0.2581 |
| **1100** | 0.06113 | 7.467 | 0.2745 |
| **1200** | 0.06356 | 7.426 | 0.2935 |
| **1300** | 0.06235 | 7.397 | 0.2933 |
| **1400** | 0.26576 | -- | -- |

## Appendix F: Thermo-Mechanical Properties

**Table 19.** Assumed elevated temperature elastic modulus for DH36 base material, as shown in Figure 27. Data are based on an assumed room temperature modulus of 210 GPa (30.5 Msi).

| Temperature (°C [°F]) | Fraction of Room Temperature Modulus | Elastic Modulus (GPa [Msi]) |
|---|---|---|
| **23 (73)** | 1.0000 | 210 (30.5) |
| **100 (212)** | 1.0000 | 210 (30.5) |
| **200 (392)** | 0.9000 | 189 (27.4) |
| **300 (572)** | 0.8000 | 168 (24.4) |
| **400 (752)** | 0.7000 | 147 (21.3) |
| **500 (932)** | 0.6000 | 126 (18.3) |
| **600 (1112)** | 0.3100 | 65 (9.4) |
| **700 (1292)** | 0.1300 | 27 (4.0) |
| **800 (1472)** | 0.0900 | 19 (2.7) |
| **900 (1652)** | 0.0675 | 14 (2.1) |
| **1000 (1832)** | 0.0450 | 9 (1.4) |
| **1100 (2012)** | 0.0225 | 5 (0.7) |
| **1200 (2192)** | 0.0000 | 0 (0) |

**Table 20.** Elevated temperature mechanical properties of DH36 base material, as shown in **Figures 28-29**.

| Specimen ID | Test Temperature (°C [°F]) | Yield Strength (MPa [ksi]) | Tensile Strength (MPa [ksi]) | Elongation in 1 in. (%) |
|---|---|---|---|---|
| 1088-RTT1 | 22 (72) | 483 (70.0) | 574 (83.2) | 34.5 |
| 1088-RTT2 | 22 (72) | 483 (70.1) | 576 (83.5) | 33.5 |
| 1088-ETT1 | 100 (212) | 451 (65.4) | 532 (77.1) | 21.0 |
| 1088-ETT2 | 300 (572) | 370 (53.6) | 559 (81.0) | 36.0 |
| 1088-ETT3 | 500 (932) | 248 (35.9) | 354 (51.3) | 39.0 |
| 01788-ETT1 | 600 (1112) | 171 (24.8) | 206 (29.8) | 40.5 |
| 1088-ETT4 | 700 (1292) | 108 (15.6) | 117 (17.0) | 48.0 |
| 01788-ETT2 | | 108 (15.6) | 110 (15.9) | 34.5 |
| 1088-ETT5 | 800 (1472) | 42 (6.1) | 59 (8.5) | 66.0 |
| 01788-ETT3 | | 48 (7.0) | 50 (7.2) | 24.5 |
| 1088-ETT6 | 900 (1652) | 38 (5.5) | 54 (7.9) | 65.0 |
| 01788-ETT4 | | 42 (6.1) | 53 (7.7) | 46.5 |
| 1088-ETT7 | 1000 (1832) | 21 (3.1) | 35 (5.1) | 77.0 |
| 01788-ETT5 | | 19 (2.8) | 32 (4.6) | 34.0 |
| 1088-ETT8 | 1100 (2012) | 9.7 (1.4) | 32 (3.1) | 49.0 |

**Table 21.** Yield strength of simulated DH36 CGHAZs after heating to 1350 °C (2462 °F) and cooling at different rates, as illustrated in **Figure 30**.

| Temperature (°C) [°F] | Yield Strength (MPa) | | | |
|---|---|---|---|---|
| | 1 °C/s Cooling | 10 °C/s Cooling | 100 °C/s Cooling | Austenite on Cooling |
| 25 [77] | 441 | 446 | 623 | |
| 200 [392] | 424 | 502 | 629 | |
| 400 [752] | 356 | 455 | 490 | |
| 600 [1112] | 223 | 285 | 304 | |
| 700 [1292] | 132 | 154 | 173 | |
| 1000 [1832] | | | | 20 |
| 1100 [2012] | | | | 15 |
| 1200 [2192] | | | | 12 |

**Table 22.** On-heating flow behavior of DH36 base material, as shown in **Figures 31-32**.

| 22 °C (72 °F) | | 100 °C (212 °F) | | 300 °C (572 °F) | | 500 °C (932 °F) | | 700 °C (1292 °F) | |
|---|---|---|---|---|---|---|---|---|---|
| $\varepsilon_{p,\,true}$ | σ (MPa) | $\varepsilon_{p,\,true}$ | σ (MPa) | $\varepsilon_{p,\,true}$ | σ (MPa) | $\varepsilon_{p,\,true}$ | σ (MPa) | $\varepsilon_{p,\,true}$ | σ (MPa) |
| **0.0000** | 482 | **0.0000** | 451 | **0.0000** | 369 | **0.0000** | 247 | **0.0000** | 110 |
| **0.0050** | 484 | **0.0050** | 460 | **0.0050** | 424 | **0.0050** | 285 | **0.0050** | 105 |
| **0.0100** | 488 | **0.0100** | 464 | **0.0100** | 472 | **0.0100** | 314 | **0.0100** | 109 |
| **0.0200** | 500 | **0.0200** | 499 | **0.0200** | 515 | **0.0200** | 324 | **0.0200** | 110 |
| **0.0300** | 541 | **0.0300** | 521 | **0.0300** | 534 | **0.0300** | 330 | **0.0300** | 104 |
| **0.0498** | 580 | **0.0326** | 526 | **0.0328** | 539 | **0.0330** | 333 | **0.0345** | 104 |

| 800 °C (1472 °F) | | 900 °C (1652 °F) | | 1000 °C (1832 °F) | | 1100 °C (2012 °F) | |
|---|---|---|---|---|---|---|---|
| $\varepsilon_{p,\,true}$ | σ (MPa) | $\varepsilon_{p,\,true}$ | σ (MPa) | $\varepsilon_{p,\,true}$ | σ (MPa) | $\varepsilon_{p,\,true}$ | σ (MPa) |
| **0.0000** | 42 | **0.0000** | 38 | **0.0000** | 21 | **0.0000** | 9 |
| **0.0050** | 47 | **0.0050** | 38 | **0.0050** | 23 | **0.0050** | 12 |
| **0.0100** | 48 | **0.0100** | 40 | **0.0100** | 25 | **0.0100** | 13 |
| **0.0200** | 48 | **0.0200** | 42 | **0.0200** | 27 | **0.0200** | 14 |
| **0.0300** | 48 | **0.0300** | 40 | **0.0282** | 26 | **0.0300** | 14 |
| **0.0330** | 48 | **0.0324** | 40 | | | **0.0353** | 15 |

**Table 23.** Flow stress of simulated DH36 CGHAZs after heating to 1350 °C (2462 °F) and cooling at 1 °C/s (1.8 °F/s), as illustrated in **Figure 33**. Terminal values are at the UTS.

| 25 °C (77 °F) | | 200 °C (392 °F) | | 400 °C (752 °F) | | 600 °C (1112 °F) | | 700 °C (1292 °F) | |
|---|---|---|---|---|---|---|---|---|---|
| $\varepsilon_{p,\,true}$ | σ (MPa) | $\varepsilon_{p,\,true}$ | σ (MPa) | $\varepsilon_{p,\,true}$ | σ (MPa) | $\varepsilon_{p,\,true}$ | σ (MPa) | $\varepsilon_{p,\,true}$ | σ (MPa) |
| **0.0000** | 441 | **0.0000** | 424 | **0.0000** | 356 | **0.0000** | 223 | **0.0000** | 132 |
| **0.0050** | 477 | **0.0050** | 482 | **0.0050** | 415 | **0.0050** | 262 | **0.0050** | 154 |
| **0.0100** | 501 | **0.0100** | 498 | **0.0100** | 443 | **0.0100** | 272 | | |
| **0.0200** | 533 | **0.0200** | 545 | **0.0200** | 475 | **0.0200** | 280 | | |
| **0.0300** | 558 | **0.0300** | 570 | **0.0300** | 494 | **0.0300** | 281 | | |
| **0.0400** | 577 | **0.0400** | 590 | **0.0400** | 507 | **0.0400** | 281 | | |
| **0.0500** | 592 | **0.0500** | 603 | **0.0500** | 518 | **0.0500** | 283 | | |
| **0.1000** | 636 | **0.1000** | 632 | **0.1000** | 552 | **0.1000** | 286 | | |
| **0.1800** | 658 | **0.14** | 639 | **0.1920** | 583 | | | | |

**Table 24.** Flow stress of simulated DH36 CGHAZs after heating to 1350 °C (2462 °F) and cooling at 10 °C/s (18 °F/s), as illustrated in **Figure 34**. Terminal values are at the UTS.

| 25 °C | | 200 °C | | 400 °C | | 600 °C | | 700 °C | |
|---|---|---|---|---|---|---|---|---|---|
| $\varepsilon_{p,\,true}$ | σ (MPa) | $\varepsilon_{p,\,true}$ | σ (MPa) | $\varepsilon_{p,\,true}$ | σ (MPa) | $\varepsilon_{p,\,true}$ | σ (MPa) | $\varepsilon_{p,\,true}$ | σ (MPa) |
| **0.0000** | 446 | **0.0000** | 502 | **0.0000** | 455 | **0.0000** | 285 | **0.0000** | 154 |
| **0.0050** | 531 | **0.0050** | 591 | **0.0050** | 510 | **0.0050** | 343 | **0.0050** | 218 |
| **0.0100** | 558 | **0.0100** | 610 | **0.0100** | 535 | **0.0100** | 353 | **0.0060** | 219 |
| **0.0200** | 594 | **0.0200** | 633 | **0.0200** | 564 | **0.0200** | 353 | | |
| **0.0300** | 621 | **0.0300** | 648 | **0.0300** | 581 | | | | |
| **0.0400** | 641 | **0.0400** | 669 | **0.0400** | 595 | | | | |
| **0.0500** | 658 | **0.0500** | 685 | **0.0500** | 603 | | | | |
| **0.1000** | 697 | **0.1000** | 733 | **0.1000** | 624 | | | | |
| **0.1760** | 715 | **0.1480** | 743 | **0.1260** | 634 | | | | |

**Table 25.** Flow stress of simulated DH36 CGHAZs after heating to 1350 °C (2462 °F) and cooling at 100 °C/s (180 °F/s), as illustrated in **Figure 35**. Terminal values are at the UTS.

| 25 °C | | 200 °C | | 400 °C | | 600 °C | | 700 °C | |
|---|---|---|---|---|---|---|---|---|---|
| $\varepsilon_p$ | σ (MPa) | $\varepsilon_p$ | σ (MPa) | $\varepsilon_p$ | σ (MPa) | $\varepsilon_p$ | σ (MPa) | $\varepsilon_p$ | σ (MPa) |
| **0.0000** | 623 | **0.0000** | 679 | **0.0000** | 490 | **0.0000** | 304 | **0.0000** | 173 |
| **0.0050** | 683 | **0.0050** | 738 | **0.0050** | 599 | **0.0050** | 355 | **0.0050** | 213 |
| **0.0100** | 714 | **0.0100** | 771 | **0.0100** | 632 | **0.0100** | 364 | **0.0060** | 214 |
| **0.0200** | 755 | **0.0200** | 810 | **0.0200** | 660 | **0.0120** | 365 | | |
| **0.0300** | 781 | **0.0300** | 828 | **0.0300** | 671 | | | | |
| **0.0400** | 799 | **0.0400** | 842 | **0.0400** | 675 | | | | |
| **0.0500** | 813 | **0.0500** | 853 | **0.0500** | 675 | | | | |
| **0.1000** | 846 | **0.1000** | 881 | **0.0750** | 676 | | | | |
| **0.1300** | 854 | **0.1210** | 887 | | | | | | |

**Table 26.** Flow stress of austenitic DH36 CGHAZs after heating to 1350 °C (2462 °F), as illustrated in **Figure 36**. Terminal values are at the UTS.

| 1000 °C | | 1100 °C | | 1200 °C | |
|---|---|---|---|---|---|
| $\varepsilon_p$ | σ (MPa) | $\varepsilon_p$ | σ (MPa) | $\varepsilon_p$ | σ (MPa) |
| **0.0000** | 20 | **0.0000** | 15 | **0.0000** | 12 |
| **0.0050** | 25 | **0.0050** | 17 | **0.0050** | 14 |
| **0.0100** | 26 | **0.0100** | 20 | **0.0100** | 15 |
| **0.0200** | 31 | **0.0200** | 21 | **0.0200** | 16 |
| **0.0300** | 33 | **0.0300** | 24 | **0.0300** | 18 |
| **0.0400** | 37 | **0.0400** | 25 | **0.0400** | 19 |
| **0.0500** | 40 | **0.0500** | 27 | **0.0500** | 20 |
| **0.1000** | 46 | **0.1000** | 32 | **0.1000** | 20 |
| **0.2000** | 55 | **0.1180** | 32 | **0.1800** | 24 |

**Table 27.** Engineering fracture strain for the specimens shown in **Figures 33-35**.

| Temperature (°C) [°F] | Fracture Strain, $\varepsilon_{f,\,eng}$ (mm/mm) | | |
|---|---|---|---|
| | 1 °C/s Cooling | 10 °C/s Cooling | 100 °C/s Cooling |
| 25 [77] | 0.44 | 0.41 | 0.40 |
| 200 [392] | 0.30 | 0.32 | 0.29 |
| 400 [752] | 0.51 | 0.44 | 0.33 |
| 600 [1112] | 0.33 | 0.13 | 0.11 |
| 700 [1292] | 0.17 | 0.11 | 0.16 |

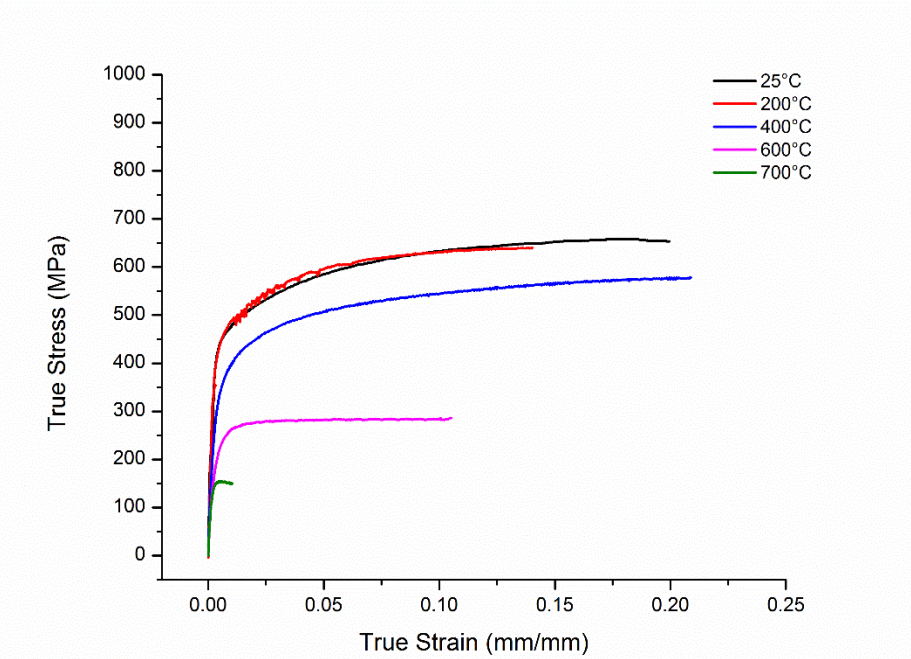


**Figure 75.** Uniaxial tension stress-strain curves from Gleeble tensile samples thermally cycled to a peak temperature of 1350 °C (2462 °F), cooled at 1 °C/s (1.8 °F/s), then reheated to the test temperature.

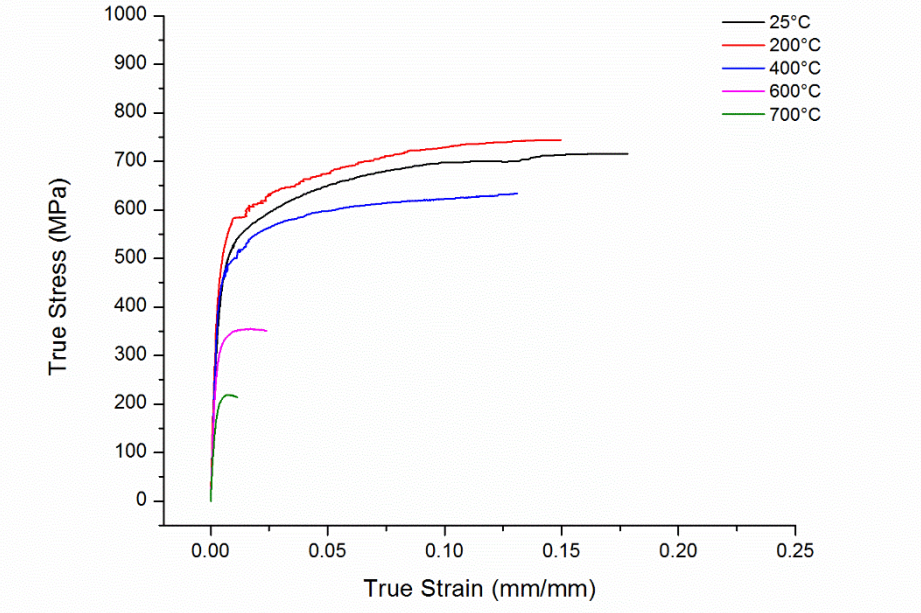


**Figure 76.** Uniaxial tension stress-strain curves from Gleeble tensile samples thermally cycled to a peak temperature of 1350 °C (2462 °F), cooled at 10 °C/s (18 °F/s), then reheated to the test temperature.

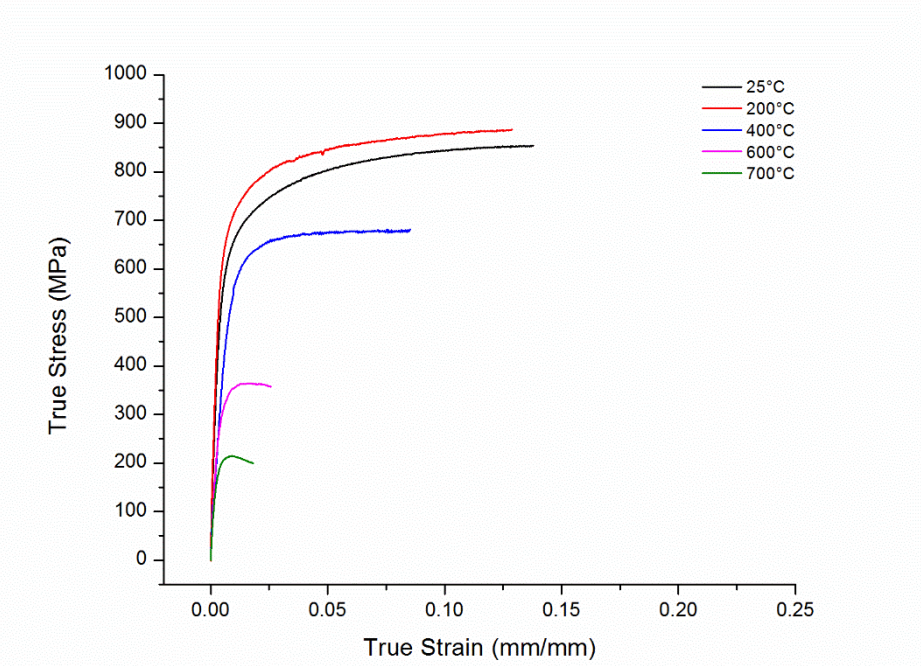


**Figure 77.** Uniaxial tension stress-strain curves from Gleeble tensile samples thermally cycled to a peak temperature of 1350 °C (2462 °F), cooled at 100 °C/s (180 °F/s), then reheated to the test temperature.

## REFERENCES


[1] L. F. Andersen, "Residual Stresses and Deformations in Steel Structures," Doctoral Thesis, Department of Naval Architecture and Offshore Engineering, University of Denmark, 2000.

[2] MIL-S-22698C, "Military Specification: Steel Plate, Shapes, and Bars, Weldable Ordinary Strength and Higher Strength: Structural," 29 June 1988.

[3] ASTM A945/M-16, "Standard Specification for High-Strength Low-Alloy Structural Steel Plate with Low Carbon and Restricted Sulfur for Improved Weldability, Formability, and Toughness," ASTM International, West Conshohocken, PA, 2016.

[4] NAVSEA Technical Publication T9074-BD-GIB-010/0300 Rev. 2, "Base Materials for Critical Applications: Requirements for Low Alloy Steel Plate, Forgings, Castings, Shapes, Bars, and Heats of HY-80/100/130 and HSLA-80/100," 18 December 2012.

[5] ASTM A541/M-05 (2015), "Standard Specification for Quenched and Tempered Carbon and Alloy Steel Forgings for Pressure Vessel Components," ASTM International, West Conshohocken, PA, 2015.

[6] ASTM A131/M-14, "Standard Specification for Structural Steel for Ships," ASTM International, West Conshohocken, PA, 2014.

[7] American Bureau of Shipping, "Rules for Materials and Welding (Part 2)," Houston, TX, 2016.

[8] ASTM E417-17, "Standard Test Method for Analysis of Carbon and Low-Alloy Steel by Spark Atomic Emission Spectrometry," ASTM International, West Conshohocken, PA, 2017.

[9] G. R. Eisler and P. W. Fuerschbach, "SOAR: An Extensible Suite of Codes for Weld Analysis and Optimal Weld Schedules," in *Seveth International Conference on Computer Technology in Welding*, San Francisco, CA, 1997.

[10] ASTM E1461-13, "Standard Test Method for Thermal Diffusivity by the Flash Method," ASTM International, West Conshohocken, PA, 2013.

[11] ASTM E1269-11 (2018), "Standard Test Method for Determining Specific Heat Capacity by Differential Scanning Calorimetry," ASTM International, West Conshohocken, PA, 2018.

[12] ASTM A370-18, "Standard Test Methods and Definitions for Mechanical Testing of Steel Products," ASTM International, West Conshohocken, PA, 2018.

[13] ASTM E21-17, "Standard Test Methods for Elevated Temperature Tension Tests of Metallic Materials," ASTM International, West Conshohocken, PA, 2017.

[14] T. D. Huang, M. Harbison, S. Scholler, H. Rucker, J. Hu, P. Dong, M. Collette, H. Chung, M. Groden, W. Zhang, J. Semple, R. Kirchain, R. Roth, M. Bustamante, Y. Yang, R. Dull, Y. Gooroochurn, M. Doroudian, C. F. Fisher, M. Sinfield, D. Kihl and A. Gonzalez, "Robust Distortion Control Methods and Implementation for Construction of Lightweight Metallic Structures," *SNAME Transactions*, 2016.

[15] N. Yurioka, S. Oshita and H. Tamehiro, "Determination of Necessary Preheating Temperature in Steel Welding," *Welding Journal*, vol. 52, no. 6, pp. 147-s to 153-s, 1983.

[16] J. O. Andersson, T. Herlander, L. Hoglund, P. F. Shi and B. Sundman, "Thermo-Calc & DICTRA, Computational Tools for Materials Science," *Calphad*, vol. 26, pp. 92-101, 2002.

[17] W. S. Rasband, "ImageJ," U. S. National Institutes of Health, Bethesda, MD, USA, 1997-2018. [Online]. Available: https://imagej.nih.gov/ij/.

[18] ASTM E1382-97 (2015), "Standard Test Methods for Determining Average Grain Size Using Semiautomatic And Automatic Image Analysis," ASTM International, West Conshohocken, PA, 2015.

[19] C. Heinze, A. Pittner, M. Rethmeiri and S. S. Babu, "Dependency of Martensite Start Temperature on Prior Austenite Grain Size and Its Influence on Welding-Induced Residual Stress," *Computational Materials Science,* vol. 69, pp. 251-260, 2013.

[20] M. Shome and O. N. Mohanty, "Continuous cooling Transformation Diagrams Applicable to the Heat-Affected Zone of HSLA-80 and HSLA-100 Steels," *Metallurgical and Materials Transactions A,* vol. 37A, pp. 2159-2169, 2006.

[21] B. Taljat, B. Radhakrishnan and T. Zacharia, "Numerical Analysis of GTA Welding Process with Emphasis on Post-Solidification Phase Transformation Effects on Residual Stress," *Materials Science and Engineering A,* vol. A246, pp. 45-54, 1998.

[22] X. Yue, J. C. Lippold, B. T. Alexandrox and S. S. Babu, "Continuous Cooling Transformatoin Behavior in the CGHAZ of Naval Steels," *Welding Journal,* vol. 91, no. 3, pp. 67-s to 75-s, 2012.

[23] R. R. Mohanty, N. Fonstein and O. Girina, "Effect of Heating Rate on the Austenite Formation in Low-Carbon High-Strength Steels Annealed in the Intercricial Region," *Metallurgical and Materials Transactiona A,* vol. 42A, no. 12, pp. 3680-3690, 2011.

[24] F. L. G. Oliveira, M. S. Andrade and A. B. Cota, "Kinetics of Austenite Formation during Continuous Heating in a Low Carbon Steel," *Materials Characterization,* vol. 58, pp. 256-261, 2007.

[25] C. A. Apple and G. Krauss, "The Effect of Heating Rate on the Martensite to Austenite Transformation in Fe-Ni-C Alloys," *Acta Materialia,* vol. 20, pp. 849-856, 1972.

[26] Bainite Committee of The Iron & Steel Institute of Japan, "Atlas for Bainitic Microstructures, Vol. 1: Continuous-Cooled Microstructures of Low Carbon HSLA Steels," The Iron & Steel Institute of Japan, 1992.

[27] H. K. D. H. Bhadeshia and R. W. K. Honeycombe, Steels: Microstructure and Properties, 3 ed., Oxford, UK: Butterwoth-Heinemann, 2006.

[28] A. K. Sinha, Ferrous Physical Metallurgy, Stoneham, MA: Butterworth Publishers, 1989.

[29] G. Thewlis, "Classification and Quantification of Microstructures in Steels," *Materials Science and Technology,* vol. 20, pp. 143-160, 2004.

[30] International Institute of Welding, Compendium of Weld Metal Microstructures and Properties: Submerged-arc Welds in Ferritic Steel, Cambridge, UK: Woodhead Publishing, 1985.

[31] M. Peet, "Prediction of Martensite Start Temperature," *Materials Science and Technology,* vol. 31, no. 11, pp. 1370-1375, 2014.

[32] S. Kang, S. Yoon and S.-J. Lee, "Prediction of Bainite Start Temperature in Alloy Steels with Difference Grain Sizes," *ISIJ International,* vol. 54, no. 4, pp. 997-999, 2014.

[33] C. Capdevilla, F. G. Caballero and C. Garcia de Andres, "Determination of Ms Temperature in Steels: A Bayesian Neural Network Model," *ISIJ International,* vol. 42, pp. 894-902, 2002.

[34] J. S. Kirkaldy and D. Venugopalan, "Phase Transformations in Ferrous Alloys," in *Phase Transformations in Ferrous Alloys: Proceedings of an International Conference,* Philadelphia, PA, 1984.

[35] S.-J. Lee, J.-S. Park and Y.-K. Lee, "Effect of Austenite Grain Size on the Transformation inetics of Upper and Lower Bainite in a Low-Alloy Steel," *Scripta Materialia,* vol. 59, no. 1, pp. 87-90, 2008.

[36] J. J. Valencia and C. Papesch, "Automated Thermal Plate Forming: Apparent Specific Heat and Thermal Expansion During Heating of HSLA-80 and DH-36 Steel Plates," Naval Metalworking Center as operated by Concurrent Technologies Corporation, Johnstown, PA, 2005.

[37] ASTM E111-17, "Standard Test Method for Young's Modulus, Tangent Modulus, and Chord Modulus," ASTM International, West Conshohocken, PA, 2017.

[38] E. 1993-1-1, "Eurocode 3: Design of steel structures - Part 1-1: General rules and rules for buildings," 2005.

[39] E. 1993-1-2, "Eurocode 3: Design of steel structures - Part 1-2: General rules - Structural fire design," 2005.

[40] P. Holsberg, "An Overview of Some Current Research on Welding Residual Stresses and Distortion in the U.S. Navy," Naval Surface Warfare Center, Carderock Division, West Bethesda, MD, 1997.

*This page intentionally left blank*

## DISTRIBUTION

### EXTERNAL

| | Copies |
|---|---|
| DEFENSE TECHNICAL INFORMATION CENTER<br>727 JOHN J KINGMAN ROAD<br>SUITE 0944<br>FORT BELVOIR, VA 22060-6218 | 1 |
| COMMANDER<br>ATTN: SEA 05P2<br>NAVAL SEA SYSTEMS COMMAND<br>1333 ISAAC HULL AVENUE S.E.<br>WASHINGTON NAVY YARD<br>WASHINGTON, DC 20376<br>ATTN: Archer, Bjornson, McGrorey, Melvin | 4 |
| OFFICE OF NAVAL RESEARCH<br>875 N RANDOLPH ST<br>ARLINGTON, VA 22217<br>ATTN: Carney, Mullins | 2 |
| LIGHTWEIGHT INNOVATIONS FOR TOMORROW (LIFT)<br>1400 ROSA PARKS BOULEVARD<br>DETROIT, MI 48216<br>ATTN: Hawke | 1 |
| HUNTINGTON-INGALLS INDUSTRIES – INGALLS SHIPBUILDING<br>100 JERRY ST PE HIGHWAY<br>PASCAGOULA, MS 39581<br>ATTN: Huang, Yang | 2 |
| OHIO STATE UNIVERSITY<br>WELDING ENGINEERING PROGRAM<br>1248 ARTHUR E ADAMS DR<br>COLUMBUS, OH 43221<br>ATTN: Zhang | 1 |

### NSWCCD INTERNAL DISTRIBUTION

| Code | Name | Copies |
|---|---|---|
| 60 | | 1 |
| 61 | DeLoach | 1 |
| 611 | Davis | 1 |
| 611 | Sinfield | 1 |
| 611 | Farren | 1 |
| 611 | Fisher | 2 |
| 611 | Bechetti | 1 |
| 611 | Semple | 1 |
| 612 | (Report Documentation Page) | 1 |
| 613 | (Report Documentation Page) | 1 |
| 617 | (Report Documentation Page) | 1 |
| 63 | (Report Documentation Page) | 1 |
| 65 | (Report Documentation Page) | 1 |
| 66 | (Report Documentation Page) | 1 |
| 3442 | (TIC) | 1 |


NAVSEA
WARFARE CENTERS
Carderock